A thesis for the Degree of Doctor of Philosophy

Acoustic and Optical Characteristics of Cavitation

Bubble Clouds Produced by Shock Wave Pulse

Gwansuk Kang

Interdisciplinary Postgraduate Program in Biomedical Engineering

GRADUATE SCHOOL

JEJU NATIONAL UNIVERSITY

2018. 8.

Acoustic and Optical Characteristics of Cavitation Bubble Clouds Produced by Shock Wave Pulse

Gwansuk Kang
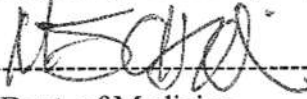
(Supervised by Professor Min Joo Choi)

A thesis submitted in partial fulfillment of the requirement for the degree of
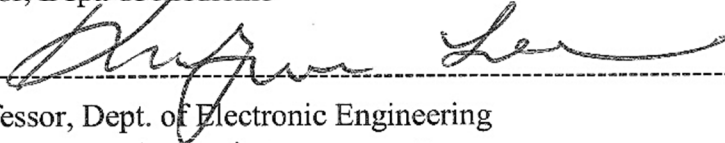Doctor of Philosophy

2018. 06.

This thesis has been examined and approved by

Thesis director, Kyung-Youn Kim, Professor, Dept. of Electronic Engineering

----
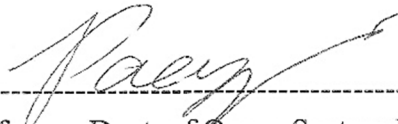
Min Joo Choi, Professor, Dept. of Medicine

Kwang-Man Lee, Professor, Dept. of Electronic Engineering

Mok Kun, Jeong, Professor, Division of Electrical and Electronic Engineering,
Daejin University

Dong-Guk Paeng, Professor, Dept. of Ocean System Engineering

Date ___2018. 06.___

Interdisciplinary Postgraduate Program in Biomedical Engineering
GRADUATE SCHOOL
JEJU NATIONAL UNIVERSITY

DEDICATED

To

My parents

Changrim Kang & Myungsoon Park

Two sisters and their families

Eunkyung Kang & Kinam Lee

Daye Lee

Dongeun Lee

Eunju Kang & Hakwon Kim

Jiyoung Kim

Jinpyo Kim

and

My partner

CONTENTS

LIST OF FIGURES

LIST OF TABLES

ABSTRACT

A shock pressure pulse used in an extracorporeal shock wave treatment has a large negative pressure (<-5 MPa) which can produce cavitation. Cavitation is known to have therapeutic effects but its measurement is not easy. This thesis is to measure cavitation induced by shock wave through an optical hydrophone and optical visualization.

The signals of shock pressure were recorded by an optical hydrophone (FOPH2000, RP Acoustics, Germany) submerged in water for several hundred microseconds at the focus for analysis. The signals are characterized by shock pulse followed by a long tail after several microseconds; these signals are regarded as a Cavitation-Related Signal (CRS). The CRS was found to contain characteristic information about the shock pulse-induced cavitation. The first and second collapse times (t_1 and t_2) were identified in the CRS. The collapse time delay ($t_c = t_2 - t_1$) increased with the driving shock pressures. The signal amplitude integrated for the time delay was highly correlated with t_c (adjusted $R^2 = 0.990$). This finding suggests that a single optical hydrophone can be used to measure shock pulse and to characterize shock pulse-induced cavitation.

Cavitation bubbles produced by a clinical shock wave system were optically visualized and their geometric features were investigated in relation to the driving shock wave field. Cavitation bubbles induced by the shock wave were captured by an ordinary industrial CCD camera under illumination of a micro-pulse LED light. The light exposure was set to last for the whole life time of bubbles from formation to subsequent collapses. It was shown that the

cavitation bubbles appeared mostly in the vicinity of the focus. The bubbles became more and larger as approaching to the focus. Jet streams formed when collapsing of the cavitation bubbles became enlarged as the output setting of the shock wave device increased. The bubble cloud boundary was reasonably fitted to an elongated ellipsoid similar to the acoustic focal area of negative pressure. Grayscale intensity of visualized cavitation bubble was highly correlated with the amplitude of negative pressure (adjusted R^2 =0.87). When the light exposure time was varied, we could visualize the focal point where the bubbles were concentrated and confirm the collapse time of the bubbles. The geometric features of the cavitation bubbles were characteristically similar to those of the focusing acoustic field, which has potential to provide the therapeutic focal information. The similarity of these characteristics enabled to visualization of the cavitation cloud image, which may provide the intensity field and location of shock wave irradiation. This result would be useful for the clinical quality assurance of therapeutic devices without time-consuming and causing damages of the expensive hydrophone sensor. The present study is limited to the static afterimages of the cavitation bubbles, and further investigation including the bubble dynamics is suggested to deliver the more realistic therapeutic area of the shock wave therapy.

Key words: Extracorporeal shock wave therapy, Cavitation bubble cloud, Bubble collapse time, Shock wave acoustic field, Optical hydrophone, Visualization, Micro-Pulse LED Light

Chapter 1

INTRODUCTION

1.1 Brief Historical Background

During the First and Second World War, lung injuries caused by underwater blasts among castaways swimming in the sea or divers operating military operations were reported (Wolf, 1970; Krause, 1997; Lance *et al*., 2015). The researchers studied the effects of shock waves on the human body and tried to protect the human body from shock waves rather than using it (Loske *et al*., 2017).

In 1955, Lev Aleksandrovich Yutkin discovered the electrohydraulic (EH) effect, which has been widely used in science and engineering field, and it is an important principle of extracorporeal shock wave source used today (Bekaev *et al*., 2014; Xu and Xu, 2015). In an EH effect, a high voltage electrical discharge through a liquid instantaneously evaporates some of volume of liquid between the electrodes, resulting in an excessively high pressure wave as the gas expands (Bekaev *et al*., 2014).

In the early 1960s, engineers at Dornier Aerospace of the Federal Republic of Germany found and inspected aircraft damage suspected of being caused by shock waves (Lingeman, 1997). Meanwhile, in 1966, one engineer accidentally experienced that shock waves can affect human tissues without surface damage (Xu and Xu, 2015). In 1969, Dornier with the support of the Ministry of National Defense of the Federal Republic of Germany began to research and develop extracorporeal shock wave lithotripsy (ESWL). In 1974, Dornier developed the first test type machine of shock wave lithotripsy using EH effect, but its efficiency was low because it didn't equip the position control or diagnostic device for targeting. After combining with an ultrasound imaging device, Dornier Human Model 1 (HM1), the world's first prototype ESWL

machine, was presented in 1979 and the first clinical trial of ESWL was performed by Chaussy *et al*. (1982) using HM1 on February 7, 1980 (Figure 1.1a). In 1982, HM1 was upgraded to HM2 for a more convenient operating environment, and the first commercial optimized HM3 with a fluoroscopy positioning system was launched on the market in 1983 (Figure 1.1b) (Lingeman, 1997; Xu and Xu, 2015; Loske *et al*., 2017). Since then, many research papers were published using HM3. After US Food and Drug Administration (FDA) approved the machine, various companies in different countries started to develop and produce ESWL machines (Xu and Xu, 2015).

<center>(a)   (b)</center>
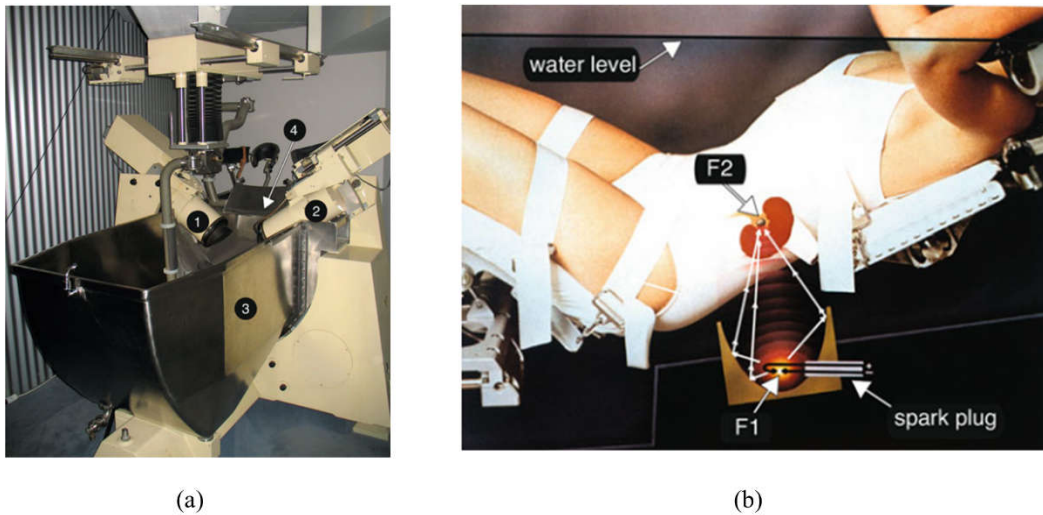
Figure 1.1 Photographs of the first generation extracorporeal shock wave lithotripter in 1980s. (a) the Human Model 1 (HM1, Dornier MedTech GmbH, Wessling, Germany), showing ① the right and ② the left image intensifier of the bi-planar fluoroscopy system to guide the localization of the target, ③ the water tank, and ④ the patient stretcher. (b) the Human Model 3 (HM3, Dornier MedTech GmbH, Wessling, Germany) with patient, Shock waves were generated by underwater electric discharges at the inner focus F_1 of a semi-ellipsoidal reflector and focused towards the outer focus F_2 (Loske *et al*., .2017).

1.2 Medical Applications of Shock Wave

Extracorporeal Shock Wave Lithotripsy

Since the development of shock wave generators, they have been applied to various applications. One of the most successful applications of shockwave technology is in medical fields, typically extracorporeal shock wave lithotripsy (ESWL).

"I will not use the knife, not even, verily, on sufferers from stone, but I will give place to such as are craftsmen therein – Hippocratic oath" (Jones, 1923).

As already mentioned in Hippocratic oath, renal stone disease has a very long history and the shock wave as a craftsman is now in responsible for many parts of kidney stone treatment and is considered as the first choice for the majority of urinary stones (Figure 1.2a) (Tailly, 2013). ESWL is a completely non-invasive therapeutic intervention for renal stone (Pearle, 2012). The stone location is aimed by diagnostic imaging device, and shock waves irradiated from outside of the body is transmitted to the target through the patient's tissue. The therapeutic efficacy is affected by various factors such as stone size, location and compositions. In general, it is reported that the stone-free rate after treatment is high in stones smaller than 15~20 mm in diameter, but for lower-pole, shock wave lithotripsy should be limited to a stone size of less than 10 mm in diameter. The stone-free rate is significantly lower when the stone diameter was more than 20 mm (Albala *et al*., 2001; Pearle *et al*., 2005; Worcester and Coe,

4

(a)

(b)

(c)

(d)
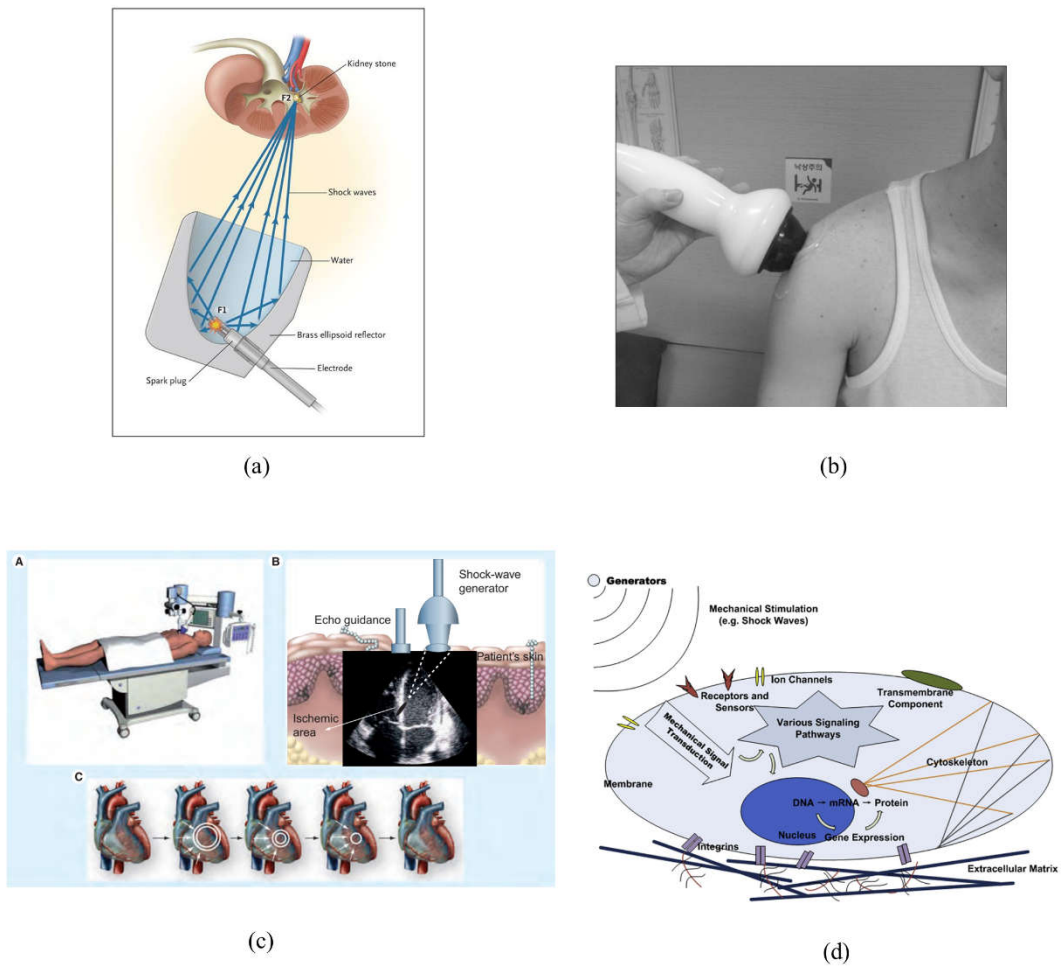
Figure 1.2 Medical applications of shock wave (a) ESWL (Pearle, 2012), (b) ESWT (Lee *et al.*, 2015), (c) Angiogenic and cardiac therapy (Ruiz-Garcia and Lerman, 2011), (d) cell stimulation (Ji *et al.*, 2016).

2010; Pearle, 2012).

Extracorporeal Shock Wave Treatment

Compared to ESWL, it has a relatively small focal zone, but similar shock pressure pulses have also been used for extracorporeal shock wave therapy (ESWT) which is used to treat orthopedic disorders including lateral epicondylitis of the elbow (Wang and Shen, 2002; Rompe and Maffulli, 2007), calcific tendinitis of the shoulder (Cosentino *et al*., 2003; Pan *et al*., 2003), and proximal plantar heel pain (Crawford and Snaith, 1996; Sun *et al*., 2017) (Figure 1.2b). Loew and Jurgowski (1993) first reported a shockwave-applied study on the treatment of calcific tendonitis of the rotator cuff using ESWL device in 1993.

Angiogenic & Cardiac

Since shock wave lithotripsy was introduced, its applications have been spreading from physical phenomena to the biological responses to stimulate living tissues. In the early 2000s, new and non-invasive angiogenic therapy (Ito *et al*., 2009; Hatanaka *et al*., 2016) and cardiac shock wave therapy (Nishida *et al*., 2004; Shimokawa *et al*., 2008; Cai *et al*., 2015) were developed for animal and human trial using relatively low intensity shock waves, which account for about 10 % of that used for urethral lithotripsy (Figure 1.2c).

Cell & Biological effects

Shock waves not only support the proliferation and differentiation of cells that contribute to wound healing (Huang *et al*., 2013; Raabe *et al*., 2013), but also affect endothelial cells (Sansone *et al*., 2012), bone cells (Kearney *et al*., 2012; Suhr *et al*., 2012), macrophage (Sukubo *et al*., 2015), and molecular delivery (Kodama *et al*., 2000) (Figure 1.2d). As described above, the biological effects and healing mechanisms are distinctly different from ESWL.

1.3 Treatment Mechanisms

The underlying mechanisms of shock pulse treatments remain unclear, but two important effects have been demonstrated (Choi, 1992; Coleman *et al*., 1989; Sapozhnikov *et al*., 2007).

First is a direct mechanical impact on target objects or tissues by shock pulse (Lokhandwalla and Sturtevant, 2000; Rassweiler *et al*., 2011; Forssmann *et al*., 1977). Mechanical deformation can occur under repetitive loading stress like shear-and-tear force that shock wave is transmitted and reflected at the target object-medium interface due to acoustic impedance mismatch, with pressure inversion that separates the target by tensile stress (Chaussy *et al*., 1980; Rassweiler *et al*., 2005). Spallation that the reflected tensile wave of the initially compression phase of the shock pulse takes place at the distal interface and combines with the negative phase of the shock pulse within the distal part to form the maximum tension

(Zhong *et al*., 1999; Sapozhnikov *et al*., 2007). Quasistatic squeezing that tensile stresses are generated front and rear ends of the target is caused by sound speed difference between target and surrounding medium (Eisenmenger, 2001; Sapozhnikov *et al*., 2007; Rassweiler *et al*., 2011). The other important effect is shock pulse-induced acoustic cavitation, which plays an important role in biological interaction (Coleman *et al*., 1987; Crum, 1988; Delius *et al*., 1988; Loske *et al*., 2002; Pishchalnikov *et al*., 2003; Pishchalnikov *et al*., 2006; Rink *et al*., 1994). Cavitation bubbles or cluster near the target can generate localized stress waves and the direct impact of a water jet generated by asymmetric or symmetric collapse of bubble (Sapozhnikov *et al*., 2007) (Figure 1.3). This study may reveal or effectively observe the cavitation phenomenon caused by the shock wave which is an important factor in the shock wave treatment.
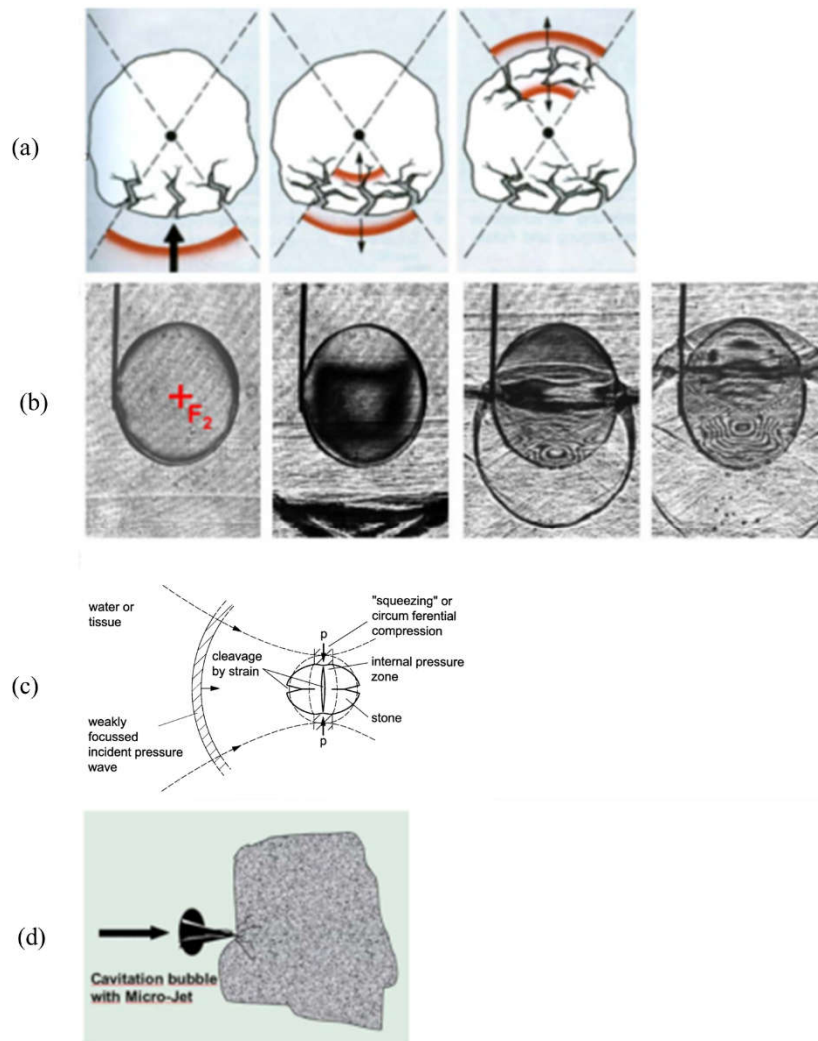
Figure 1.3 Treatment mechanisms (a) shear-and-tear force that shock wave is transmitted and reflected at the target object-medium interface due to acoustic impedance mismatch, with pressure inversion that separates the target by tensile stress, (b) spallation that the reflected tensile wave of the initially compression phase of the shock pulse takes place at the distal interface and combines with the negative phase of the shock pulse within the distal part to form the maximum tension , (c) quasistatic squeezing that tensile stresses are generated front and rear ends of the target caused by sound speed difference between target and surrounding medium, (d) acoustic cavitation that plays an important role in biological interaction   (Rassweiler *et al*., 2011).

1.4 A Review of Cavitation Measurement Techniques

Various attempts have been made to monitor cavitation activities. In this section, typical measurement methods for shock wave-induced cavitation are reviewed based on acoustic and optical techniques. The following PCD, ACD, and B-mode are acoustic techniques based on piezoelectric sensing materials, optical hydrophone and high-speed photography are optical techniques based on light refraction of medium.

Passive Cavitation Detector (PCD)

Acoustic emission that resulted from the collapses can be detected by a broadband ultrasonic transducer, known as a passive cavitation detector (PCD) (Figure 1.4a) (Atchley *et al*., 1988; Cunningham *et al*., 2001; Coleman *et al*., 1992). The characteristic of acoustic emission detected by PCD contains two spikes in time domain called the 1st and 2nd collapse signals for a single shock pulse (Coleman *et al*., 1996; Xi *et al*., 2000; Tu *et al*., 2007). A focused PCD that provides high sensitivity and spatial specificity in the focal region of the transducer is often used. However, this type of PCD is insensitive outside the focal region (Li *et al*., 2014). This focused PCD was tested to monitor the acoustic emission generated within the body of a patient during ESWL (Coleman *et al*., 1996). A simple unfocused PCD developed by Leighton *et al*. (2008) can also monitor the efficacy of shock wave lithotripsy treatment in real time. Orthogonally aligned confocal dual PCDs used the coincident signals

to provide direct evidence that acoustic wave emitted from cavitation activities in renal (Bailey

et al., 2005; Chitnis and Cleveland, 2006).

Active Cavitation Detector (ACD)

In contrast to PCD, active cavitation detector (ACD) senses the cavitation bubbles by

transmitting ultrasonic bursts and receiving backscattering signals reflected from the bubbles

(Figure 1.4b). This is basically the same principle as the ultrasonic A-mode technique, which

indicates a discrepancy in acoustic impedance between media. Roy *et al.* (1990) demonstrated

an acoustic backscattering technique for detecting presence of transient cavitation produced

by short pulses of high-frequency ultrasound. Madanshetty *et al.* (1991) conducted a

comparison of threshold measurement using PCD and ACD in the same environment. In their

study, ACD provides a high sensitivity to detect the occurrence of a weak cavitation event that

the PCD cannot detect. Typical PCDs and ACDs do not provide information on size or

population other than detection of bubble activities (Smith *et al.*, 2012a; McLaughlan *et al.*,

2010). On the other hand, ACD with multiple driving frequencies can estimate the bubble size

distribution from attenuation of received signal using spectral analysis (Caruthers *et al.*, 1999;

Choi *et al.*, 2006).

Ultrasound B-mode imaging

Ultrasonic B-mode image generated by clinical diagnostic ultrasound scanner also can be

11

used as an array active cavitation detector (array ACD) (Figure 1.4c) (Bailey *et al*., 2005; Pishchalnikov *et al*., 2005). The PCD can only provide 1D temporal history of acoustic emission from cavitation bubbles. On the other hand, B-mode imaging technique has already proved its visualization ability to offer anatomical information of the body with excellent temporal and spatial resolution (Tu *et al*., 2007; Rabkin *et al*., 2005). It is utilized to help guidance and real time monitoring of the treatment site that rely on the appearance of a hyperechoic region, which has been postulated to be the result of cavitation bubbles activity (Vaezy *et al*., 2001; Wu *et al*., 2003). Unlike visualized bubbles by the high speed camera, the echoes of cavitation bubbles detected by B-mode imaging have lasted much longer. This suggested that B-mode imaging has a better sensitivity than optical camera has and some bubbles persisted below the sensitivity of optical camera (Pishchalnikov *et al*., 2006).

These techniques employ the acoustic methods that measures the acoustic emission and scattering by cavitation bubbles. However, these cannot provide quantitative information on the acoustic pressure because they are located at a distance away from the shock wave field.

Optical Hydrophone

The methods described above employs piezoelectric materials as sensing elements, and the followings are optical methods. Optical hydrophone is introduced for reliable measurements in environments with very sharp wave front, high acoustic pressure and violent cavitation activities such as shock wave field (Figure 1.4d) (Staudenraus and Eisenmenger,

1993; Parsons *et al*., 2006). The optical hydrophone is not based on the piezoelectric effect, but it measures the amount of photons reflected from the fiber-water interface, which is modulated by acoustic pressure. It has a broadband frequency characteristics and strong resistance of violent cavitation activities. The bonding force between the silica fiber and the water molecule is stronger than that between water molecules, and thus suppresses cavitation occurrence on the fiber surface. However, optical hydrophones are not free from the effects of cavitation and are reporting on cavitation related signals including shock wave-bubble interaction (Pishchalnikov *et al*., 2005; Arora *et al*., 2007; Zhou *et al*., 2012) and fiber-bubble interaction (Wurster *et al*., 1994; Pishchalnikov *et al*., 2005; Zijlstra and Ohl, 2008; Smith *et al*., 2012b). Bull *et al*. (2013) reported that optical hydrophone can be used as a cavitation detector by measuring broadband acoustic emissions. Huber *et al*. (1994) demonstrated that saturated square waveform obtained by optical hydrophone could measure the lifetime of cavitation bubble, but it showed only particular case where air bubble is attached to the fiber glass trip. Obviously, the signals recorded by optical hydrophone contain cavitation activities, and it is necessary to interpret carefully whether it is artifact or information. This study attempted to conduct a qualitative analysis of the cavitation related signal using an optical hydrophone.

High-Speed Imaging

High-speed photography is a typical and powerful method for visualizing ultra-fast

phenomena such as cavitation behavior (Figure 1.4e) (Lauterborn and Timm, 1980; Chen *et al.*, 2006). It is usually composed of multi-frame high speed camera, high power backlit systems, and time-sharing devices. High-speed photography provides the best resolution in temporal and spatial domain without affecting the shock wave field, in particular, it is mainly used to observe sequential bubble behavior in microsecond order (Zhong *et al.*, 2001; Ohl, 2002; Pishchalnikov *et al.*, 2011).

Schlieren technique or shadowgraphy can also visualize transient or steady state acoustic fields after the discovery of light diffraction by acoustic pressure (Hanafy and Zanelli, 1991; Schneider and Shung, 1996; Tachikawa *et al.*, 2012). They use a reflective index change of medium modulated by acoustic pressure in water (Carnell *et al.*, 1993; Carnell and Emmony, 1994; Kudo, 2015; Iijima and Kudo, 2017).

However, the configuration equipment, such as high-speed cameras, their compatible lighting devices or LASER systems and other optical components are very expensive and generally not readily available, and most previous studies were limited to study the behavior characteristics of individual or cloud bubbles over time (Sapozhnikov *et al.*, 2002; Xu *et al.*, 2008; Zijlstra and Ohl, 2008; Pishchalnikov *et al.*, 2011, Ando *et al.*, 2011; Smith *et al.*, 2012b; Zhou *et al.*, 2012). This study investigated the method of evaluating the shock wave acoustic pressure field through the cavitation bubble cloud visualized in a practical way.
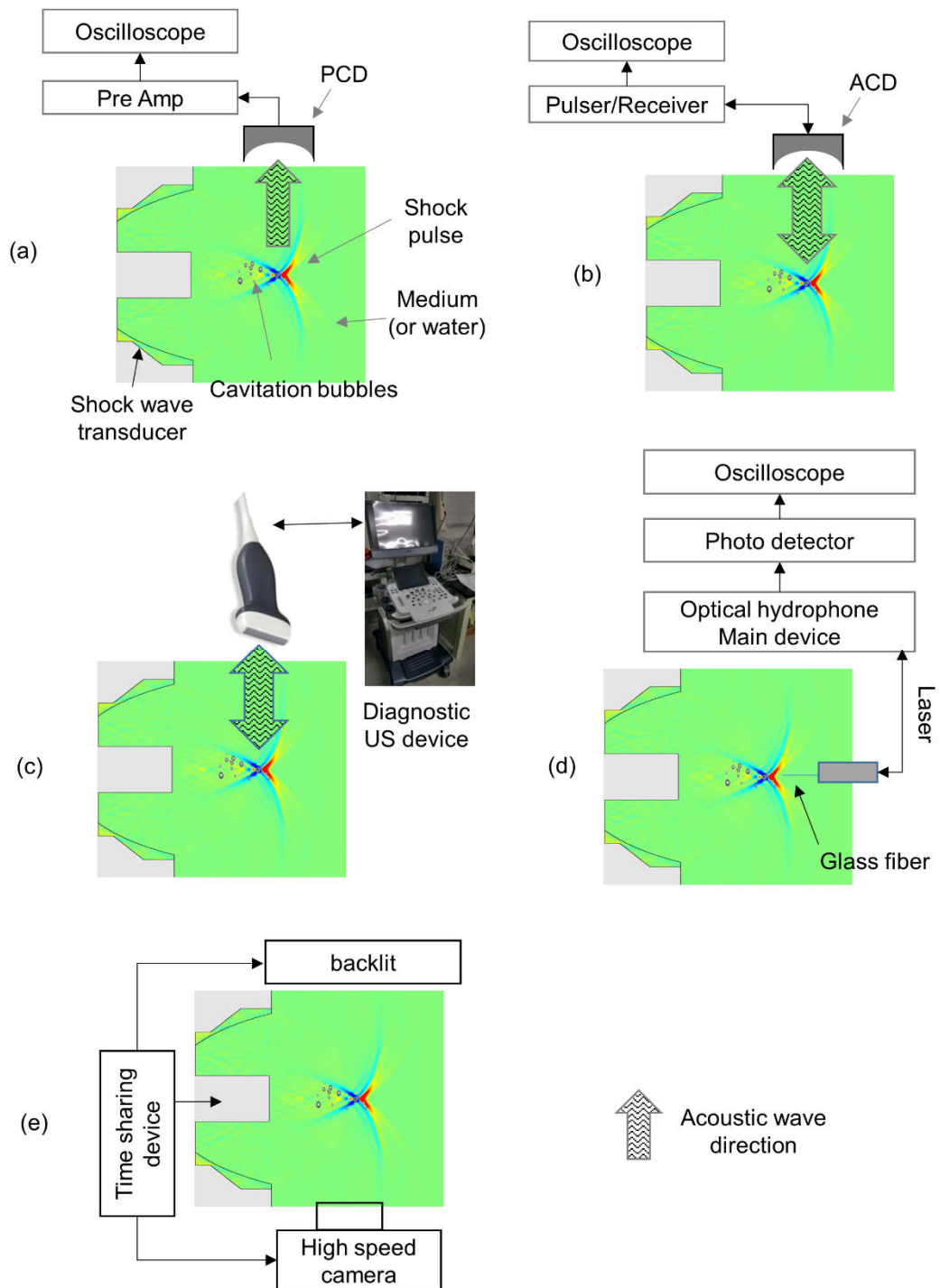
Figure 1.4 Schematic diagram of cavitation measurement setup (a) Passive Cavitation Detector (PCD), (b) Active Cavitation Detector (ACD), (c) Ultrasonic B-mode Imaging, (d) optical hydrophone, (e) High-speed imaging.

1.5 Motivation

Shock wave induced-cavitation is physically or clinically utilized or suppressed (Bailey *et al*., 2005). In a previous research, it was reported that inertial collapse of cavitation bubbles plays an important role in shock wave treatment (Coleman *et al*., 1987; Delacretaz *et al*., 1995; Pishchalnikov *et al*., 2005). On the other hand, damage to tissues and cells can be minimized by suppressing cavitation generation (Roessler *et al*., 2005; Delius *et al*., 1990; Zhong *et al*., 2001; Krimmel *et al*., 2010; Coralic and Colonius, 2013; Sankin *et al*., 2017). Therefore, a reliable method for cavitation monitoring is an important issue for both in use and restraint aspects. (Jochle *et al*, 1996; Bailey *et al*., 2005).

Most cavitation monitoring sensors can only sense the strength or occurrence of cavitation based on a single element. To evaluate the spatial distribution, a certain area is scanned or mapping technique using a plurality of sensor devices is attempted as well (Coleman *et al*., 1993; Cwik *et al*., 1993; Jochle *et al*., 1996; Cleveland *et al*., 2000). However, it is not a trivial task to quantitatively evaluate due to the chaotic behavior, ultrafast phenomenon, media-dependent characteristics and its strong destructive force (Staudenraus and Eisenmenger, 1992; Tu *et al*., 2007; Zijlstra and Ohl, 2008). And these methods take a long time to measure and the cost of constructing the measurement system makes it more difficult (Parsons *et al*., 2006). Although many previous studies have attempted to quantify the shock waves, there is no standard method that can be readily evaluated by operators in the field (Bailey *et al*., 2005; Bull *et al*., 2011; Smith *et al*., 2012b).

In order to ensure safe and to maximize therapeutic effect, it is necessary to optimize the physical dose of shock wave and to evaluate precise spatial targeting to avoid the tissue damage at undesired locations.

1.6 Specific Aims

The purpose of this study is to monitor cavitation characteristics using hydrophone signals and cavitation cloud images. In order to achieve this purpose, this study has two specific aims as follows.

The first aim is to study the interpretation of cavitation related signals recorded on an optical hydrophone. Generally, optical hydrophone is known to be suitable for measuring under high intensity and violent cavitation environment. In most previous studies regarding this subject, the researcher's interest was the main shock pressure pulse appeared in the optical hydrophone signal and how accurate it was to measure. However, we focused on interpreting the abnormal fluctuation signal, which is associated with the cavitation activities appearing after the main shock pulse waveform.

The second aim is to establish a simple experimental setup for visualization of cavitation bubble cloud and to evaluate the characteristics of the shock wave acoustic field using the acquired images. Cavitation behavior and its spatial distribution are quite chaotic phenomena, but they are closely related to the output level and acoustic field of the shock wave. To evaluate

shock wave field characteristics from cavitation cloud images, a simplified experimental setup was constructed using a long exposure photography technique that can project a bubble cloud over its lifetime in a single image in order to visualize the cavitation bubble.

1.7 Thesis Outline

This thesis consists of four chapters, including introduction, two experimental researches, and conclusions.

Chapter 1 presents the background, necessity, motivation and aims of this thesis.

Chapter 2 provides the physical background knowledge of shock waves and acoustic cavitation for this study.

Chapter 3 describes the interpretation of cavitation related signal recorded on optical hydrophone. Validation with passive cavitation detector was performed to verify the cavitation behavior. The results suggest that a single optical hydrophone can be used to measure shock pulse and to characterize shock pulse-induced cavitation.

Chapter 4 demonstrates a method for estimating the shock wave beam field through visualization of cavitation bubble cloud. It is well known that cavitation bubble is generated by the negative pressure phase of the shock pulse, and the degree of growth and the lifetime vary depending on the exposure pressure level. Cavitation bubble images were acquired using the long exposure photography technique and analyzed to investigate acoustic pressure field that related to bubble distribution.

Chapter 5 summarizes and concludes this study and suggests future works for research.

Chapter 2

SHOCK WAVE AND ACOUSTIC CAVITATION

2.1 Shock Wave

When an aircraft or a missile exceeds supersonic speed, and an underwater explosion occurs, a phenomenon described as a shock wave occurs (Cole, 1948; Zel'dovich and Rayzer, 1963). Shock waves are usually caused by changes in excessive initial conditions such as explosions or supersonic movements or by abrupt changes in high amplitude pressure waves due to nonlinear propagation (Zel'dovich and Rayzer, 1963; Hamilton and Blackstock, 1998). Shock wave phenomenon can cause serious defects in machinery and human body, so many researchers are working on the issues (Wolf, 1970; Wolfum 2004; Lance *et al*., 2015).

The waveform of shock wave pulse consists of a compressive phase (positive pressure, p+) that rises very rapidly to its peak within several tens of nanoseconds followed by a relatively long tensile phase (negative pressure, p-) as shown in Figure 2.1 (Choi *et al*., 2007; Coleman *et al*., 1991; Coleman *et al*., 1989). The amplitude of the positive phase is always greater than peak negative pressure, and there is no abrupt pressure transition in negative phase. The waveforms generated by most shock wave generators are similar in shape, but their amplitudes vary depending on the equipment configuration and applications. Since the acoustic pressure is high enough to modulate the state of the propagation medium such as density and speed of sound, as a result of these physical changes, shock wave has nonlinear

20

(a)   (b)
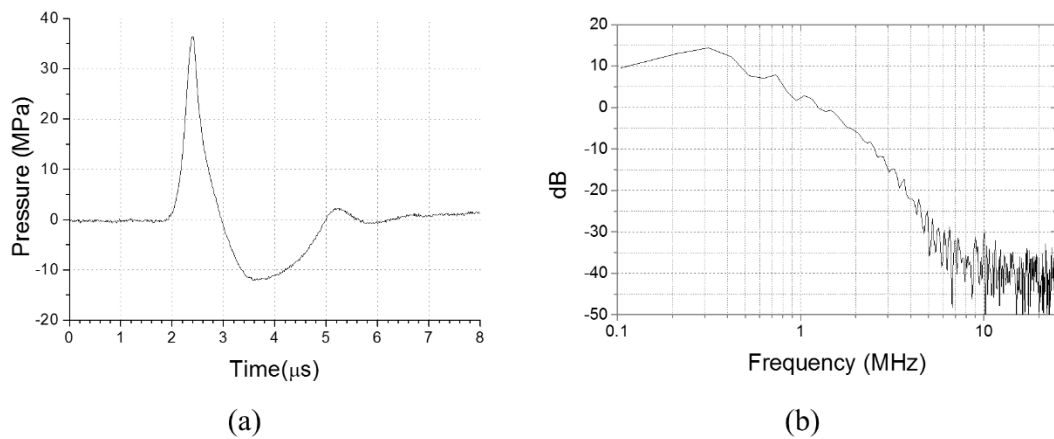
Figure 2.1 Waveform and spectrum characteristics. (a) Temporal pressure variation of a typical shock wave recorded by optical hydrophone (FOPH2000, RP Acoustics, Germany) at the geometric focus of the electromagnetic shock wave transducer (Shinewave-Sonic, HnT Medical Systems, Republic of Korea). There is a rapid pressure elevation to peak pressure followed by a decrease to zero-crossing and relatively long negative pressure, (b) Frequency distribution of shock wave using Fast Fourier Transform. The peak frequency component is found at around 300 kHz.

propagation characteristics (Smith *et al*., 2012a).

With the assumption that the density of medium does not change with time or position, acoustic waves can be described starting with a simple three-dimensional linear wave equation derived from the conservation of mass and momentum.

$$\nabla^2 P = \frac{1}{c^2} \frac{\partial^2 P}{\partial t^2}$$ (2.1)

where P is acoustic pressure, ∇ is Laplacian, t is time, and c is sound speed with constant value (Kinsler *et al*., 2000). This linear wave equation is satisfied only with a low pressure range, which can ignore the compressibility of the medium. It is no longer effective in a shock wave field where a very high acoustic pressure is formed. Because sound speed c depends on the local compression of the medium. The equations for the conservation of mass, momentum, energy, and state are followed for a compressible fluid (Blackstock, 2000; Wolfum, 2004).

Conservation of mass : $\dfrac{\partial \rho}{\partial t} + \nabla(\rho \vec{u}) = 0$ (2.2)

Momentum : $\rho \dfrac{\partial \vec{u}}{\partial t} + \rho(\vec{u}\nabla)\vec{u} = -\nabla P$ (2.3)

Energy : $\rho \dfrac{dE}{dt} = \dfrac{P}{\rho}\dfrac{d\rho}{dt}$ (2.4)

The specific internal energy E is the sum of thermal and chemical energy per unit mass. ρ is density of medium, u is the particle velocity. The Tait equation represents the relation in compressible media (Storey and Szeri, 1999).

$$\text{Equation of state :} \qquad \frac{P+B}{P_0+B} = \left(\frac{\rho}{\rho_0}\right)^n \qquad\qquad (2.5)$$

where B and n are the material depend values. P_0 and ρ_0 are the initial pressure and density respectively.

$$\text{The sound speed :} \qquad c = \sqrt{\frac{\partial P}{\partial \rho}} \qquad\qquad (2.6)$$

The local sound speed c can further be derived from the Tait equation (Eq.2.5) (Storey and Szeri, 1999).

$$
\begin{aligned}
c &= \sqrt{\frac{n\rho^{n-1}}{\partial \rho_0^n}(P_0+B)} \\
&= \sqrt{\frac{n}{\rho_0}\left(\frac{P+B}{P_0+B}\right)^{\frac{n-1}{n}}(P_0+B)}
\end{aligned}
\qquad (2.7)
$$

23

Figure 2.2 shows the nonlinear effect to a sinusoidal wave as it propagates with nonlinearity. The waveform is distorted in shape. In the absence of absorption, the wave obtains an infinite slope and then folds over and becomes multivalued. But for the last step (Figure 2.2d), this is unrealistic because multiple pressures cannot exist at one point (Smith *et al*., 2012a).
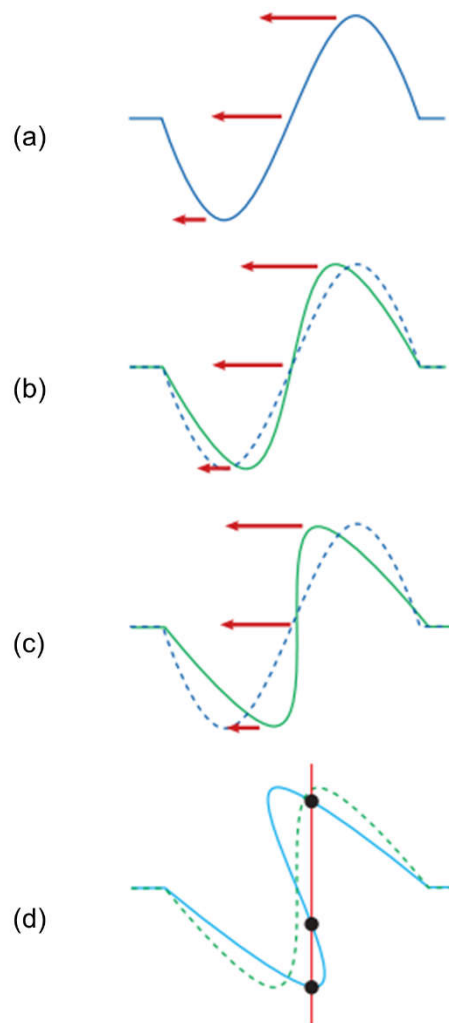
Figure 2.2 Nonlinear distortion of a sine wave due to the sound speed changes in compressible media. The length of the red arrows represents the local phase speed on the waveform. (a) initial waveform, the positive peak moves the fastest, (b) waveform at a short time from (a), dashed line indicates the waveform in (a), (c) shock formation where the slope of the wavefront becomes infinite, dashed like indicates the waveform in (a), (d) Predicted multi-valued waveform, the vertical line indicates that there are three different pressures predicted at one point in time, dashed line indicates the waveform in (c), This shape is nonphysical (Figure 49.7, p536, Smith, 2012a).

2.2 Shock Wave Generation Methods

Shock wave generator can be divided into three major types based on the technical principles named electrohydraulic, electromagnetic, and piezoelectric types shown in Figure 2.3.

Electrohydraulic type

The first model used a shock wave source in the extracorporeal lithotripsy for human and several other shock wave generators of the 1st generation equipped with an electrohydraulic (EH) sources (Chaussy *et al*., 1980). EH lithotriptor consists of a spark plug and a semi-ellipsoidal reflector with two focal points according to mathematical definition. Spark plug is aligned at the focal point F_1 in the reflector side (Figure 2.3a). When a high voltage is discharged between the two electrodes of the spark plug, plasma bubbles are generated. The plasma bubble expansion lead to spherical wave propagation with a shock front in all directions. The spherical wave towards the reflector is diverted through the conjugate focal point F_2 where all reflected acoustic energy converges to a point. Therefore, alignment of the spark plug is very important for focusing the shock waves. Otherwise, the focusing efficiency becomes lower, and the focal zone also becomes wider (Cleveland and McAteer, 2012). Although the spark plug electrodes are precisely positioned at the focal point, the plasma bubbles occur at slightly different positions at each shot because the electrodes wear and the gap between them widen, which leads to a shot-to-shot variability known as spatial and

temporal 'jitter effect' (Bourlion *et al*., 1994; Ohl, 2002). This can affect the acoustic output.

Electromagnetic type

Electromagnetic (EM) type of lithotriptor consists of a shock wave transducer composed of a cylindrical solenoid coil surrounded by a thin metallic membrane that is arranged inside a parabolic reflector (Figure 2.3b). A high voltage – high current pulse is discharged through a coil of shock wave transducer, generating magnetic field that causes in a sudden expansion of membrane, resulting in a cylindrical wave. The cylindrical wave can be concentrated onto the geometric focus after reflection off the parabolic reflector. There are no electrodes to replace in the shock wave transducer but excessive use can cause the thin membrane to degrade its elasticity or become damaged. Acoustic output of the EM type is more reproducible than that of EH type.

Piezoelectric type

Piezoelectric (PE) type uses piezoelectric ceramics and is basically the same structure that high intensity focused ultrasound (HIFU) transducer used (Figure 2.3c). Several dozen of piezoelectric ceramics are arranged inside the base in the form of a spherical cap. All ceramics are confocally focused with the geometric focus of spherical cap base. Unlike EH and EM types, PE type directly focuses acoustic energy without reflector. When a high voltage is applied to both sides of the ceramics, the ceramic expands and shrinks and generates an

acoustic pulse that propagate toward the focal point. Shock wave can be formed by constructive interference and nonlinear propagation of acoustic pulses. Burst Wave Lithotripsy (BWL) is a newly proposed with a similar driving principle. But that uses broadly focused short burst ultrasonic waves (Maxwell *et al*., 2015, Maeda *et al*., 2015). BWL generates a relatively low acoustic pressure trains rather than a strong shock pulse to produce discrete fragments rather than dust-like particles.
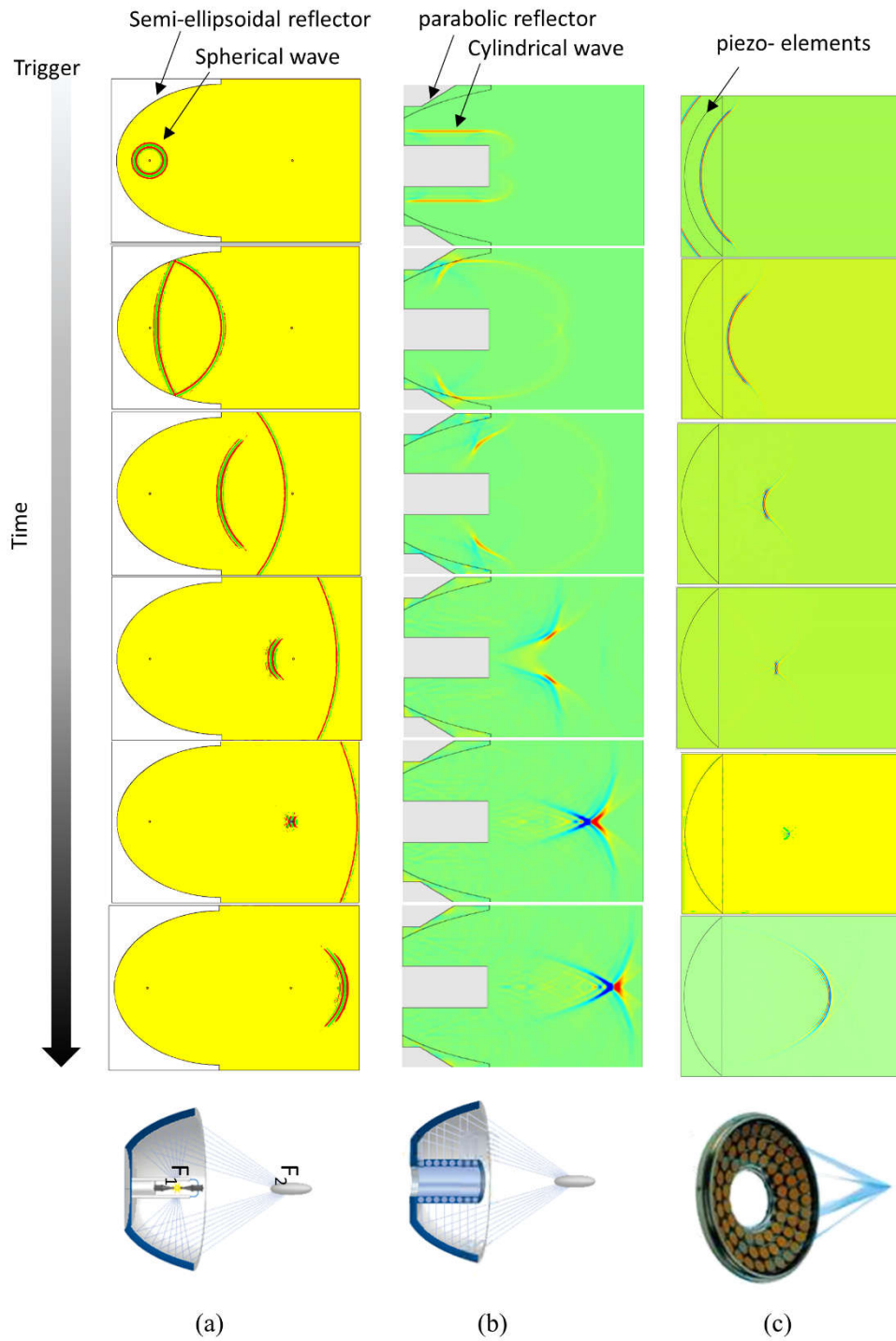
Figure 2.3 The sequence of focusing of a cylindrically diverging wave by a parabolic reflector ellipsoidal reflector. (a) Electrohydraulic type, (b) Electromagnetic type, (c) Piezoelectric type.

2.3 Acoustic Cavitation

In general, materials exist in three states: solid, liquid, and gas. Plasma has recently been added to the fourth state. The material can be transformed from one phase to another under certain conditions, mainly involving heat and pressure.

In the case of liquid, especially water, when the pressure falls sufficiently below the saturated vapor pressure at a constant temperature, water molecules are instantly separated from each other to form a vacuum known as cavitation phenomena. Acoustic wave can play this role during its negative pressure phase (Neppiras, 1980, 1984; Apfel, 1982; Webster, 1963). Water molecules are attached by hydrogen bonds, and strong negative pressures below -100 MPa are required for these bonds to separate from each other in pure water (Strasberg, 1959; Herbert *et al*., 2006; Caupin and Herbert, 2006; Menzl *et al*., 2016). However, most of the research groups reported much moderate and different pressure threshold for the inception, onset or nucleation of cavitation bubbles due to unique nuclei conditions for experimental purposes (Atchley *et al*., 1988; Webster, 1963; Herbert and Caupin, 2005; Borkent *et al*., 2009; Bull *et al*., 2013).

Acoustic cavitation induced by shock wave has a unique feature. In brief, an initial burst acoustic emission is occurred due to the positive pressure phase of the shock wave pulse. The subsequent negative pressure phase causes rapid growth of the bubble. The bubble continues to grow for a relatively long period without external pressure after the shock wave passes. The bubble then grows to its maximum size, and the ambient pressure of the fluid becomes

relatively larger than the pressure in the bubble, causing the bubble to collapse and emit the second acoustic signal (Figure 2.4) (Coleman *et al*., 1996; Zhong *et al*., 2001; Tu *et al*., 2007). Church (1989) predicted that bubbles undergo an initial collapse followed by the more violent second collapse. The time delay between the two collapses is closely related to the driving shock pressure controlled by the output setting of a shock wave generator (Cunningham *et al*., 2001; Choi *et al*., 1993). These characteristics were experimentally validated by an ultrasonic transducer, known as a passive cavitation detector (PCD) (Cunningham *et al*., 2001, Xi and Zhong, 2001; Coleman *et al*., 1992 and 1996)

To describe cavitation dynamics under shock wave pressure field, cavitation model based on the behavior of a single spherical bubble is commonly used (Church, 1989). It begins with the following assumptions.

- A free single bubble initially exists in an infinite medium.

- Bubbles maintain their shape with perfect sphere.

- The inside of the bubble is spatially homogeneous.

- The external force does not affect the bubble motion.

- Gas content inside of the bubble is constant.

- Bulk viscous is negligible.

- Thermal damping is not considered.

- The gas inside of the bubble is an ideal gas.

Temporal radius changes of a spherical bubble can be calculated by Gilmore-Akulichev

formulation as followed (Figure 2.5a) (Church, 1989).

$$R\left(1-\frac{U}{C}\right)\frac{dU}{dt}+\frac{3}{2}\left(1-\frac{U}{3C}\right)U^2=\left(1+\frac{U}{C}\right)H+\frac{U}{C}\left(1-\frac{U}{C}\right)R\frac{dH}{dR} \tag{2.8}$$

where

the radius of the bubble wall: R

the velocity of the bubble wall:

$$U=\frac{dR}{dt} \tag{2.9}$$

the speed of sound in water:

$$c=\sqrt{\frac{dP}{d\rho}}=\sqrt{c_0^2+(m-1)H} \tag{2.10}$$

the specific enthalpy of the water:

$$H=\int_{P_\infty}^{P(R)}\frac{1}{\rho}dP \tag{2.11}$$

time-varing pressure P and density ρ (Tait equation):

$$P=A\left(\frac{\rho}{\rho_0}\right)^m-B \tag{2.12}$$

A, B, and m: Empirical constant

the pressure at the bubble wall:

$$P(R)=P_g-\frac{2\sigma}{R}-\frac{4\mu}{R}U \tag{2.13}$$

the linear speed of sound in water:

$$c_0=\sqrt{\frac{Am}{\rho_0}} \tag{2.14}$$

the pressure emitted by bubble:

$$P_r(t)=A\left[\frac{2}{m-1}+\frac{m-1}{m+1}\sqrt{1+\frac{m+1}{rc_0^2}G}\right]^{2m/(m-1)}-B \tag{2.15}$$

the distance in the water from the center of the bubble: r

Bubble motion:

$$G=R\left(H+\frac{1}{2}U^2\right) \tag{2.16}$$

32

In the left side terms of Equation 2.8 represent the inertial status and the right side terms represent the action caused by the difference in pressure between bubble and water (Bailey *et al.*, 1999). The shock wave, pressure P, is applied to the bubble through C and H, since they are the function of pressure P. Figure 2.5b shows the simulation result of the bubble (R_0=3 um) response to a shock wave (P+ = 100 MPa) predicted by Gilmore-Akulichev. This model has been successfully adapted and modified in many research groups (Church, 1989; Coleman *et al.*, 1992; Bailey *et al.*, 1999; Cleveland *et al*, 2000; Sapozhnikov *et al.*, 2002; Tanguay and Colonius, 2003).
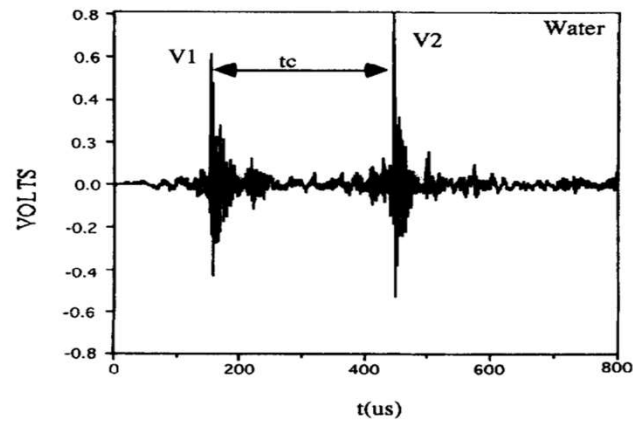
(a)
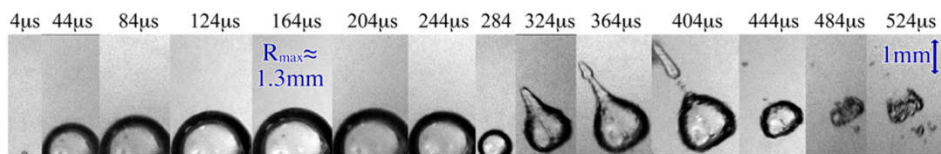
(b)

Figure 2.4 The growth-collapse-rebound cycle of a cavitation bubble (a) typical cavitation response detected by passive cavitation detector (Coleman *et al*., 1996) (b) The initial collapse of bubble was occurred between 284 and 324 μs visualized by high speed camera. (Pishchalnikov *et al*., 2011).

(a)

(b)
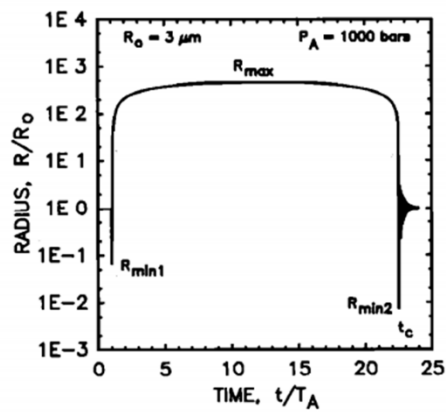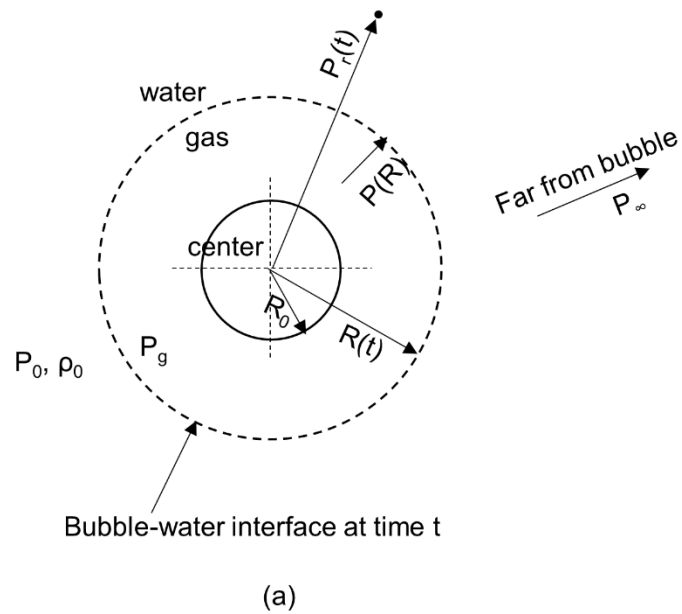
Figure 2.5 Numerical simulation of bubble dynamic model (a) Schematic of a spherical bubble in an infinite liquid, (b) temporal variation of bubble radius predicted by Gilmore-Akulichev equation (Church, 1989).

Chapter 3

CAVITATION RELATED SIGNAL ON OPITCAL

HYDROPHONE SIGNAL

3.1 Introduction

3.1.1 Abnormal Fluctuation on Optical Hydrophone Signal

As shown in Figure 2.3 of Chapter 2, no strong physical energy remains to modulate the optical hydrophone signal after the main shock pulse. Therefore, the signals after the main shock pulse were not of interest in the hydrophone signals. On the other hand, when the recording time is extended, some abnormal fluctuation after the main shock pulse signal is observed.

Figure 3.1 shows an example of the time history of an acoustic signal, which was recorded by an optical hydrophone located at the focus in water when the shock pressure pulse was generated by a clinical ESWT system. The shock pulse initially appears and last for about 5 μs. The first abnormal fluctuation signal appears within several μs after the shock pulse, and then falls to the baseline, and the second abnormal fluctuation signal appears thereafter. Even under the same experimental conditions, the amplitude and shape of the signals vary from one measurement to the next, even if the shock pulse signal is constantly measured without significant changes. This is a characteristic signal that occurs only in optical hydrophones

(Smith *et al*., 2012b).

3.1.2 Motivation

Is this abnormal fluctuation signal an artifact that interferes with interpretation or information that contains physical phenomena?

A shock pressure pulse in water changes the density of water, which modulates the optical refractive index. A change in refractive index is measured by light reflection at the tip of the glass fiber submerged in water. The loss of water contact by cavitation bubbles at the fiber tip leads to an abnormal increase of light reflection. Hence sudden saturation signal emerging after the shock pulse is closely related to the shock pulse-induced cavitation bubble activities.

A hydrophone initially senses large pressures of shock pulse before it is exposed to the inertial collapse of bubbles induced by shock pulse (Choi *et al*., 2012). Therefore, the signal recorded by a hydrophone is characterized by shock pulse followed by a characteristic tail after a few microseconds.

The tail has large, complicated, and long-lasting amplitude variation for an order of magnitude longer than the shock pulse length. The tail is expected to contain information about shock pulse-induced cavitation bubble activity. However, these data are not considered during shock pulse measurement in previous studies.
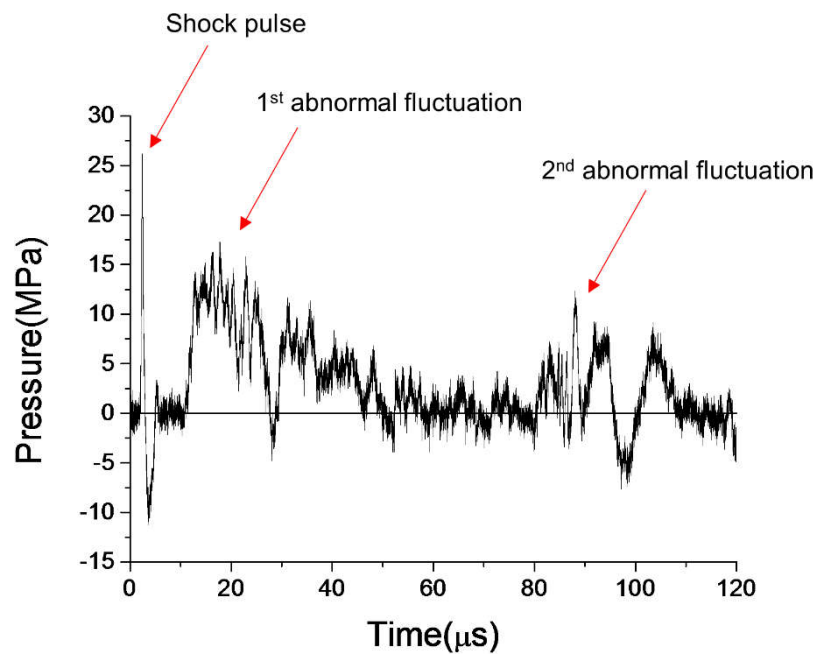
Figure 3.1 A typical time history of the acoustic signal recorded by an optical fiber hydrophone located at the focus in water when the shock pressure pulse was generated by a clinical ESWT system. The shock pulse that appears first lasts for about 5 μs and produces cavitation bubbles accompanied by broad band acoustic emission called the first collapse. The light reflected by the bubbles in front of the optical fiber tip results in a strong and long-lasting optical signal output (cavitation-related signal) that contains a violent inertial collapse called the second collapse.

3.1.3 Aim

This study considers the signal recorded for several hundred microseconds by an optical hydrophone that contains the shock pulse and the subsequent signal resulting from the light reflection of the cavitation bubbles induced by shock pulse. The present study aimed to measure shock pressure pulse and, at the same time, to characterize shock pulse-induced cavitation activities. Experimental validation was performed in the shock pulse field generated in water by a clinical ESWT system (ShineWave-Sonic, HnT Medical System, Republic of Korea) using an optical hydrophone (FOPH2000, RP Acoustics, Germany). The shock pressure pulse and the resulting cavitation bubble activities were simultaneously recorded using a single hydrophone. This allowed us to evaluate the cavitation activities in relation to the driving shock pulse.

3.2 Materials and Methods

The experimental setup is composed of a shock wave generator, an optical hydrophone, a digital oscilloscope, and a PC is shown in Figure 3.2.
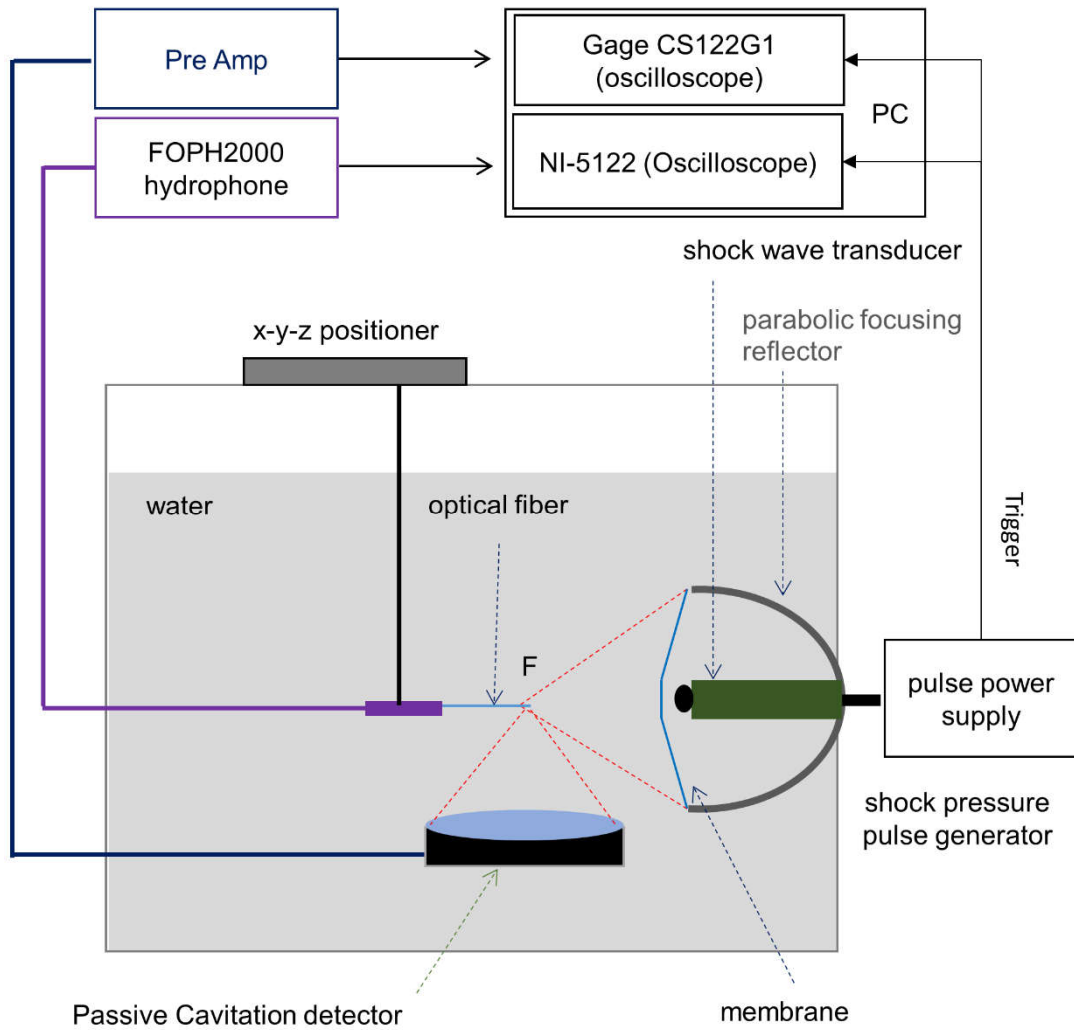
Figure 3.2 An experimental setup composed of a shock pulse generator, an optical fiber hydrophone, a digital oscilloscope for signal acquisition, and a PC for signal processing.

3.2.1 Shock Wave Generator

A clinical electromagnetic (EM) ESWT system (ShineWave-Sonic, HnT Medical System, Republic of Korea) was used as a shock pulse generator (Figure 3.3). The shock pulse generator is divided into a pulse power supply unit and a shock wave transducer with a parabolic focusing reflector (Cho *et al*., 2007; Cho, 2008). A photo graph of the ESWT system is shown in the upper right corner of Figure 3.3. This system employs an EM cylindrical shock wave generator whose simplified equivalent circuit diagram is presented in Figure 3.3. A capacitor (0.15 μF) charged up to 20 kV is discharged through a shock wave transducer, which is simply a solenoid surrounded by a metallic membrane between which a thin membrane insulator is placed (Cho, 2008; Choi *et al*., 2001; Lee *et al*., 2001). A strong current pulse (~10 kA) flowing through the solenoid, induces an EM force that enables the metallic membrane to vibrate, which eventually results in a mechanical pulse (Choi *et al*., 2011; Johnk, 1988). The pulse diverges spherically and is focused on a target location using a parabolic reflector (not shown in Figure 3.3 but plotted in Figure 3.2). The shock wave energy is controlled by the charging voltage, which is scaled as the setting number for users ranging from 1 to 7. The detailed description of the shock pulse generator is provided in our previous works (Choi *et al*., 2011; Cho, 2008; Cho *et al*., 2007).
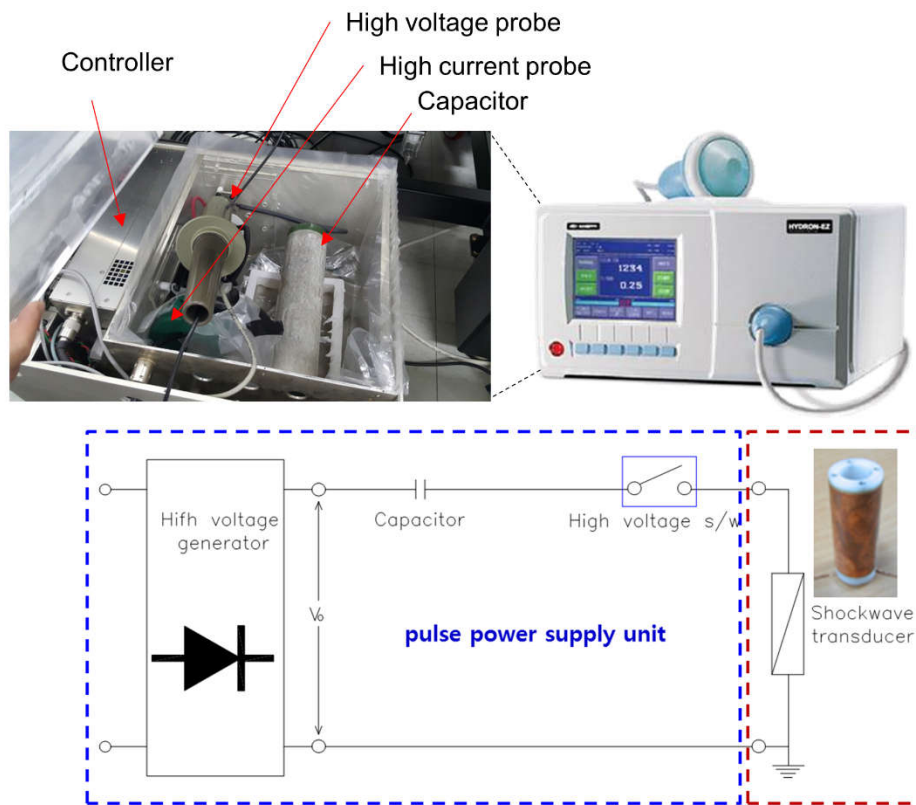
Figure 3.3 A schematic diagram of the shock pressure pulse generator employed in a clinical

ESWT system (ShineWave-Sonic, HnT Medical System, Republic of Korea)

3.2.2 Fiber Optic Probe Hydrophone

Figure 3.4 shows a photograph of the wide band optical hydrophone (FOPH2000, RP Acoustics, Germany) consisting of the main unit of the hydrophone and the photodetector. The figure also shows a schematic principle of the pressure detection via light reflection at the tip of the optical fiber [https://www.rp-acoustics.de/english/Hydrophone_FOPH2000.htm (last viewed 29 March 2018)]. The Fiber Optic Probe Hydrophone (FOPH) is preferred for the measurement of shock pulses because of its wide bandwidth and the absence of EM noises (Choi *et al*., 2007; Staudenraus and Eisenmenger, 1993; Pishchalnikov *et al*., 2016).

Figure 3.5 shows the structure of the glass fiber used in the FOPH. The glass fiber consists of a core which is a transmission path of light, a clad that surrounds the core so that light does not come out, and a coating portion that protects them. The LASER rays irradiated into the glass fiber with the incidence angle for the total internal refraction is refracted at the core-clad interface and advances without loss. To satisfy the condition for total internal reflection in the optical fiber, LASER must be incident within a critical angle θ_c described by Snell's law.

$$\frac{\sin\theta_2}{\sin\theta_1} = \frac{n_{cl}}{n_c} \tag{3.1}$$

$$\theta_2 = \sin^{-1}\left(\frac{n_{cl}}{n_c}\sin\theta_1\right) \tag{3.2}$$
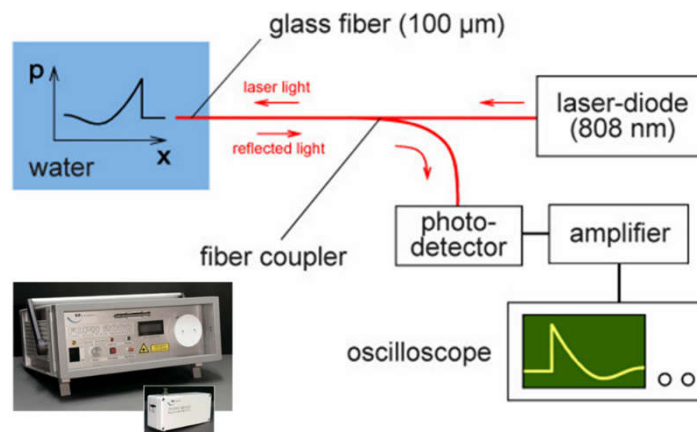
Figure 3.4 The schematic principle and photograph of an optical fiber hydrophone FOPH2000 [https://www.rp-acoustics.de/english/Hydrophone_FOPH2000.htm (last viewed 29 March 2018)].
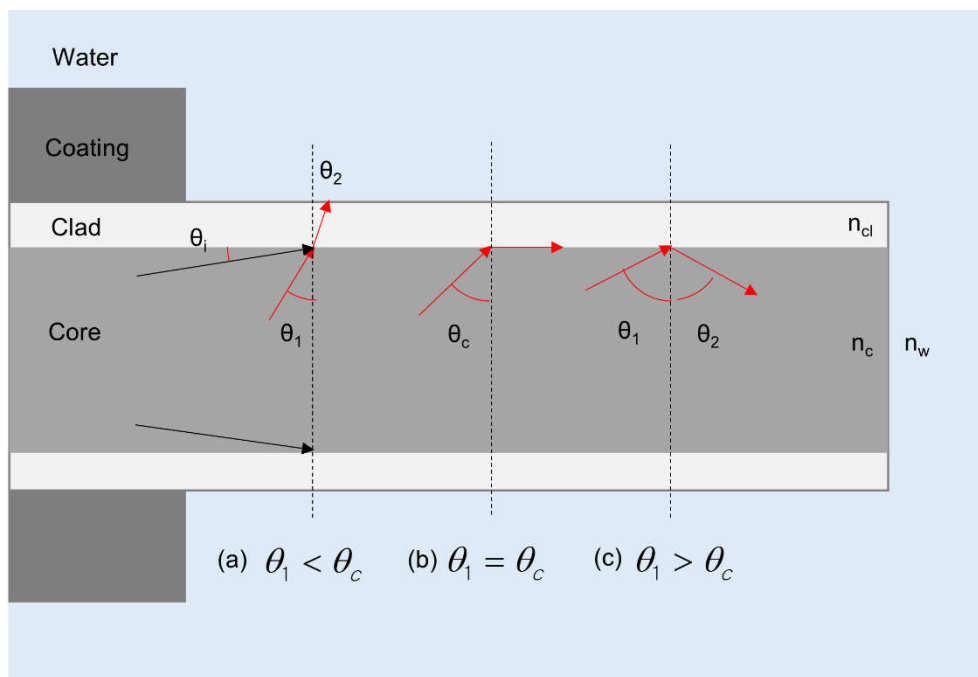
Figure 3.5 The structure of glass fiber and principle of light transmission through glass fiber.

(a) refraction angle, (b) critical angle (=81.2°), (c) total internal reflection angle.

Where n_c (=1.453) and n_{cl} (=1.436) are the refractive indices of glass fiber core and clad, provided by manufacturer of FOPH2000, RP acoustics, Germany. The refractive index is the ratio of the light speed in medium respect to the light speed in vacuum (n_{vcc}=1.0). θ_1 and θ_2 are incidence and refraction angles, respectively. The critical angle θ_c (=θ_2) for glass fiber is 81.2°.

The basic principle of FOPH is to measure the intensity of the laser beam reflected at the glass fiber tip – water interface. The reflectivity R is determined by the difference in the speed of light in the optical fiber and water, which follows the Fresnel relation at normal incidence light.

$$R = \left(\frac{n_c - n_w}{n_c + n_w} \right)^2 \qquad (3.3)$$
$$= 0.2\%$$

Where n_w (=1.329 at 20 ℃) is the refractive index of water. When cavitation bubble touches the glass fiber tip, reflectivity R becomes its maximum (= 3.36 %) where the refractive index of air n_{air} is 1.003. Since the compressibility of the optical fiber is negligibly small, n_c is regarded as a constant and it was already emphasized in the original description of the FOPH (Staudenraus and Eisenmenger, 1993). On the other hand, n_w is function of density, and can be converted into density following Gladstone-Dale relation (Figure 3.6a) (Davison and Graham, 1979; Yadav *et al.*, 1973).

$$\rho = \rho_0 \left(\frac{n_w - 1}{n_w^0 - 1} \right) \tag{3.4}$$

The isentropic Tait equation is used to connect density of water and pressure.

$$\frac{P + Q}{\rho^\gamma} = \text{constant} \tag{3.5}$$

Where, $P = P_0 + p$, P_0 is static pressure, p is acoustic pressure, $Q = 295.5 MPa$, $\gamma = 7.44$ for standard conditions ($T = 20$ ℃, $P_0 = 0.1$ MPa, $\rho = 1000$ kg/m^3) (Figure 3.6b) (Staudenraus and Eisenmenger, 1993). As a result, absolute acoustic pressure can be calculated by measuring reflectivity R (Figure 3.6c and 3.6d).
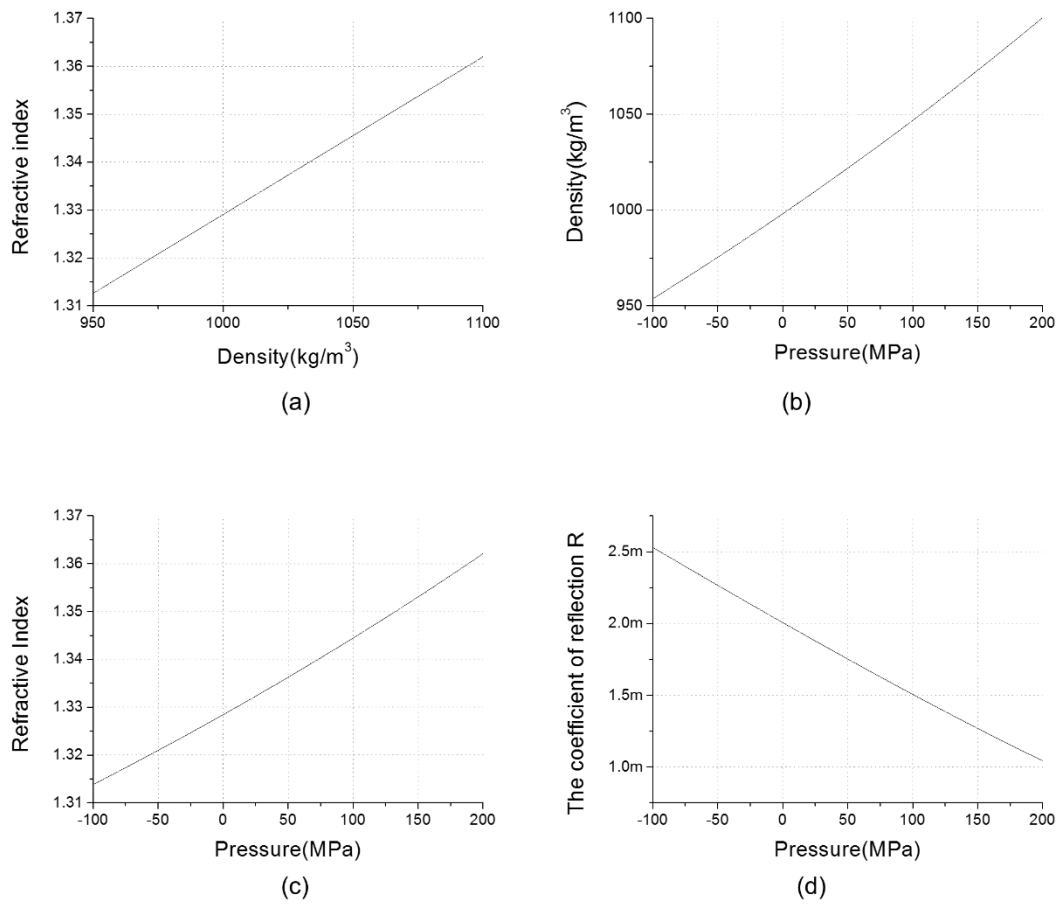
Figure 3.6 The relation of light reflectivity and acoustic pressure. (a) Density vs Refractive index, (b) Pressure vs Density, (c) Pressure vs Refractive index, (d) Pressure vs Reflectivity R

3.2.3 Shock Wave Acquisition

The water tank was filled with tap water used as the shock wave propagation medium. The water was filtered using a 5 μm filtering system for 10 h (AIMS water conditioning system, NTR systems Inc., USA) to remove impurities that act as possible cavitation nuclei. The water was then left at room temperature (20 ℃) overnight for natural degassing before use.

The signal sensed by the optical hydrophone was acquired by a digital oscilloscope (NI-5122, National Instruments, USA) for longer than 140 μs at a sampling rate of 100 MS/s. The recording time was sufficient to contain the signal that resulted from the second collapse. The sampling rate was fast enough to capture the shock front rapidly rising to the peak positive pressure (p+) within the range of several 10 ns. The acquired signal was transferred to a PC for further processing. For reproducible measurements of the shock wave, 60 s were waited before the next pulse was triggered (Arora *et al*., 2005). Figure 3.7 shows a typical measured signal, which is characterized by a single shock pulse followed by a CRS after several microseconds. CRS is a result of the abnormal light reflection of the cavitation bubbles. CRS increases rapidly to a maximum followed by a fluctuation that decreases with time.

Measurements were repeated 30 times as the setting level of the shock pulse generator was raised from 1 to 7 by a step size of 2. With the known features of the shock pulse-induced cavitation activities, two parameters were considered for the characterization of cavitation. The first parameter was the collapse time delay (t_c) between the first (t_1) and the second bubble collapses (t_2). The other parameter was the signal amplitude integral (SAI) with respect to time
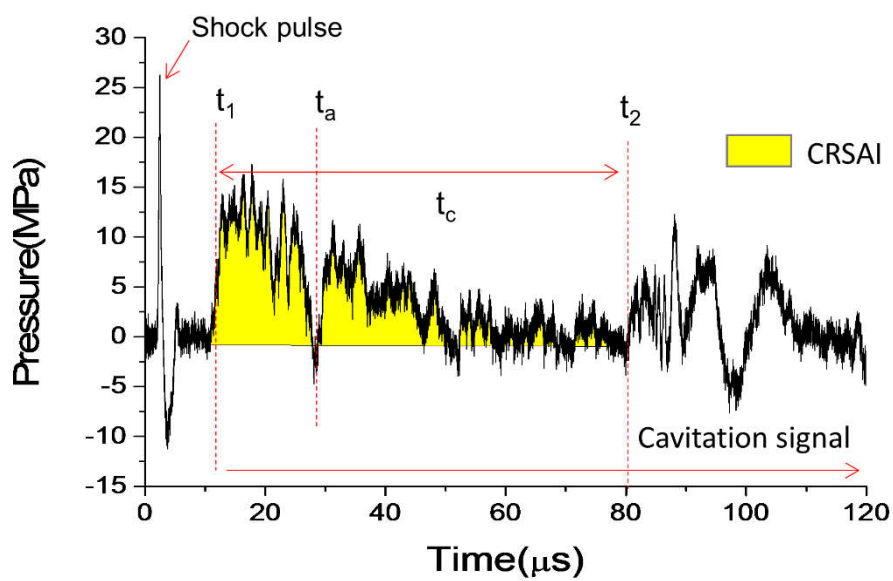
Figure 3.7 A schematic diagram to illustrate the definition of parameters used to quantify t_c and CRSAI (Cavitation Related Signal Amplitude Integral). The plot shows the characteristics of the cavitation related signal (CRS) on the optical hydrophone.

from t_1 to t_2, regarded as an index of the degree of the shock pulse-induced cavitation bubble activities (Figure 3.7).

3.3 Results

3.3.1 Acoustic Signal recorded by Optical Hydrophone

Figure 3.8 shows the time domain signals recorded with the optical hydrophone submerged in water at the focus of the shock pulse generator at setting levels of 1, 3, 5, and 7 for 140 μs. The solid line represents the mean value of 30 repeated measurements, the raw data of which are scattered to form the background shadows. The magnitudes of the shock pulse and the subsequent CRS increased as the setting level was raised. This result indicates that large shock pressure pulse engendered strong bubble activities. An acoustically silent period (ASP) was observed between the shock pulse and the CRS. The ASP shortened as the setting level increased. This reduction was not significant at the setting levels up to 5. The mean signals are compared with one another in Figure 3.8e to illustrate the characteristic features of the signals measured at different settings.
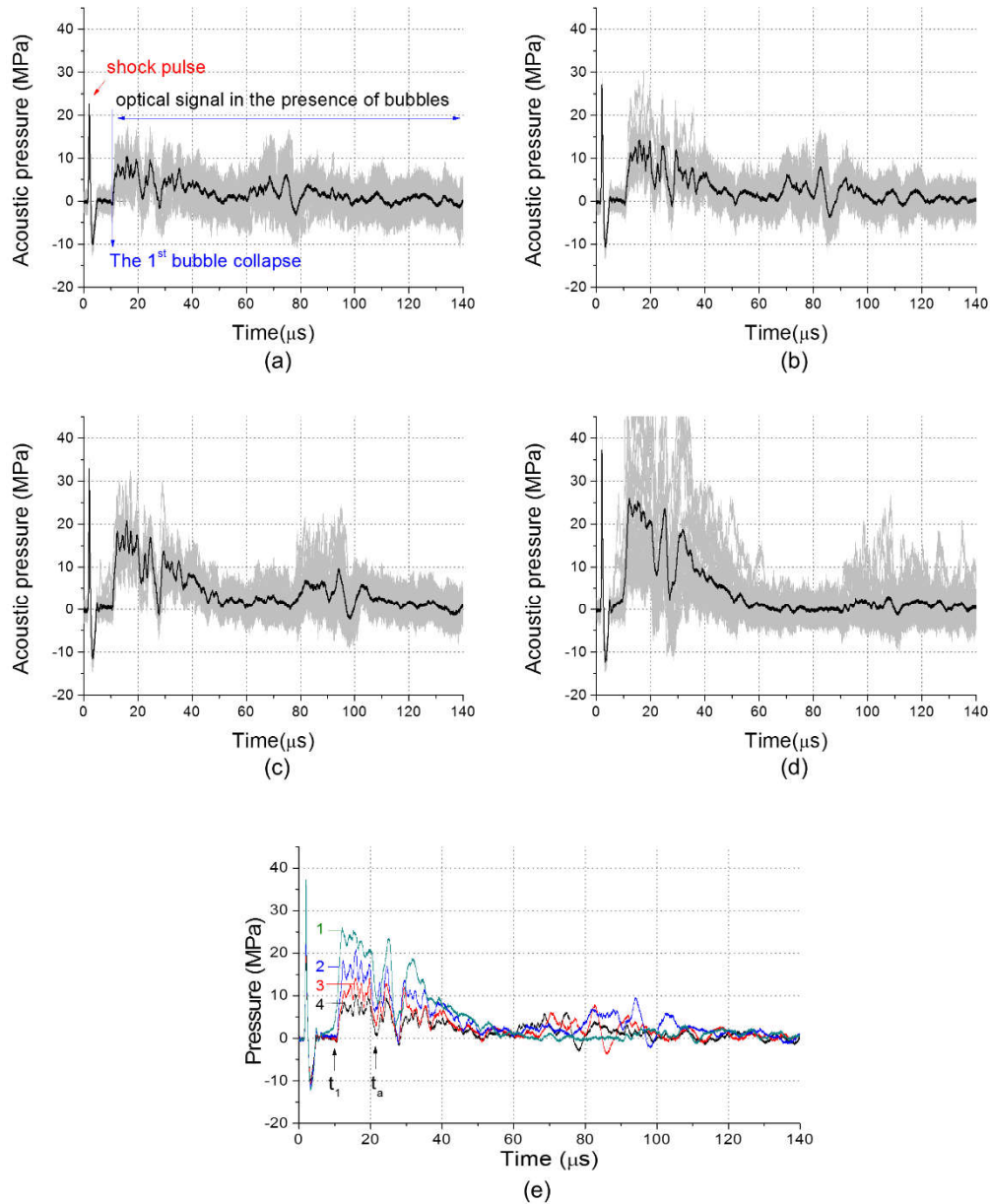
Figure 3.8 The time history of the signal recorded by the FOPH2000 optical hydrophone for the shock pulse generated in water by a clinical ESWT system at setting levels (a) 1, (b) 3, (c) 5, and (d) 7. The signal is divided into the shock pulse and the subsequent CRS which are separated through an ASP (Acoustically Silent Period). The solid line represents the mean value of the 30 repeated measurements that were plotted as background shadows. (e) Contrast among the averaged signals at different setting levels.

3.3.2 Cavitation Related Signal

As shown in Figure 3.8a the hydrophone sensed the shock pulse first. It then detected the CRS after an ASP of several microseconds. The CRS rises to a peak (smaller than p+) followed by long amplitude fluctuations that decrease with time. Figure 3.9a shows the magnified signals of shock pulses at different setting levels. The peak positive (p+) and the peak negative (p-) pressures are plotted against the setting levels in Figure 3.9b, which shows that the peak pressures vary nearly linearly with the setting levels. As seen in Figure 3.9a, the initial part of the CRS (the subsequent light reflection from the cavitation bubble after the shock pressure pulse) became strong as the setting level increased and apparently separated at different settings.

As shown in Figure 3.8e, the CRS soared to a maximum at t_1 followed by a gradual fluctuation that decreased to near zero until a noticeable oscillation reappeared at t_2 (not marked in Figure 3.8, but shown in Figure 3.10). Unlike the shock pulse, the CRS did not have negative values. The initial rise in the CRS is associated with the first bubble collapse at t_1. The reappearing noticeable oscillation which is highly significant in the time-frequency domain, is related to the second bubble collapse at t_2. In the singular time location in the CRS (marked as t_a in Figure 3.8e), the signal quickly decreased to near zero regardless of the setting levels. The ASP remained almost constant up to a setting level of 5, but it was significantly shortened at the highest setting level of 7. The second collapse time t_2 was approximately 60 ~ 110 μs after the shock pulse appeared, depending on the setting levels (as shown in Figure

3.10).

The first collapse time t_1 was easily identified in the CRS in the time domain, whereas the second collapse time t_2 was not observed clearly (Figure 3.8e). Considering the strong broadband acoustic emission during the inertial bubble collapse, the problem can be resolved by transforming the time domain signal into a time-frequency spectrogram.

Figure 3.10 shows the time frequency representation averaged for the 30 recordings of the optical hydrophone signal measured at setting levels of 1, 3, 5, and 7. The spectrograms were constructed using a MATLAB function called "spectrogram" (MATLAB 2011a, MathWorks Inc., Natick, MA). The conditions for the numerical computing included a sampling rate of 100 MS/s, a window size of 4 μs (400 samples), and an overlap between windows of 75 %. The color scale for the magnitudes of spectrogram was normalized to the peak value obtained at the setting level of 7. The arrows in Figure 3.10 identify the second collapse which was not clearly observed in the time domain (Figure 3.8).
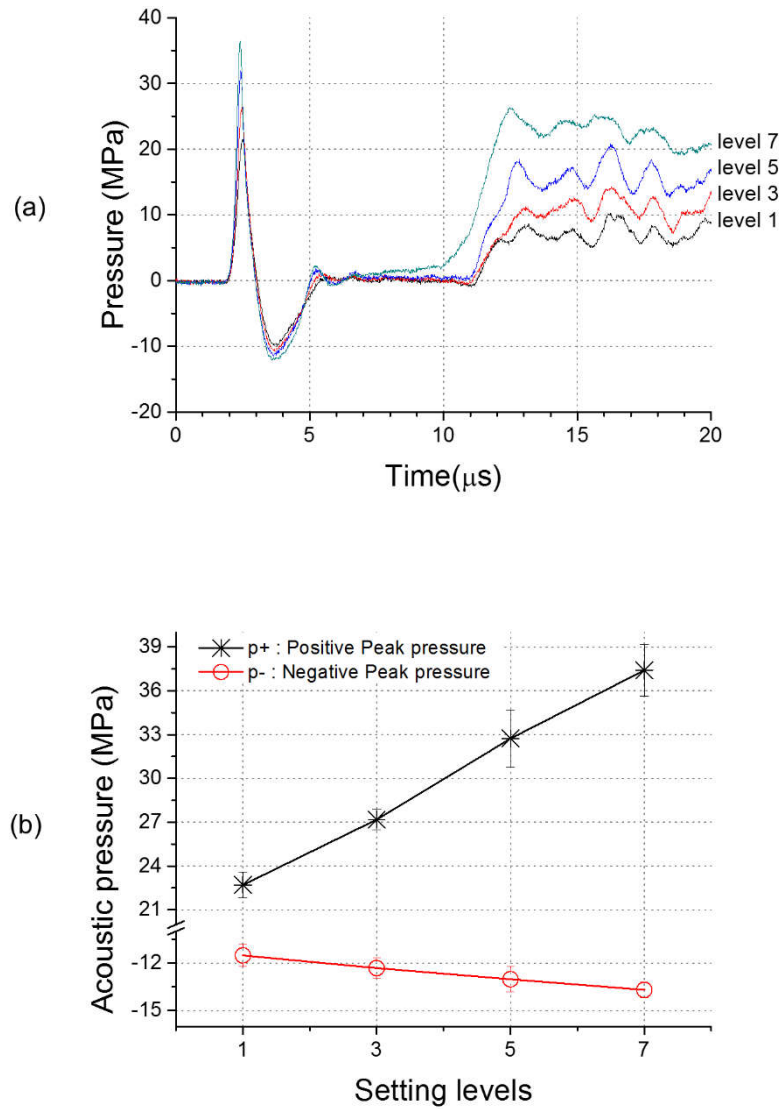
Figure 3.9 Typical signals recorded using the optical hydrophone FOPH2000 in water at different setting levels of the shock wave generator: (a) shock pressure pulse followed by the beginning part of the CRS and (b) peak positive (p+) and peak negative (p-) pressures against setting levels.
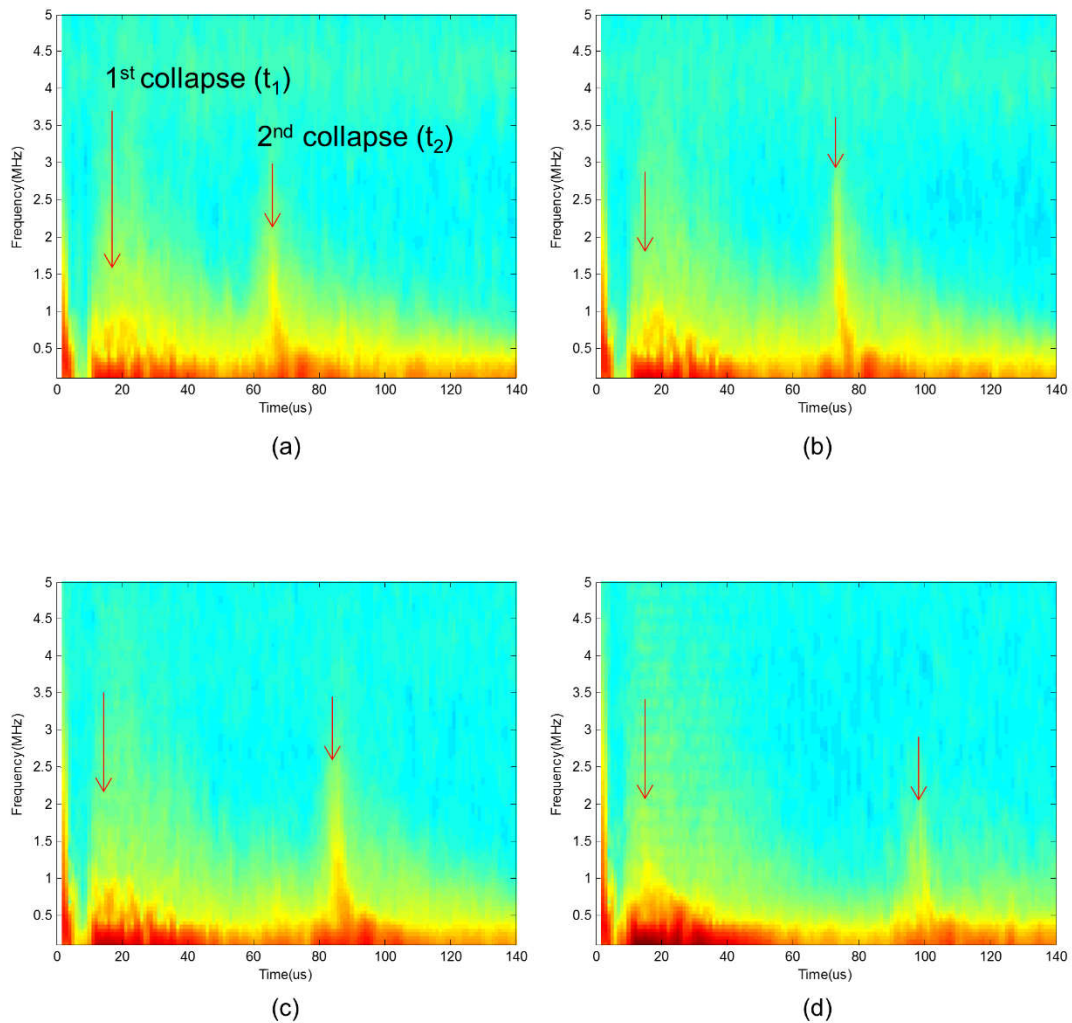
Figure 3.10 Time-frequency spectrograms averaged for the 30 recordings of the temporal variations of the signal outputs from the optical fiber hydrophone FOPH2000 at setting levels (a) 1, (b) 3, (c) 5, and (d) 7. The numerical conditions for the spectrograms included a sampling rate of 100 MHz, a window size of 4 μs (400 samples), and an overlap between windows of 75 %. The magnitude in the color scale was normalized to the peak value at the setting level of 7.

56

3.3.3 The Bubble Collapse Time, t_c

Collapse time delay t_c was measured to characterize the shock pulse-induced cavitation from the CRS:

$$t_c = t_2 - t_1 \tag{3.6}$$

where t_1 is the first bubble collapse time and t_2 is the second bubble collapse time. These collapse times are clearly identified in the time frequency representation of the CRS. In addition, Cavitation Related Signal Amplitude Integral (CRSAI) with respect to time from t_1 to t_2, which is understood to be associated with the degree of the shock pulse-induced cavitation bubble activities, was computed as

$$CRSAI = \int_{t_1}^{t_2} CRS(t)dt \tag{3.7}$$

where CRS(t) is the temporal history of the light reflection from the shock pulse-induced cavitation bubbles recorded by the optical hydrophone.

Figure 3.11 shows the mean values (N=30) of the measured collapse time delay t_c and the computed CRSAI which are plotted in the same figure against the setting level (Figure 3.11a),

57

peak positive pressure p+ (Figure 3.11b), and peak negative pressure p- (Figure 3.11c). As

expected, both t_c and CRSAI increase with the setting level or the peak pressures, which are

shown to have almost the same trend (Figure 3.11). In order to examine how closely CRSAI

is related to t_c, the CRSAI values were plotted against the t_c values. The results are illustrated

in Figure 3.12, showing that the two parameters are linearly correlated, and the correlation

coefficient is close to 1 (adjusted R^2=0.990). The standard deviations of the two parameters

are plotted as the error bars in Figure 3.12 to illustrate their variability. The variability of both

the parameters is relatively large at the highest setting of 7. The variability of CRSAI for the

setting levels less than 7 increases with the setting level, whereas that of t_c is insensitive to the

setting level.
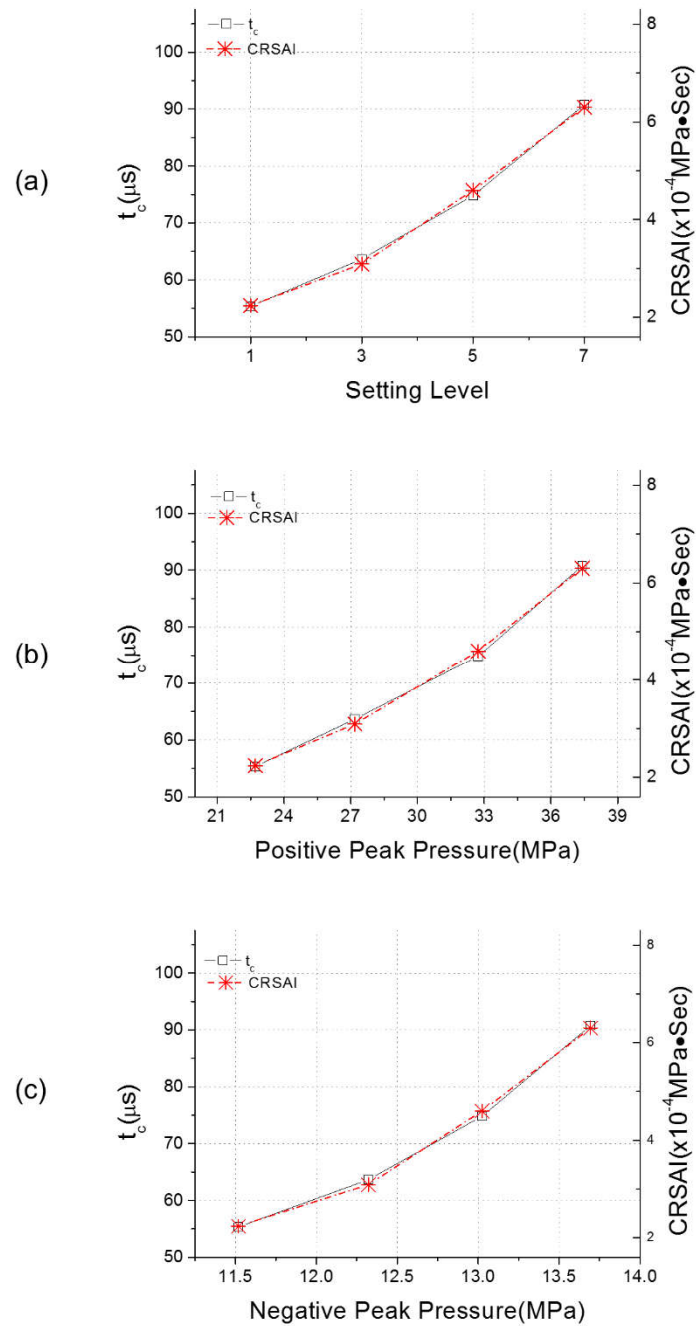
Figure 3.11 The mean values (N=30) of the measured collapse time delay t_c and the CRSAI computed by integrating the CRS amplitude with respect to time form t_1 to t_2 in relation to (a) the setting level, (b) the peak positive, and (c) peak negative pressures.
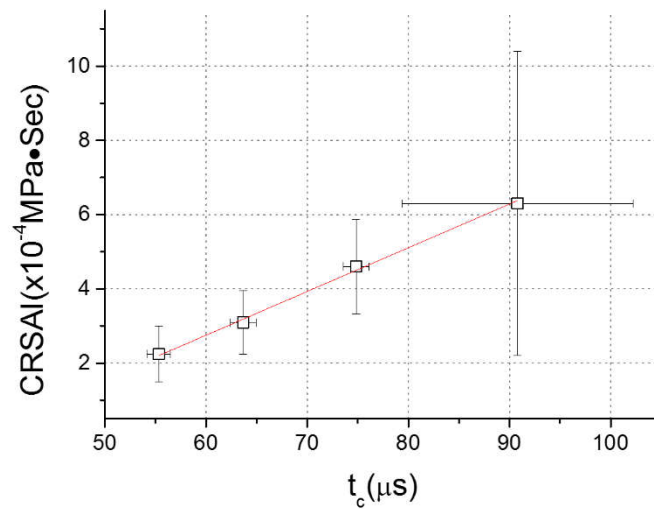
Figure 3.12 Correlation between the measured collapse time delay t_c and the CRSAI computed by integrating the CRS amplitude with respect to time from t_1 to t_2 (adjusted R^2=0.990, y=-a+bx where a=-4.318E-4, b=1.178E-5). The data point and the error bar represent the mean and the standard deviation of the 30 measurements, respectively.

3.4 Discussion

This study considered the time history of the signal sensed for a few hundred microseconds at the focus of a clinical shock wave generator using an optical fiber hydrophone.

3.4.1 Interaction between Optical Hydrophone and Cavitation Bubble Activities

The signal contained the shock pressure pulse and a characteristic tail which was associated with the shock pulse-induced bubbles. The characteristic tail, as described in the '3.1 Introduction', is attributed to the abnormal changes of the optical impedance at the fiber-water interface resulting from the existence of the cavitation bubbles. Smith *et al*. (2012b) observed that the rapid elevation in the amplitude of the tail near the first collapse was attributed to the separation of the optical fiber from water by the bubbles (Figure 9 of Smith *et al*., 2012b). This underpins that the instantaneous signal of the tail is associated with the bubble activities. The tail also contains broad band acoustic emissions resulting from the first and second bubble collapses. These emissions are unique cavitation features induced by the shock pulse. Given these conditions, the tail signal is referred to as CRS. The CRS has not been widely considered in pressure field measurement. However, this study uses the CRS to characterize cavitation bubble activities. CRS was found to last for several hundred microseconds and contain critical information on the bubble collapse and the degree of cavitation bubble activities. As reported in previous works (Choi, 1992; Coleman *et al*., 1996;

Coleman *et al*., 1992), the collapse time delay between the first and the second collapse (t_1 and t_2) is long with increasing peak pressures of the driving shock pulse. The CRSAI from t_1 to t_2, which is as an index of the degree of cavitation bubble activities, has an almost linear relationship with the t_c. This finding suggests that a single optical hydrophone signal can provide shock pressure pulse and quantities that characterize shock pulse-induced cavitation bubble activities.

The second collapse time t_2 was not clearly identified in the CRS in time domain (Figure 3.8). This problem was effectively solved by transforming the signal to the time-frequency spectrogram because the second collapse resulted in a strong broad band acoustic emission. Significant energy spread over the wide frequency (≥ 1.5 MHz) at the collapses, particularly at the strong second inertial collapse (Figure 3.10). This finding indicates that a high pass filter above 1.5 MHz can be effectively used to increase the signal-to-noise ratio when identifying t_2. Alternatively, a properly designed wavelet transformation may also be employed to detect t_c accurately, as validated in previous work (Choi, 2001). These techniques could be used as practical tools for the real time detection for collapse time.

3.4.2 Alternative Cavitation Related Signal by Amplitude Integral

A shortcoming of the CRSAI, which was introduced as a possible index of the strength of shock pulse-induced cavitation bubble activities, is its integration with the time period t_c (=

$t_2 - t_1$) which varies with setting levels. A reasonable alternative is that the integration be carried

out from t_1 to t_a ($\sim$ 20 μs), because t_a is insensitive to setting levels and remains unchanged.

This alternative is referred to as the aCRSAI, which was computed and plotted in Figure 3.13.

The aCRSAI is smaller than the CRSAI. However, the variability between the two parameters

is similar. Figure 3.14 shows the correlation between CRSAI and t_c (adjusted R^2=0.990). This

correlation was little different (smaller) from the correlation between aCRSAI and t_c (adjusted

R^2=0.999). This result suggests that CRSAI and aCRSAI virtually are the same parameters for

characterizing shock pulse-induced cavitation activities.
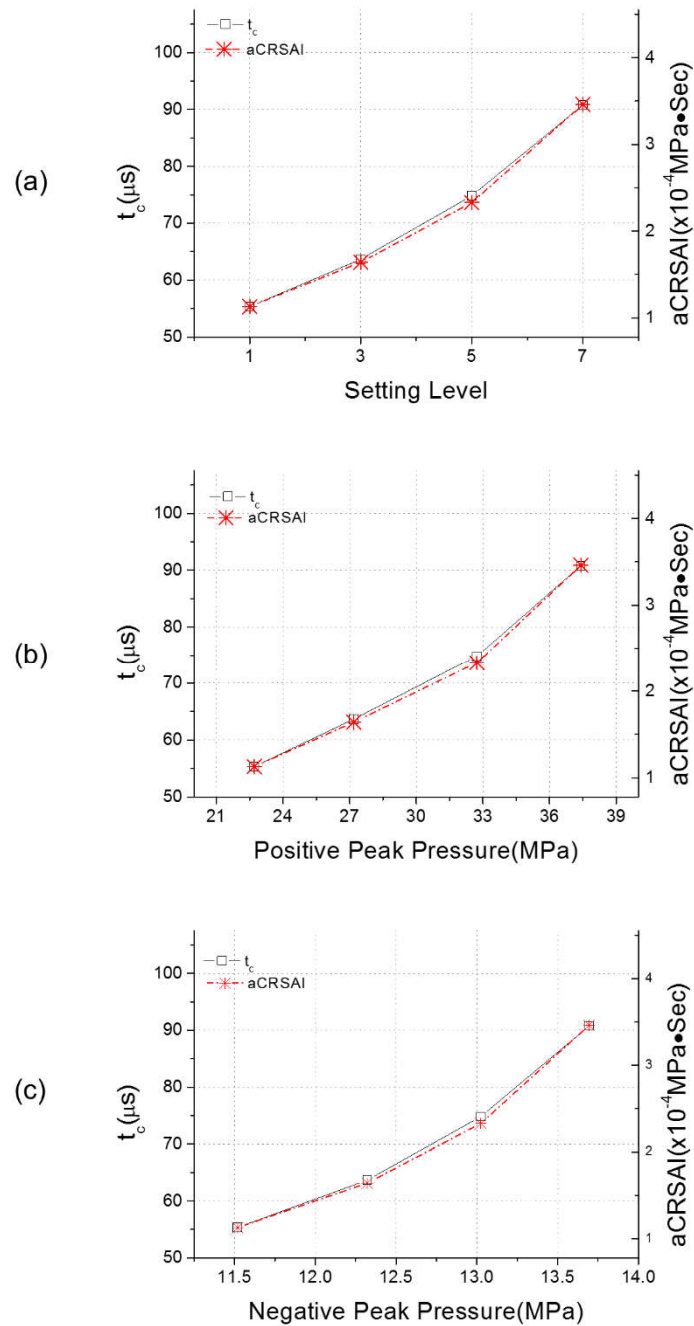
Figure 3.13 The mean values (N=30) of the measured collapse time delay t_c and the aCRSAI computed by integrating the CRS amplitude with respect to time form t_1 to t_a against (a) the setting level, (b) the peak positive, and (c) peak negative pressures.

64
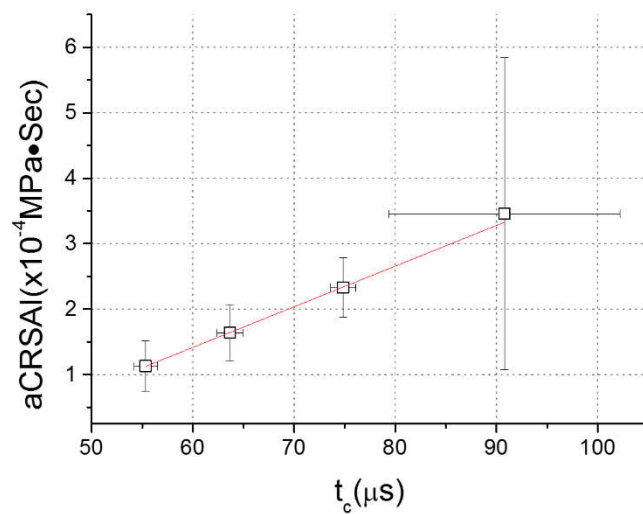
Figure 3.14 The illustration of the correlation between the measured collapse time delay t_c and the aCRSAI computed by integrating the CRS amplitude with respect to time from t_1 to t_a (adjusted R^2=0.999, y=a+bx where a=-2.312E-4, b=6.213E-6). The data point and the error bar represent the mean and the standard deviation of the 30 measurements, respectively.

3.4.3 Consideration of the Acoustic Energy

The collapse time delays measured by Coleman *et al*. (1992) are larger (>200 μs) than those shown in the present study (<100 μs). Collapse time delay or cavitation is related to the driving shock pulse that depends on the shock wave generator. The shock wave sources used in present and Coleman *et al.* (1992) studies are different. Coleman's group used an electrohydraulic shock wave generator (Coleman *et al*., 1989) identical to that employed in the Dornier HM3 commercial lithotripter. By contrast, the present study used an EM shock wave generator (Figure 3.3) employed for a clinical ESWT system. The shock wave source of the present study was employed for a clinical ESWT system, whereas that of Coleman's group was used for a clinical ESWL system. ESWL requires much more acoustic energy than that of ESWT. Figure 3.9b shows that the focal (spatial peak) peak pressures (p+, p-) from the present shock wave source are comparable to those of Coleman and Saunders (1989) used. However, the focal volume is much smaller in ESWT than in ESWL. Therefore, the acoustic energy is much larger in ESWL than in ESWT. The typical ranges of the acoustic outputs from commercial ESWT and ESWL systems are described in the work of Coleman and Saunders (1989) and Choi *et al*. (2010). As reported by Smith and Zhong (2012), cavitation correlates with the spatially averaged peak pressure. It is more closely related to the total acoustic energy than the spatial peak (focal) pressure. This suggests that the shock wave source for ESWL produces stronger cavitation than the present source for ESWT, even if the shock pulse waveforms at the focus are comparable to one another.

Caution should be taken when using the Gilmore equation (Church, 1989; Choi *et al*., 1993) to predict the collapse time of a bubble exposed to shock pulse. Such prediction with the shock pulse at the focus may lead to misunderstanding when different shock wave generators are compared. The identification of an effective driving shock pulse that can be fed to the Gilmore model so as to predict the collapse time measured for a shock wave source would be challenging.

3.4.4 Cavitation Nucleation Effect by Glass Fiber of Optical Hydrophone

The optical fiber would affect the cavitation because the optical hydrophone was submerged in cavitating water. This effect may be insignificant because the fiber tip is extremely small (100 μm in diameter). The silica-based glass fiber suppresses the occurrence of cavitation bubble due to its strong adhesion with water, even stronger than hydrogen bonding between water molecules (Staudenraus and Eisenmenger, 1993; Smith *et al*., 2012b; Zijlstra and Ohl, 2008). However, this effect may not be negligible in other types of optical hydrophone which requires a large volume of glass block instead of a fine optical fiber such as the light spot hydrophone described by Smith *et al*. (2012b) and Leitao *et al*. (2007). The membrane hydrophone may modify the cavitation activities when it is used for measuring shock pulses because the bubbles attach to the membrane. Contact-free measurement techniques, such as passive detection of cavitation (Choi *et al*., 2008; Cunningham *et al*., 2001;

Coleman *et al.*, 1996), sonoluminescence (Coleman *et al.*, 1992), high-speed shadowgraph and active light or ultrasonic transmission (Zhou *et al.*, 2012; Choi *et al.*, 2006), should be employed to avoid cavitation sources from being affected or violated. Passive cavitation detection uses an ultrasonic transducer to listen to ultrasonic emissions from cavitation and has no influence on the cavitation field itself. High-speed shadowgraph can capture a series of images of shock wave propagation and bubble dynamics (Zhou and Zhong, 2003). A laser pulse (wavelength of 512 nm for duration of 6 ns) forms a parallel beam through the focal region of the shock pulse generator via a concave lens and a Schlieren mirror (Zhou *et al.*, 2005). Images are captured with the laser, a high-speed charge-coupled device (CCD) camera, and a frame grabber. The capturing device is triggered at a time delayed after shock pulse generation. The shock pulse-induced bubble clusters may be monitored continuously by a light transmission technique. In the work of Zhou *et al.* (2005), an expanded light illumination produced by a helium-neon laser was transmitted through the focal region and subsequently focused onto a fast photodetector. The optical photography for bubble clouds or light transmission through bubbles can provide useful information on shock pulse-induced cavitation. For instance, the bubble cluster produced by a shock wave lithotripter was characterized by Zhou *et al.* (2012), and the maximum bubble radius as the cavitation potential for lithotripsy was observed by Iloreta *et al.* (2007).

3.4.5 Comparison of Bubble Collapse Time t_c between the Passive Cavitation Detector and Optical Hydrophone

Contact-free PCD can clarify the effect of the optical fiber sensor on the bubble activities via remote monitoring of the acoustic emission from cavitation bubbles. In this study, measurements for the same shock wave generator were conducted with a PCD to facilitate the validation of cavitation activities conveyed through the CRS of the optical fiber hydrophone. A focal bowl ultrasonic transducer was utilized as a PCD, resonated at 1.1 MHz and with a focal length of 62.6 mm and an aperture diameter of 64 mm (H-101, Sonic Concepts Inc., USA). Figure 3.15 shows a typical time history of acoustic emission from the cavitation bubbles recorded by (a) the optical hydrophone and (b) PCD. The figure also compares the mean values of the collapse time delays (t_c) measured 30 times by the PCD with those of the optical hydrophone FOPH2000 (Figure 311a or 3.13a). The values of t_c measured by the two methods were in good agreement for the same setting levels (Figure 3.15c). According to Zhou *et al*. (2012), passive cavitation detection is closely related to high-speed imaging of bubble clusters. Therefore, additional validation of the CRS through bubble images may not be necessary in the scope of the present study.

As validated in this study, the CRS is useful in characterizing shock pulse-induced cavitation. Note that the CRS measured in this study was at the focus. However, this condition did not limit the clarification of the CRS signal through which cavitation was related to the driving shock pulse. Shock pulse-induced cavitation activity is dependent on the location

where driving shock pulse is. Such a characteristic may indicate that the spatial distributions of the cavitation-related parameters $t_c(r,z)$ and CRSAI(r,z) can be obtained by scanning the optical hydrophone while the pressure distributions p+(r,z) and p-(r,z) are measured (note that z represents the direction along the beam axis and r represents the radial direction perpendicular to z). The distribution can be used to construct an image of where the cavitation-related quantities occur relative to the shock pulse pressure distribution. As stated previously, a hydrophone may influence the cavitation field, and hydrophone scanning is a time-consuming process. These problems may be resolved by a passive array detector (Haworth *et al.*, 2012). The probe remotely detects the acoustic signals emitted from areas containing the focus. The CRS at a location CRS(r,z,t) can be reconstructed by relocating the phase of the signal sensed by each element of the probe. The distribution of parameters $t_c(r,z)$ and CRSAI(r,z) can be computed from CRS(r,z,t) and is displayed on top of the ultrasonic image obtained by the same probe.
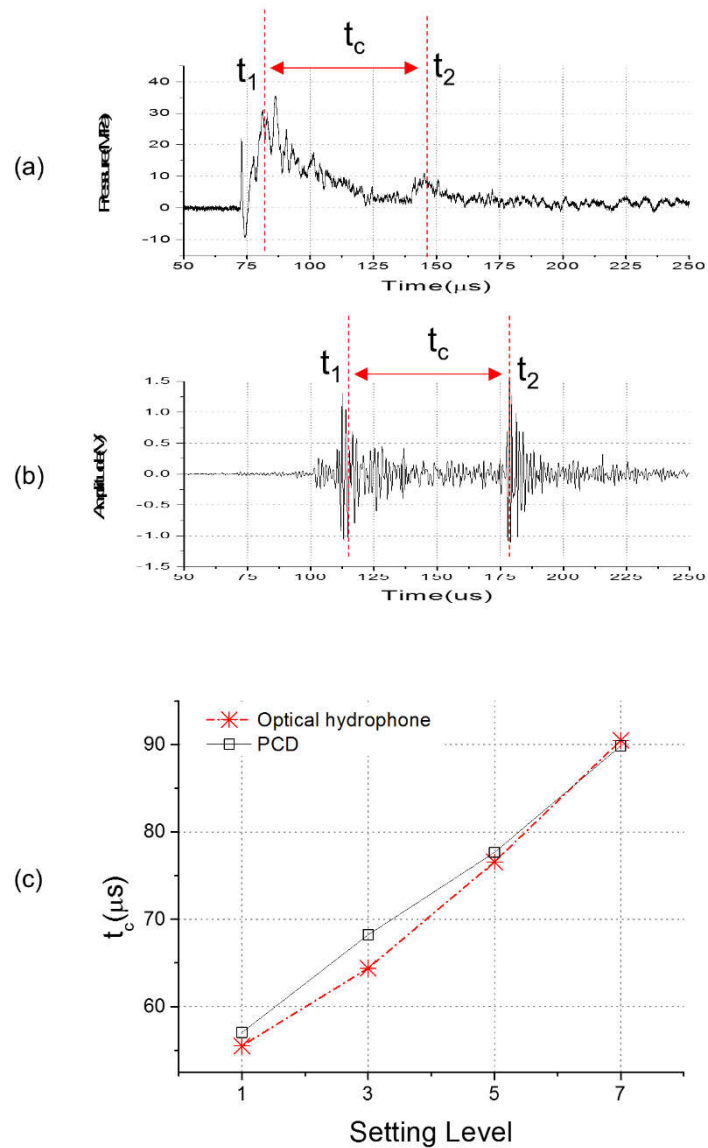
Figure 3.15 Collapse time delay t_c measured with an optical hydrophone and PCD: a typical time history of the acoustic emission from cavitation bubbles recorded by (a) the optical hydrophone and (b) PCD, and (c) contrast between the mean values of the t_c measured 30 times by the PCD and those measured by the optical fiber hydrophone (N=30).

71

3.5 Conclusion

Acoustic cavitation appears to play an important role in the therapeutic effects of an extracorporeal shock wave treatment. However, shock pulse-induced cavitation bubble activity cannot be easily measured, making it difficult to examine a quantity that may relate to a therapeutic "cavitation dose." This study considered the signal output from an optical fiber hydrophone exposed to the focal pressure field generated in water by a clinical shock wave generator. The signal was recorded for a few hundred microseconds to capture the shock pulse and the subsequent CRS. The first and the second collapse times were identified in the CRS. As expected, the collapse time delay increased with shock pulse pressures. The SAI from the first to second collapse time, which represents the degree of cavitation, was highly correlated with the collapse time delay (adjusted R^2=0.990). These findings suggest that a single optical hydrophone can be used to measure the shock pulse and, at the same time, to characterize the shock pulse-induced cavitation bubble activity. The hydrophone can also be utilized to construct an image of the cavitation bubble activity for comparison with the shock pulse pressure distribution, which may be of value in determining the therapeutic field distribution.

Chapter 4

OPTICAL MEASUREMENTS OF THE SPATIAL

DISTRIBUTION OF CAVITATION BUBBLES

4.1 Introduction

4.1.1 Pressure and Beam Profile Measurement of Shock Wave Field

Evaluating the output of the shock wave is basic and crucial to the user or the manufacturer. However, the shock wave pressure field has a high degree of difficulty due to high intensity and cavitation phenomena, which is different from the diagnostic ultrasound.

According to the International Electrotechnical Commission (IEC) standard 60601-2-36 and 61846 (IEC 60601-2-36, 2014; IEC 61846, 1998), IEC suggests hydrophone measurements for shock wave field. This document defines various parameters such as the -6dB focal zone, acoustic pulse energy, and duration, etc. The 5 MPa –focal zone is the pressure field above 5 MPa and considered as a treatment zone by definition of the Working Group Technical Developments – Consensus Report of the German Society of Shock Wave Lithotripsy (Wess *et al*., 1997) even if a threshold of medical effect is not clear.

The shock wave is strong enough to always produce cavitation bubbles which play a critical role in the desired therapeutic effects (Choi *et al*., 1993; Coleman *et al*., 1996; Leighton *et al*., 2008; Ghorbani *et al*., 2016). Accordingly, the region treated with the shock wave is

likely to be associated with the cavitation field induced by the shock wave. Over the decades, the polyvinylidene fluoride (PVDF) hydrophones have become the standard in ultrasonic measurement (Harris, 1998). Flat frequency response, high sensitivity to incident acoustic waves and high durability are the advantages of PVDF hydrophone (Granz, 1989; Platte, 1985). Narrow frequency bandwidth to detect sharp wave front, susceptibility to cavitation damage, unsuitable for sensing the strong tensile phase of a shock wave, and regular calibration due to thermal depolarization of polymer led to the emergence of new method (Harris, 1988; Eberle and Eisenmenger, 1992). To address this need, Fiber Optical Probe Hydrophone (FOPH), which consists of glass fiber, laser and photodetector, was developed. FOPH has a wide frequency bandwidth (>100 MHz), and the glass fiber is well tolerated in a cavitation environment (Staudenraus and Eisenmenger, 1993).

By optical methods, schlieren imaging, first used by Toepler (1867), is used to observe the acoustic waves together with shadowgraphy, after the discovery of light diffraction by acoustic pressure (Debye and Sears, 1932). Optical techniques can visualize acoustic field non-invasively without affecting them, and be used as tools for measurement of shockwave field (Carnell *et al*., 1993; Kudo, 2013). Quantitative measurement of acoustic power (Hanafy and Zanelli, 1991; Jiang *et al*., 2016) and attenuation coefficient (Iijima and Kudo, 2017) using optical methods were attempted in several research groups.

4.1.2 Visualization of the Cavitation Bubbles

To obtain edge clear images of bubble motion, the bubble should move less than one pixel during the exposure time (Thoroddsen *et al*., 2008). Today, ultrafast speed camera can grab images more than 1 M frames per second, which is fast enough to obtain a stop motion image of bubbles (Tomita *et al*., 1984; Tomita and Shima, 1990; Kodama and Takayama, 1998; Robinson *et al*., 2001; Pishchalnikov *et al*., 2006, 2011; Iloreta *et al*., 2007; Ohl *et al*., 2015). Such studies often require an expensive ultrafast high-resolution camera and specially designed illumination device which is currently not readily available and the number of frames that can be stored at one series is limited.

To overcome such limitations, a high speed snapshot imaging technique can be an alternative. This technique also requires a special lighting system with a very short flash time. In contrast to prior high speed imaging on cavitation, it is advantageous in cost because a relatively inexpensive camera can be used and the quality of the pictures is emphasized to resolve freezing the bubbles in stop motion. However, there is a limitation that only one image can be obtained during cavitation event so that fast transient phenomena cannot be achieved (Tomita *et al*., 2009; Zijlstra and Ohl, 2008).

Recently, an ordinary camera without light system has been used for photographing the distribution of cavitation bubbles under sonochemical luminescence as a light source. This approach is limited to the cavitation bubbles being gradually energized in a standing wave field and thus cannot be utilized in a pulsed shock wave field lasting for a short time (Yanagida

et al., 1999; Uchida *et al*., 2010).

4.1.3 Motivation

Despite the increasing attention to cavitation, its practical use is highly restricted because the chaotic nature of cavitation makes it difficult to measure. Accordingly, the region treated by the shock wave therapy is likely mapped to the cavitation field rather than the driving shock wave field. However, the performance test of the therapeutic device and the treatment planning still rely on the shock wave field, such as mean focus, acoustic focal region and acoustic intensity.

What's worse, the measurement of shock wave field requires an expensive hydrophone, time consuming scan, and high-level expertise, so that the precise information of the shock wave field is not readily available to clinical users.

In order to resolve those problems, we considered the shock wave induced cavitation field, in particular, its geometry which is expected to be effectively related to the acoustic field of shock wave transducer.

For such limited circumstances, the performance test of the therapeutic device and the treatment planning still rely on the focusing acoustic field characterized by focal intensity location, and region.

4.1.4 Aim

The aim of this study in this chapter is to investigate feasibility of optical measurement of cavitation activity using the geometrical characteristics of cavitation bubble cloud to evaluate the shock wave field which is difficult to measure.

A relatively simple, economical, and optical method was devised by which the cavitation bubbles were visualized under a micro pulse light and captured with an ordinary CCD camera. The light was set to illuminate for the time period which covers the whole life time of bubbles from formation to collapse.

The present study was focused on the geometrical aspects and quantification of the cavitation bubble images that were expected to indicate the realistic cavitation dose of the shock wave field. A clinical extracorporeal shock wave system was used to produce the cavitation bubbles. Their geometrical features were compared with those of the acoustic field to discuss characteristic similarities between them. The clinical potential of the static image of the cavitation bubbles was discussed.

4.2 Materials and Methods

4.2.1 FEM Simulation of Shock Wave Field

Numerical simulation was performed to predict the acoustic field on the vertical cross section of the shock wave transducer including the parabolic reflector shown in Figure 4.1. The technical and geometrical specifications of the shock wave generator required for the simulation were provided by the manufacturer (HnT Medical System, Republic of Korea). The numerical simulation was carried out in the time domain using PZFlex (Ver 2014, Weidlinger Associates, USA), where water was selected as the propagation medium and the nonlinear propagation was considered. The acoustical and physical properties of the propagation media such as sound speed, density, and attenuation coefficient are listed in Table 4.1.

The rectangle in the middle on the right hand side represents the shock wave transducer surrounded by the parabolic reflector. Note that the dotted horizontal line represents the shock wave propagation axis (propagating from left to right on the image) and the intersection of the dotted lines indicates the focal point.
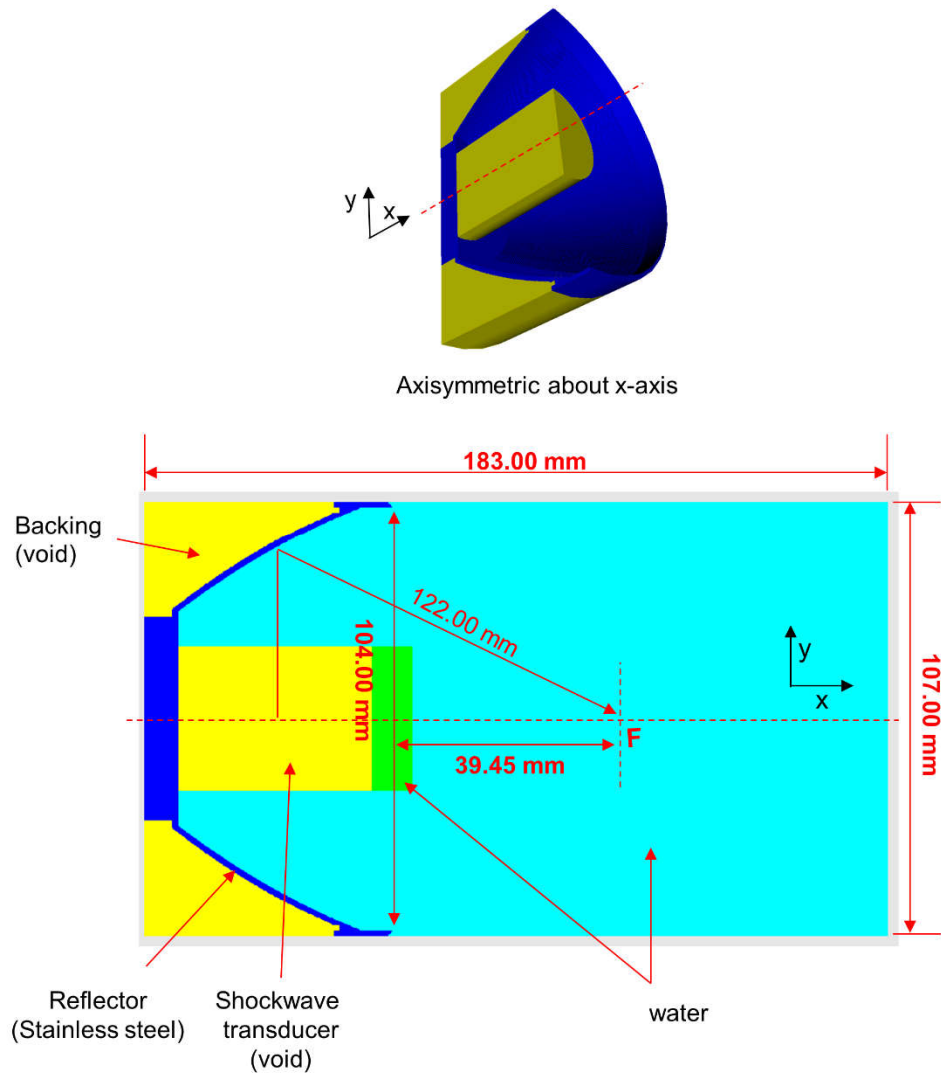
Figure 4.1 Geometry for the numerical simulation of the focusing shock wave field produced by a cylindrical shock wave transducer with a parabolic reflector.

Table 4.1 Acoustic properties for the shock wave transducer model.

Material	density kg/m3	sound speed m/s	atten. Coeff. dB/cm/MHz
Void	0	0	0
Water	1000	1500	0.002
stainless steel	7890	(bulk) 5790 (shear) 3100	0.3

4.2.2 Acoustic Output Measurement

Acoustic intensity measurement system (AIMS, NTR Systems Inc., USA) with an optical hydrophone (FOPH2000, RP Acoustics, Germany) was used to measure shock wave field. Axial and lateral 1D profile scanning was performed. Scanning range in relation to the focal point is from -25 mm to +35 mm in the axial direction and from -10 mm to +10 mm in radial direction and measured in 0.5 mm spacing. Shock waves were administered at 60 s pulse repetition period. Shock wave generator and water conditioning were described in detail in Chapter 3.2.1 and 3.2.3.

4.2.3 Long Exposure Shadowgraphy

Long Exposure Shadowgraphy (LES) is fundamentally the same as shadowgraphy with a relatively long light exposure time, which is based on the refraction of light in an inhomogeneous medium. Differences in refractive indices at gas-liquid interface distort parallel light rays and cause spatial variations in the intensity of light, which can be visualized on a screen or image sensor on the opposite side of the medium (Takeuchi *et al*., 2012). Figure 4.2 represents the basics of shadowgraphy and a typical example image for a spherical cavitation bubble in water. For a bubble, mismatch of refractive index at the air-water interface led to the strong light refraction (Staudenraus and Eisenmenger, 1993).

81

Image sensor
or
screen

Background
Light

Ray of light

Bubble
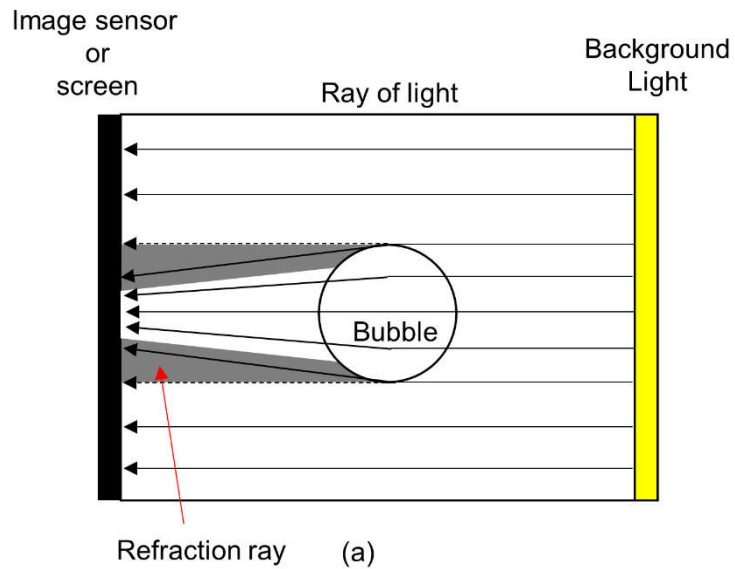
Refraction ray   (a)

Dark circle caused by refracted light from outline of bubble

image   500µm
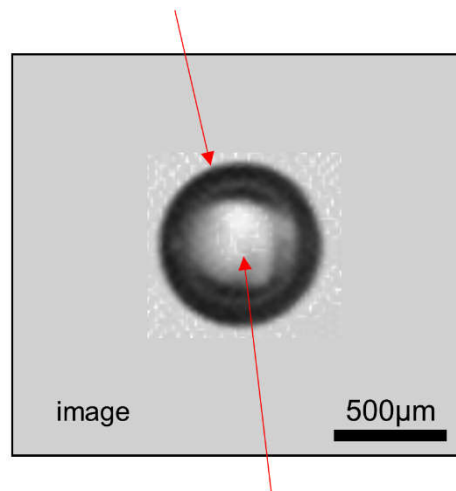
Gradient back to backlight caused by non-uniform refraction
of rays at the bubble surface.

(b)

Figure 4.2 Basic optical concept of shadowgraphy for a spherical bubble in liquid medium.

(a) refracted light from bubble outline, (b) visualized bubble image.

This phenomenon is caused by the difference in light speed between water and air. The refraction gradually decreases as the light rays reaches from outline to the center of the bubble. so that the light ray passing through the exactly center of the bubble is not refracted (Settles, 2001).

LES that has a relatively longer illumination and shutter time than the cavitation behavior and can record the motion trances during its lifetime. The behavior of bubbles over time can be typically thought of in two cases. First case is a bubble moving one place to another due to streaming caused by acoustic radiation force. The trajectory of the bubble can be recorded (Figure 4.3a). Second case is a bubble with different lifetime. The bubble that has a longer lifetime can be visualized darker and clearer than the one that has a short lifetime (Figure 4.3b).
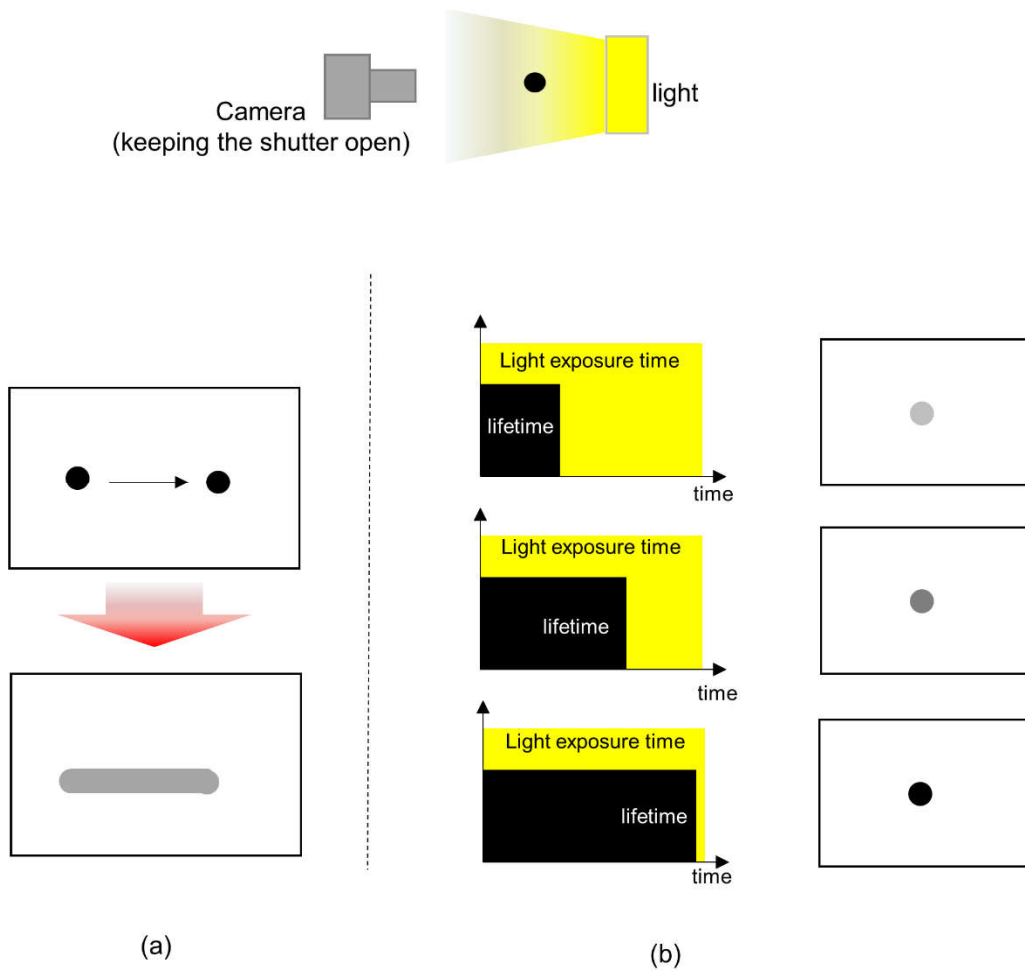
Figure 4.3 A concept of a solitary bubble image acquired by long exposure time. (a) Moving

target, (b) lifetime of target.

4.2.4 Acquisition of Cavitation Bubble Images

The cavitation visualization system is composed of a CCD camera (CM3-U3-50S5M, PointGrey, Canada) with a macro-lens, the Micro-Pulse LED Light (MPLL, KISTech, Republic of Korea), water tank (200 x 200 x 200 mm, optically transparent) and the compact vision system (NI CVS-1459, National Instruments, USA) as shown in Figure 4.4.

A CCD camera (CM3-U3-50S5M, PointGrey Research, Canada) with a macro-lens (M0824-MPW2, 2/3", 8 mm, F2.4, 57.8° HFOV, Computar, USA) was used to focus and then capture the optical images of the cavitation bubbles in the dark room. The shock wave-induced cavitation bubbles were visualized under the microsecond pulse LED light (MPLL, KISTech, Republic of Korea) illuminated for the entire lifetime of the bubbles, which was measured to be several hundred microseconds ($\sim$ 150 μs) by Kang *et al*. (2014). In particular, at the highest charging voltage of 20.75 kV used in the present study, the entire lifetime of the bubbles was observed to be no longer than 150 μs. A light diffuser was mounted in front of the MPLL to spread out light to obtain uniform illumination, resulting in homogeneous white background on the image.

When the shockwave device is triggered, compact vision system detects the trigger signal from the shockwave device, and generates TTL signal using internal 40 MHz FPGA to control CCD camera and MPLL. The CCD camera starts acquisition and after 60 μs, the MPLL emits light for 150 μs. After 60 μs, the operation of the camera stops and the image acquisition is completed (Figure 4.5).
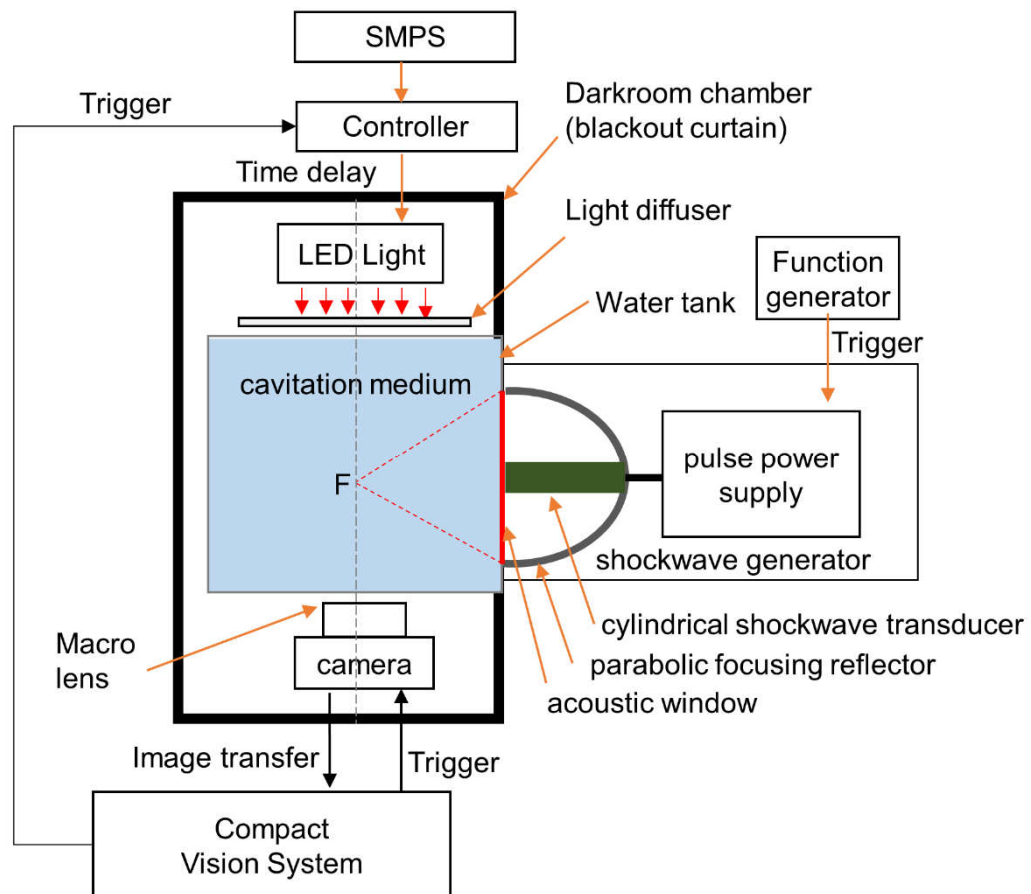
Figure 4.4 A schematic illustration of the main part of the experimental setup for visualizing the cavitation bubbles produced by the shock wave generator under a micro-pulse LED light.
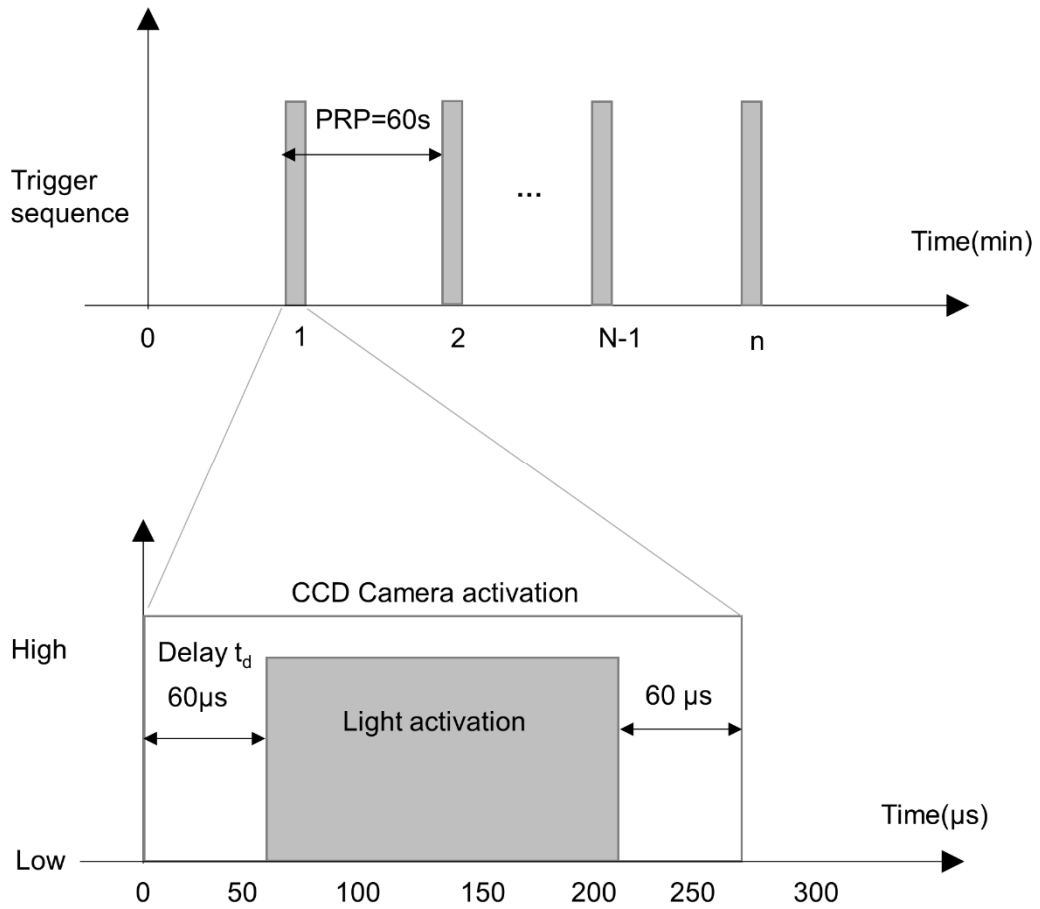
Figure 4.5 Sequential procedure to synchronize a CCD camera with micro-pulse LED light.

4.2.5 Image Processing

In order to define the size of the image, a transparent plate ruler with grids spacing of 5 mm was prepared. This ruler was captured by aligning the focus position of the camera where the cavitation occurs (Figure 4.6a). The image size is 2448 x 2048 and the resolution is 40 μm per pixel. A number of images were combined to extract the unchanging part to create a background image. Since cavitation bubbles occur irregularly in space, considering a particular coordinate (x, y) in the image, most grayscale values among n images have high level background. It also has low level due to cavitation bubble (Figure 4.5b). These low values were removed and the rest of the high values were averaged to form the background image (Figure 4.6b).

The multiple instantaneous images were obtained repeatedly and converted into grayscale format and accumulated sequentially into one image. Cavitation bubbles were expressed as low values in the grayscale of the image. Therefore, only low values were combined through acquired images (Figure 4.6d and 4.6e).

$$\mathrm{I}_{\mathrm{merged}}\left(x,y\right) = \min\left\{I\left(x,y,t\right)\right\} \tag{4.1}$$

where x, y are the coordinates of the image, and n is the image number.

After the images were accumulated, the background images were removed. For

quantification, a threshold was applied to convert into binary image. To estimate the area,

ellipse estimation algorithm provided by an image processing tool kit (Vision Development

Module 2017, National Instruments, USA) was applied to accumulated images (Figure 4.6f to

4.6h).
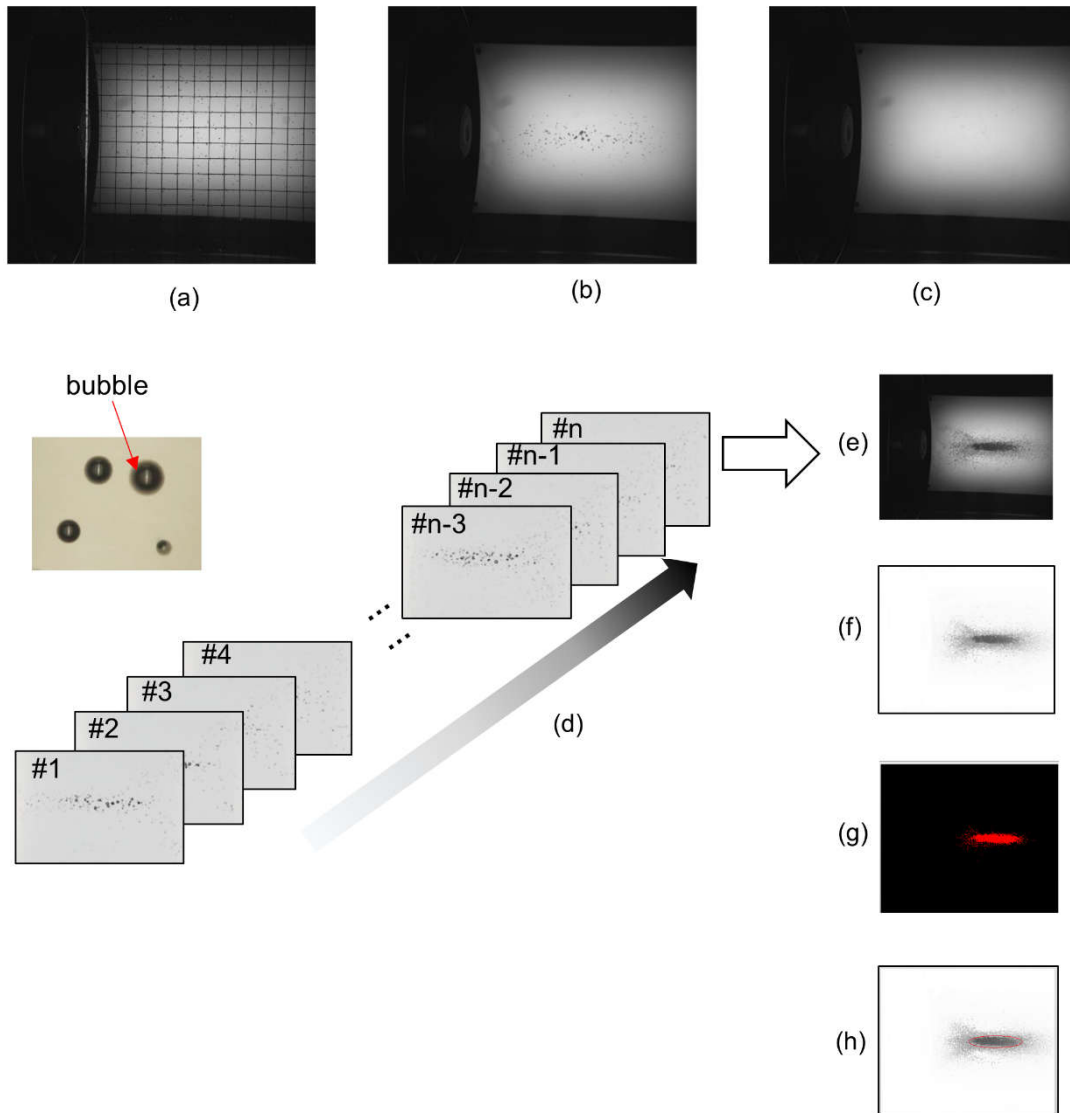
Figure 4.6 Image merging method for generating cumulative image. (a) scale image (b) instantaneous image, (c) background image, (d) sequential images, (e) accumulated image, (f) background removal image, (g) binary image, (h) Ellipse fitting image.

4.3 Results

4.3.1 Cavitation Bubble Cloud Images

Figure 4.7 depicts the optical image of the cavitation bubbles captured under microsecond pulse LED light illumination with various shock wave output levels. The light was switched on for 150 μs (from a time delay of 60 to 210 μs after the shock wave generator was triggered), which covered the entire bubble lifetime (Kang *et al*., 2014). Note that the shock wave arrived at the focus after 72 μs of triggering the shock wave device. Therefore, the time delay of 60 μs represented the time 12 μs before the shock wave arrived at the focus and the delay of 210 μs allowed the camera to capture the bubbles for their entire lifetime (<150 μs) (Kang et al., 2014). Each image represents an afterimage into which the dynamic behaviors of cavitation bubbles overlap. The repetition time of measurements was set to 60 seconds before the subsequent shock wave was generated so as to ensure that all the remaining bubbles produced by the preceding shock wave disappeared. As seen in Figure 4.7, a single shock wave produced the cavitation bubbles sparsely in the vicinity of the focus marked by a cross on each image. Note that the shock wave propagated from left to right on the image.

In order to check the variation of cavitation bubble production with time, each image was quantified using grayscale intensity representing bubble behavior. Figure 4.8a shows the sum of grayscale intensity occupied by the bubbles as the acquired image sequence number increased. Each acquired image was converted into a binary image using the histogram and

threshold method was implemented in MATLAB (R2015, MathWorks, USA). Integration of

the grayscale values was considered as the behavior of cavitation bubble cloud. The variation

of bubble production did not show a correlation with the image sequence number. As seen in

Figure 4.8a, the variation in the area did not have any tendency with the sequence number but

stayed randomly near either side of the mean value (Figure 4.8b). Based on this observation,

it is surmised that the water condition which could influence cavitation inception (or threshold)

was not significantly altered during the image acquisitions.

Shock wave direction

Image
number
#001

#010

#020

#030

#100

(a) (b) (c) (d) (e)
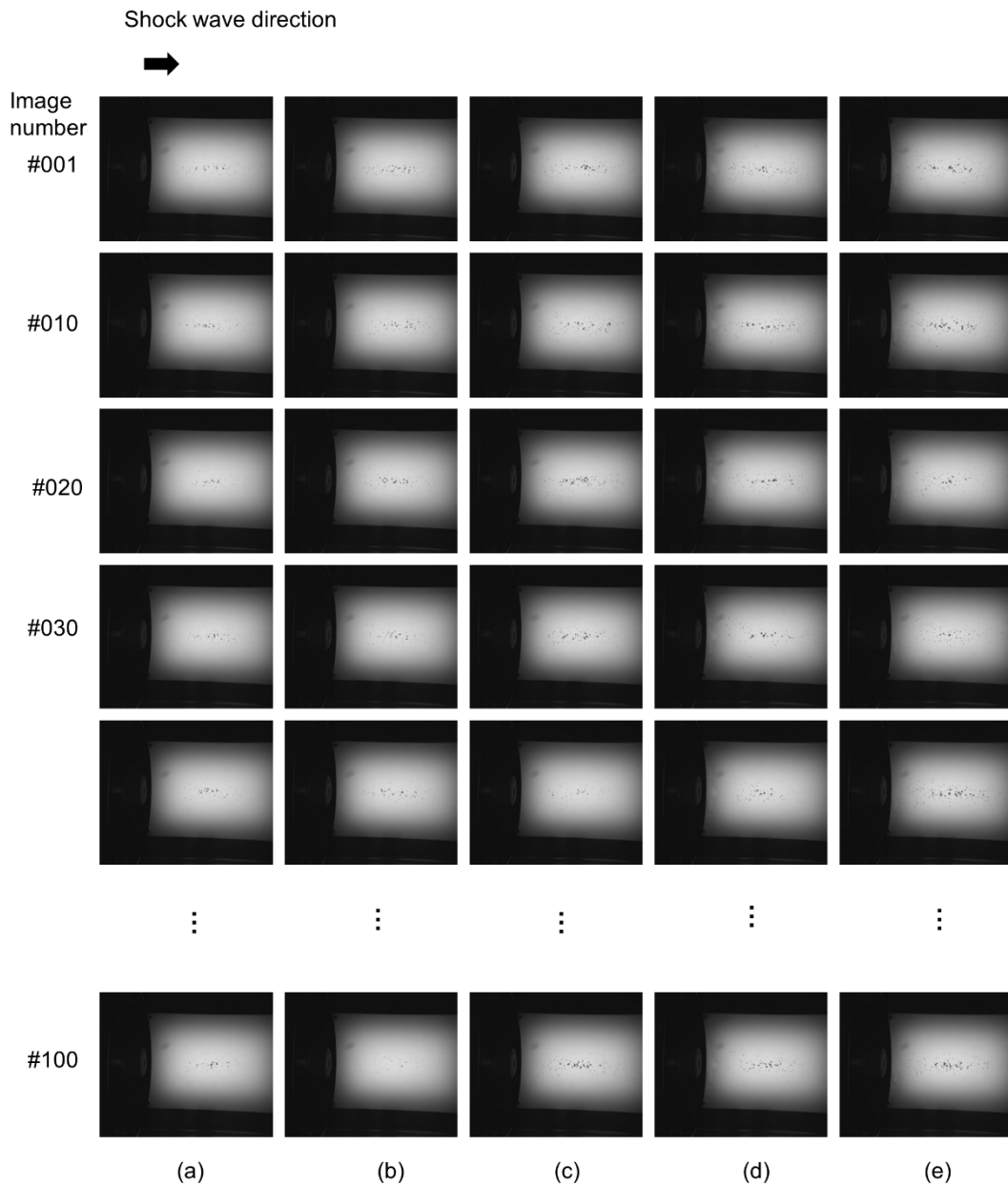
Figure 4.7 Sequential series of 100 images of cavitation bubbles captured under light exposure for the entire lifetime of bubble (60~210 µs after triggering the shock wave generator at the charging voltage (19.75 kV) of the shock wave device. Note that the interval of shock wave production was 60 seconds and the shock wave propagated from left to right. (a) Level 1, (b) Level 3, (c) Level 5, (d) Level 7, (e) Level 9.
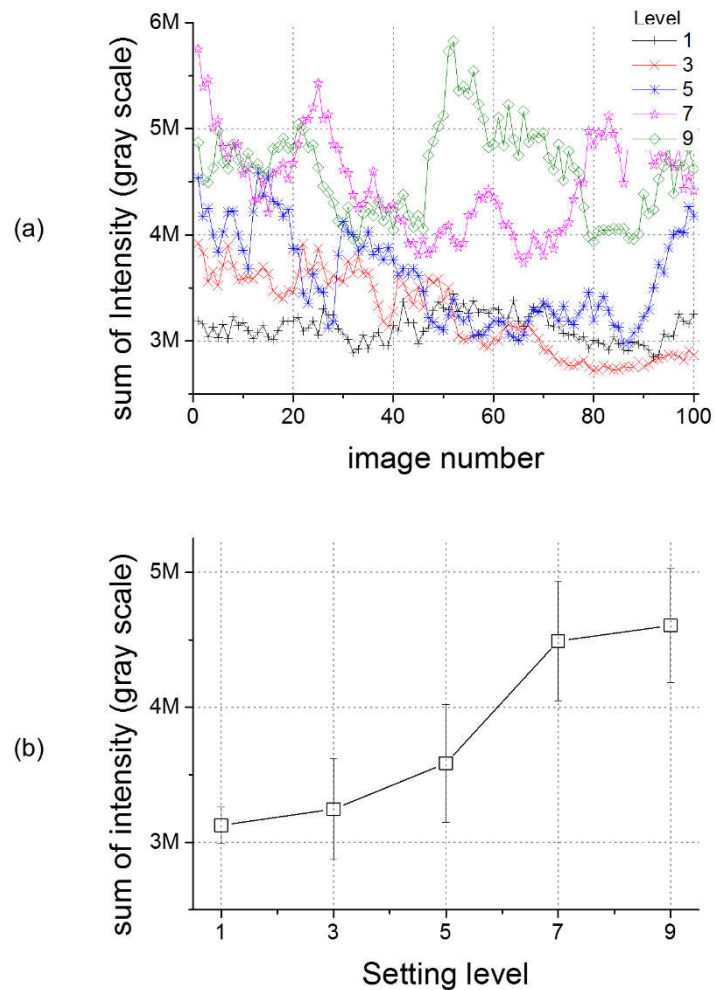
Figure 4.8 Variability of cavitation bubble production with time: (a) sum of the pixel intensity that occupied by bubblers against the sequence number of acquired image, (b) the intensity differences with shock wave output setting levels.

4.3.2 Accumulated Cavitation Bubble Cloud Image

To clarify the geometric feature of the cavitation bubble cloud, multiple images should be required to merge together after removing background structures. As the number of images increases for overlapping, the geometric clarity initially improves, but the effect becomes gradually saturated. Figure 4.9 shows the resulting image into which the 100 instantaneous images were merged to clarify the geometric features of the bubble cloud. The accumulated images demonstrate that the silhouettes of the cavitation bubbles appear like bubble jet streams centered at the focus. The jet streams are stronger as the shock wave generator output setting increases. The boundary of the bubble clouds was reasonably fitted to an elongated ellipsoid centered at the focus, which was similar to the acoustic focal region.

The bubbles were observed to increase in number and size as they approached the focus. In terms of color, the grayscale appeared most intensely at the focal point and faded away from it. This is due to the reflection of background illumination by the bubbles. The silhouette of the bubble cloud appears like a rocket centered at the focus moving in the same direction of the shock wave propagation. The tail of the rocket is made of a number of small bubbles. It was found, on the basis of visual observations, that the 100 images were adequate for optimizing the merging effects.

A practical way of assessing the degree of saturation would be to monitor the rate of increase in the grayscale intensity (Figure 4.10) and area (Figure 4.11) occupied by bubbles as a function of the number of merged images. For the quantitative analysis, grayscale images

were inverted, so that the dense bubble region was given a high grayscale. It is shown that the

rate of increase in the area was significantly reduced (which may suggest saturation in progress)

at the 100 images compared to that at a few numbers of images. As seen in Figure 4.10 and

4.11, the values of each parameter almost linearly increase with the shock wave output setting

levels (adjusted R^2 is 0.99 for the sum of intensity, and 0.98 for the area).

Shock wave direction

Range

#1

#1~#10

#1~#20

#1~#30

#1~#40

⋮

#1~#100

(a)   (b)   (c)   (d)   (e)
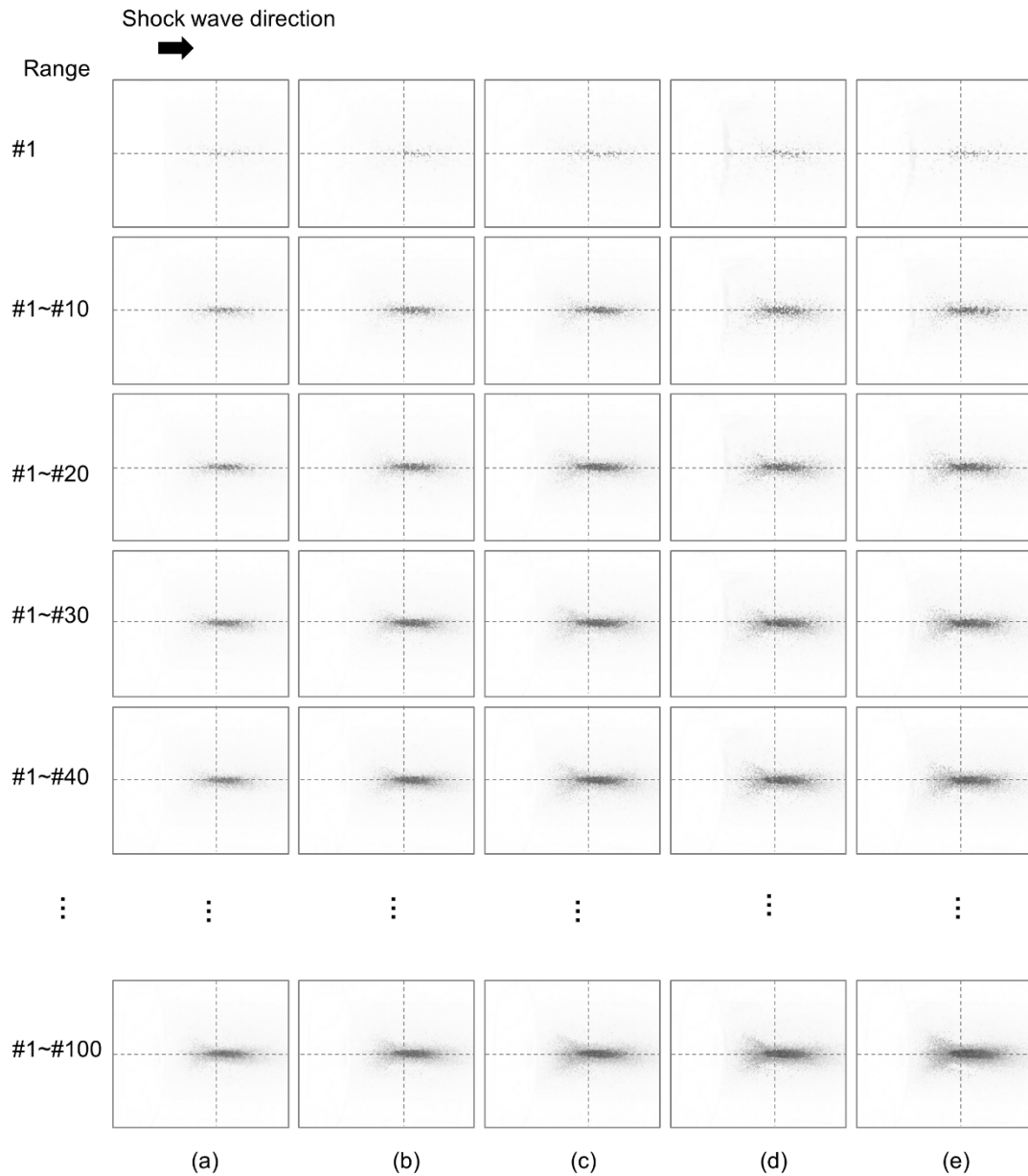
Figure 4.9 Geometrical changes of images accumulated according to the number of instantaneous images. (a) Level 1, (b) Level 3, (c) Level 5, (d) Level 7, (e) Level 9.
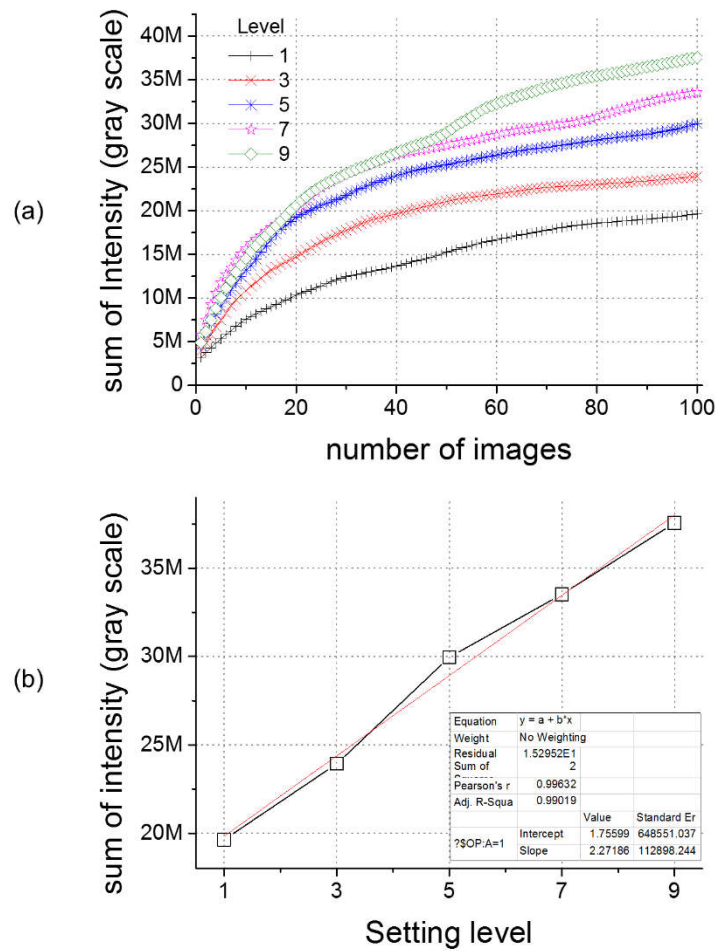
Figure 4.10 (a) Intensity of accumulated cavitation bubble cloud image with the number of images, (b) Correlation between the shock wave output and the sum of intensity.
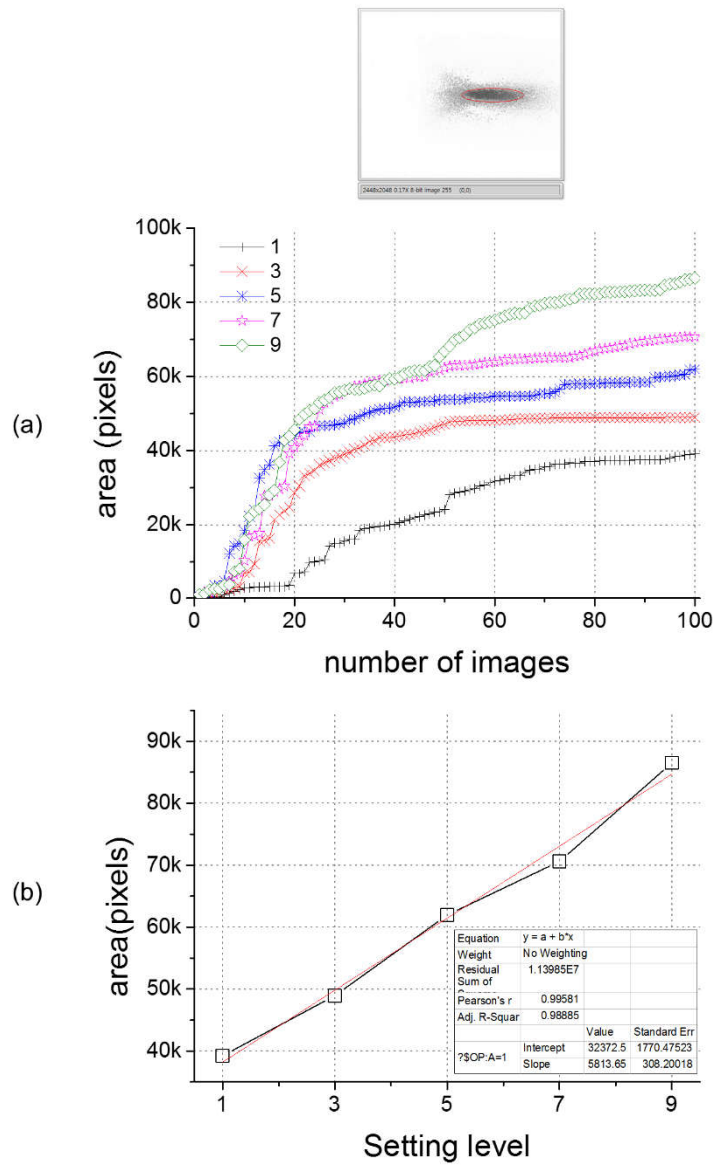
Figure 4.11 (a) Area of accumulated cavitation bubble cloud image with the number of images, (b) Correlation between the shock wave output and area of the cavitation bubble cloud.

4.3.3 Comparison of the Cavitation Image and the Predicted Pressure Field

The predicted focusing process from the simulation and the focal pressure distributions produced by the shock wave generator are displayed in Figure 2.2b of Chapter 2, illustrating the sequential instantaneous image of the initial cylindrically diverging wave, the reflection for focusing, and the beam patterns through focus. The pressure distributions throughout the focus are plotted for the peak positive pressure (Figure 4.12a) and peak negative pressure (Figure 4.12b). It is shown that the peak positive pressure is more tightly focused than the peak negative pressure. Their focal pressure distributions are characteristically different from each other. The (-6dB) focal region is much larger for the peak negative pressure than for the peak positive pressure. The locations of the largest peak pressures are different between the peak positive and negative pressure. The negative peak pressure is focused to the position that deviates from the focus of the positive peak pressure (being close to the geometric focus), about 3 mm towards the shock wave transducer. It will be discussed more in following sections.

As observed in Figures 4.7 and 4.9, the bubbles mostly appeared in the acoustic focal regions, and their density and size were subject to the relative location from the focus. This observation suggests that the cavitation bubbles are closely associated with the spatial distribution of acoustic pressure. This speculation is elucidated by comparing Figure 4.12c with Figure 4.12a and 4.12b. The image of the cavitation bubble cloud looks more similar to the focal pressure distribution of peak negative pressure, rather than the focal peak positive pressure field. In particular, the pre-focal acoustic field structure is well reproduced by a

number of small bubbles observed in the pre-focal region (left side of the image). The static

image of the cavitation bubbles characteristically holds the focal distribution of the peak

negative pressure of the shock wave. This result can possibly be explained by the critical role

of negative pressures to form cavitation bubbles (Pishchalnikov *et al*., 2006).
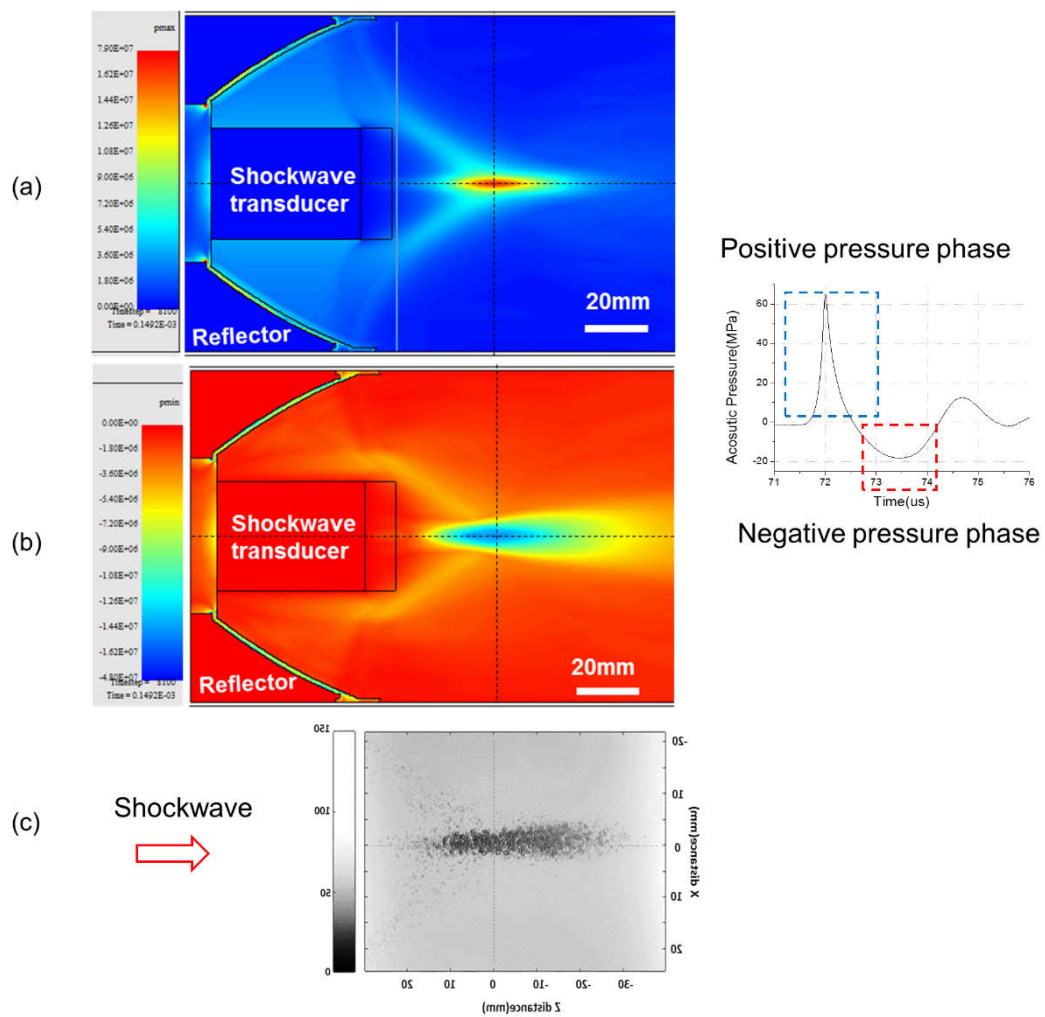
Figure 4.12 Predicted focusing shock wave field. (a) peak positive and (b) peak negative pressure field of the shock wave, (c) accumulated cavitation cloud image.

4.3.4 One dimensional Pressure Profile

One dimensional (1D) pressure profile of the peak positive (Dotted line, p+) and negative pressure (Solid line, p-) are shown in Figure 4.13. Note that the red arrow indicates the direction of shock wave propagation and charging voltage of shock wave generator was 19.75 kV (Level 7). Acoustic pressure rose rapidly near the focal point. The peak positive and negative pressure were measured to be 93 MPa and -19 MPa, respectively. The position of the peak negative pressure appeared before the geometric focal point towards the transducer.

4.3.5 Comparison of the Cavitation Cloud Image and the Acoustic Negative Pressure Field

In terms of optical image, the grayscale intensity of bubbles projected on CCD image sensor depends on bubble lifetime. The lifetime of bubbles is known to be highly correlated with the exposed shock wave pressure (Church, 1989, Bailey *et al*., 2003). Therefore, the grayscale distribution of visualized bubble images is expected to be highly relied on the distribution of the shock wave field.

Figure 4.14a shows the accumulated cavitation cloud image using 100 instantaneous images with a charging voltage of 19.75 kV (Level 7). The vertical and horizontal line-profile responses to the focus position are shown in Figure 4.14b and 4.14c, respectively. Note that

the grayscale values were inverted due to the fact that less light was transmitted through the bubbles. These line-profiles are very noisy because these are the result of superimposing of many images that have sparse bubbles. As expected, it appears strongest in the focal position and is gradually decreasing as it moves further away from the focal position.

It is interesting to compare the line-profiles to the negative pressure profile as shown in Figure 4.15. For comparison of two data with different physical quantities, 1D line profiles of cavitation image and negative pressure were overlaid. Line profiles of cavitation image were smoothed out using a moving average filter (window size of 50 points) to reduce noise (Figure 4.15). Their distance axes were shared, the left vertical axis representing the negative pressure and the right vertical axis representing the grayscale were adjusted to the same peak and base line. The peak position and shape of distribution in the axial and radial directions are similar.

Figure 4.16 shows the linear relationship between the shock wave pressure and the grayscale level of the cavitation bubble image. Gray scale level raised as the negative pressure was increased. This result implies a strong linear correlation between two parameters (adjusted R^2 = 0.865, Pearson's r = 0.93). However, optimization is necessary because there is a possibility that the cavitation phenomenon can change depending on the medium condition and be distorted by the vision system environment.
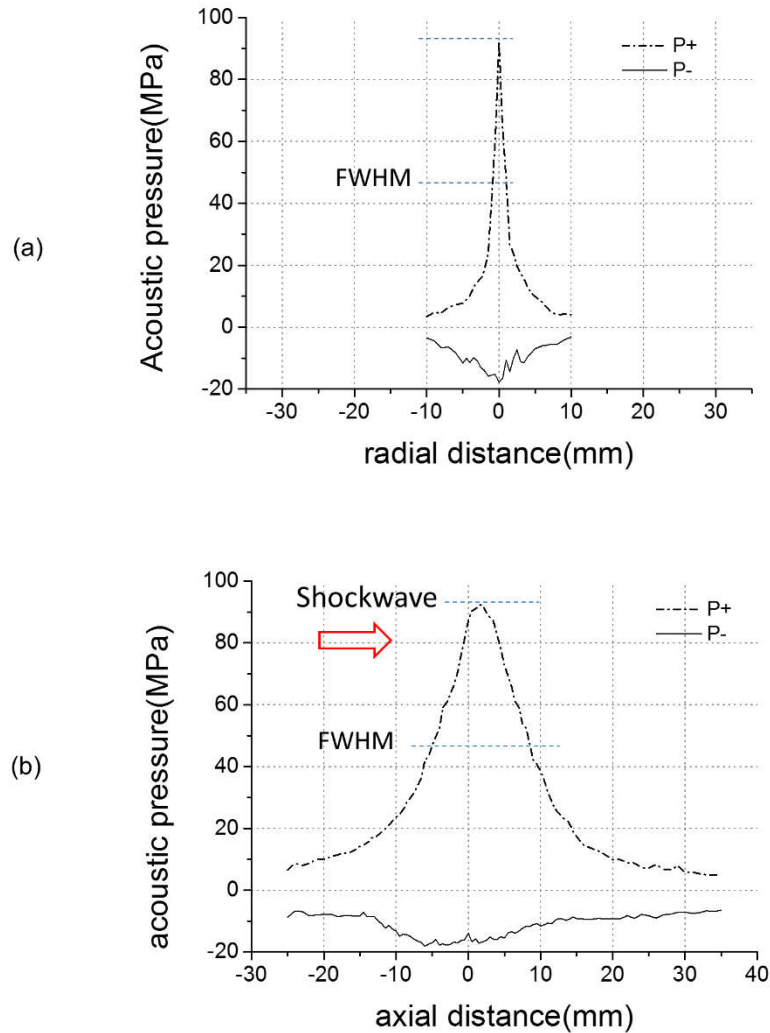
Figure 4.13 One dimension (1D) Pressure distribution from the geometric focus of shock wave transducer along axial and radial direction. The charging voltage is 19.75 kV. Red arrow indicates the direction of shock wave propagation. (a) radial direction, (b) axial direction.
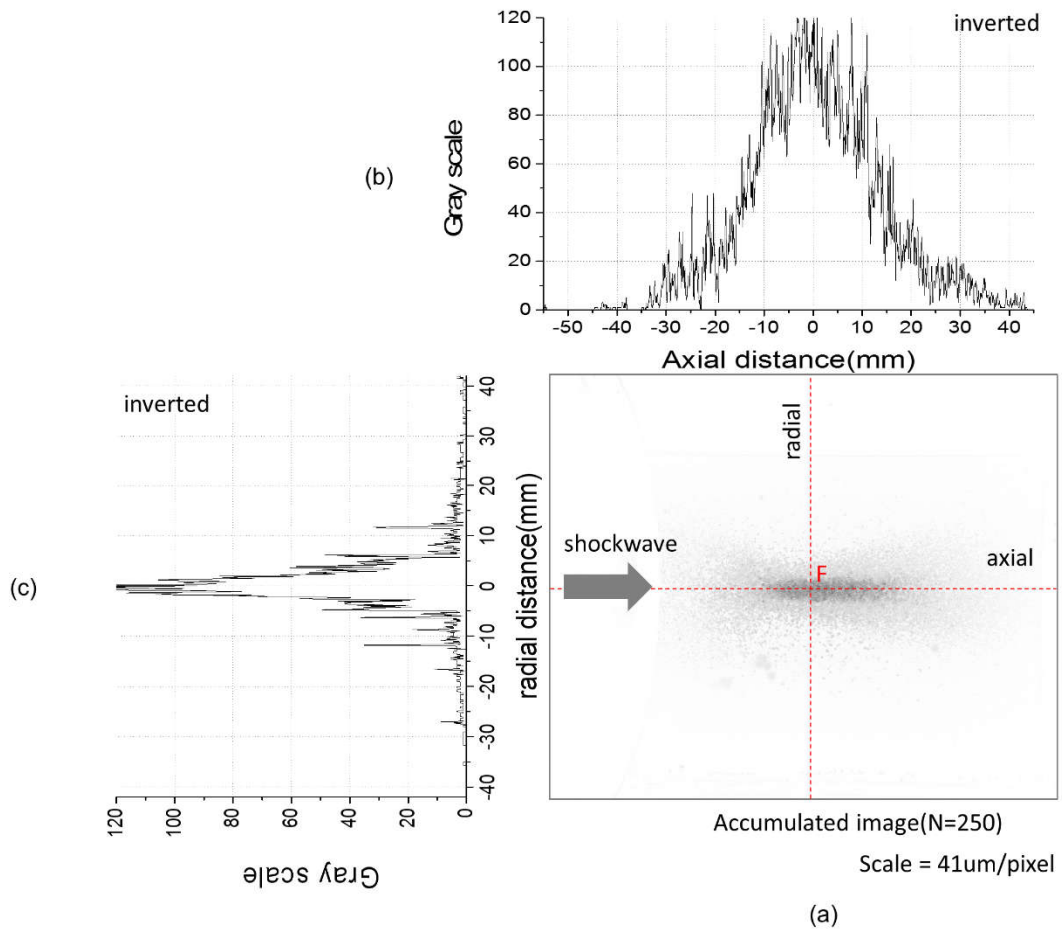
Figure 4.14 Cavitation bubble cloud and its line profile of the accumulated image along the axial and radial axis.
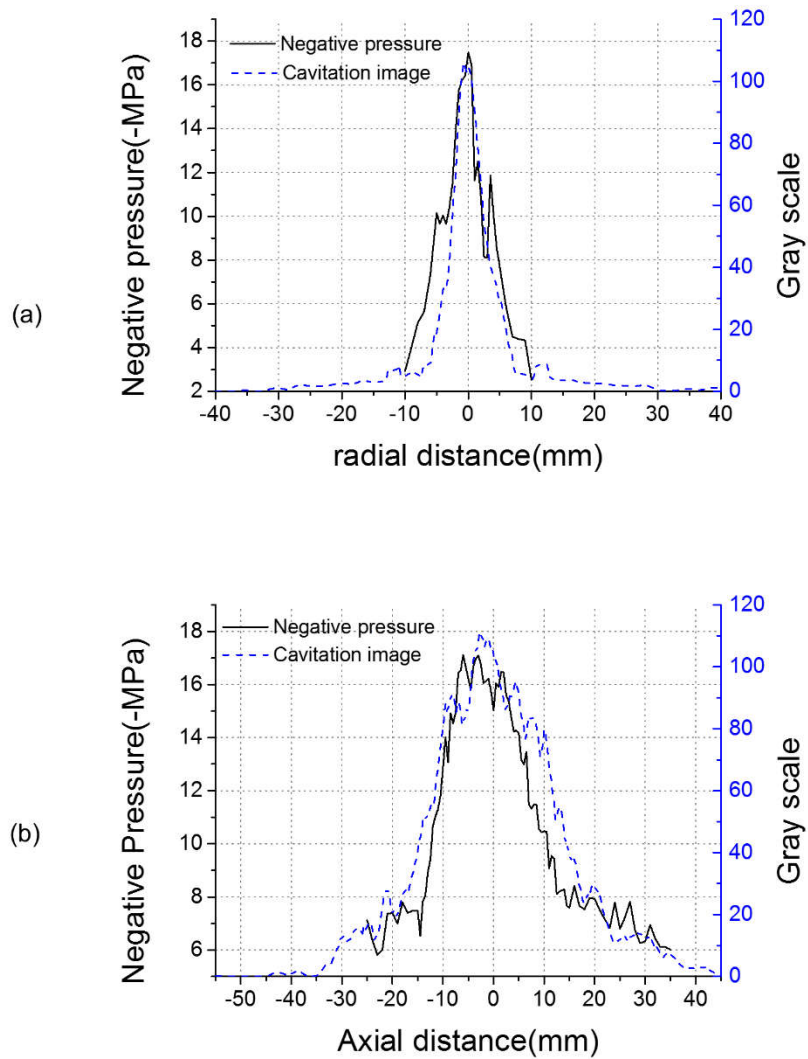
Figure 4.15 Cavitation bubble cloud and its line profile of the accumulated image along the axial and radial axis.
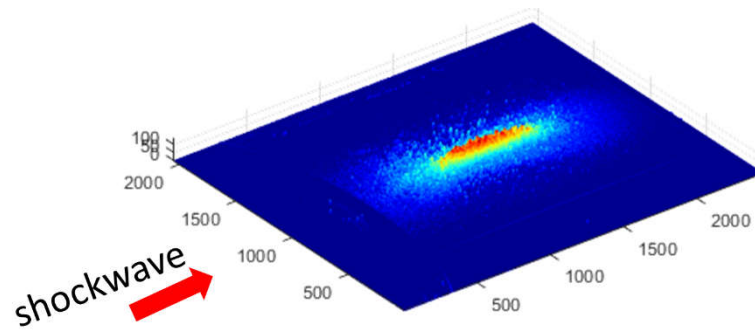
Color plot image
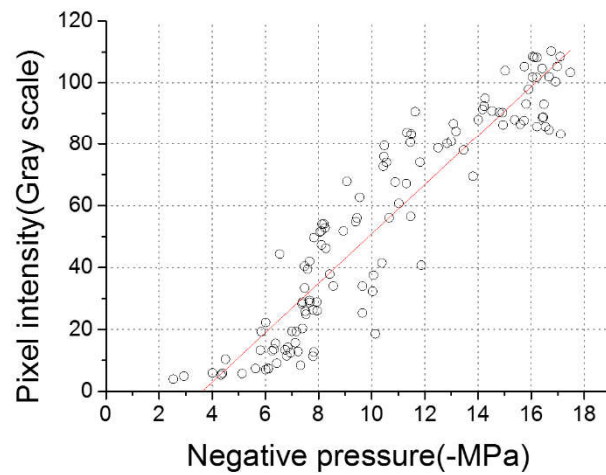
Equation : y=a+bx
a=-28.9
b=7.98

Pearson's r = 0.93
Adjusted R^2 = 0.865

Figure 4.16 Correlation analysis between shock wave pressure and grayscale level of the accumulated cavitation bubble image.

4.3.6 Effect of Light Exposure Time

The cavitation bubble image acquired by the CCD camera senses bubble behavior only during the time that the light system is working. This section focuses on the result of the dynamic characteristics of the bubbles with respect to the light exposure time.

Figure 4.17 shows a time chart of the light exposure. Shockwave was triggered at 0 μs. After the shock wave was triggered and the time delay of 60 μs was elapsed, the light exposure times was set to 10, 50, 100, 150, 200, and 300 μs. Note that the shock wave reached the focal point at 72 μs.

Figure 4.18 depicts the typical acquired instantaneous snapshot images of cavitation bubble cloud taken at a time delay of 60 μs after shock wave generator triggered. Light exposure time was chosen to set to (a) 50, (b) 100, (c) 150, and (d) 200 μs for which the dynamic behavior of cavitation bubble was projected onto a single image. It was observed that the bubbles appeared sparsely and were spherically shaped for the light exposure time from 50 to 150 μs (Figure 4.18a and 4.18c). The number and size of bubbles decreased slightly in Figure 4.18c compared to Figure 4.18b. A dark area appeared at the edges of bubbles and moved toward adjacent bubbles (Figure 4.18c right hand side). The bubbles with relatively long lifetime remained in the focal area and were observed to form jets during their inertial collapses as seen in Figure 4.18d.

A sequential series of the 50 images of the cavitation bubbles were captured under the micro pulsed light with various exposure time (Figure 4.19). When the light exposure time

was 10 μs, i.e. the light was illuminated close to the time (68.5 μs) at which the shock wave

reaches the focus position, the cavitation bubble cloud appeared in a cone shape facing the

focal point (Figure 4.19a). As Lex was set to illuminate bubbles until shock wave propagated

through the focus, the geometrical features of the resulting cavitation bubble clouds were

imaged. It was found that they were observed to be similar to the driving shock wave field, in

particular, the focal distribution of the peak negative pressure (Figure 4.19b and 4.19c). When

Lex was set to be longer than the lifetime of the largest bubble, small bubbles around the focus

area disappeared and only the bubbles in the focal zone remained and gradually blurred (Figure

4.19d and 4.19e).
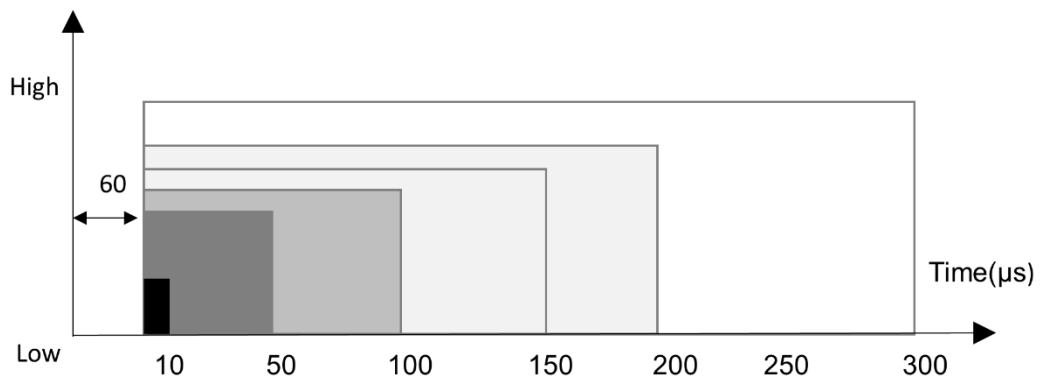
Figure 4.17 TTL signal to synchronize a CCD with MPLL for various exposure time.
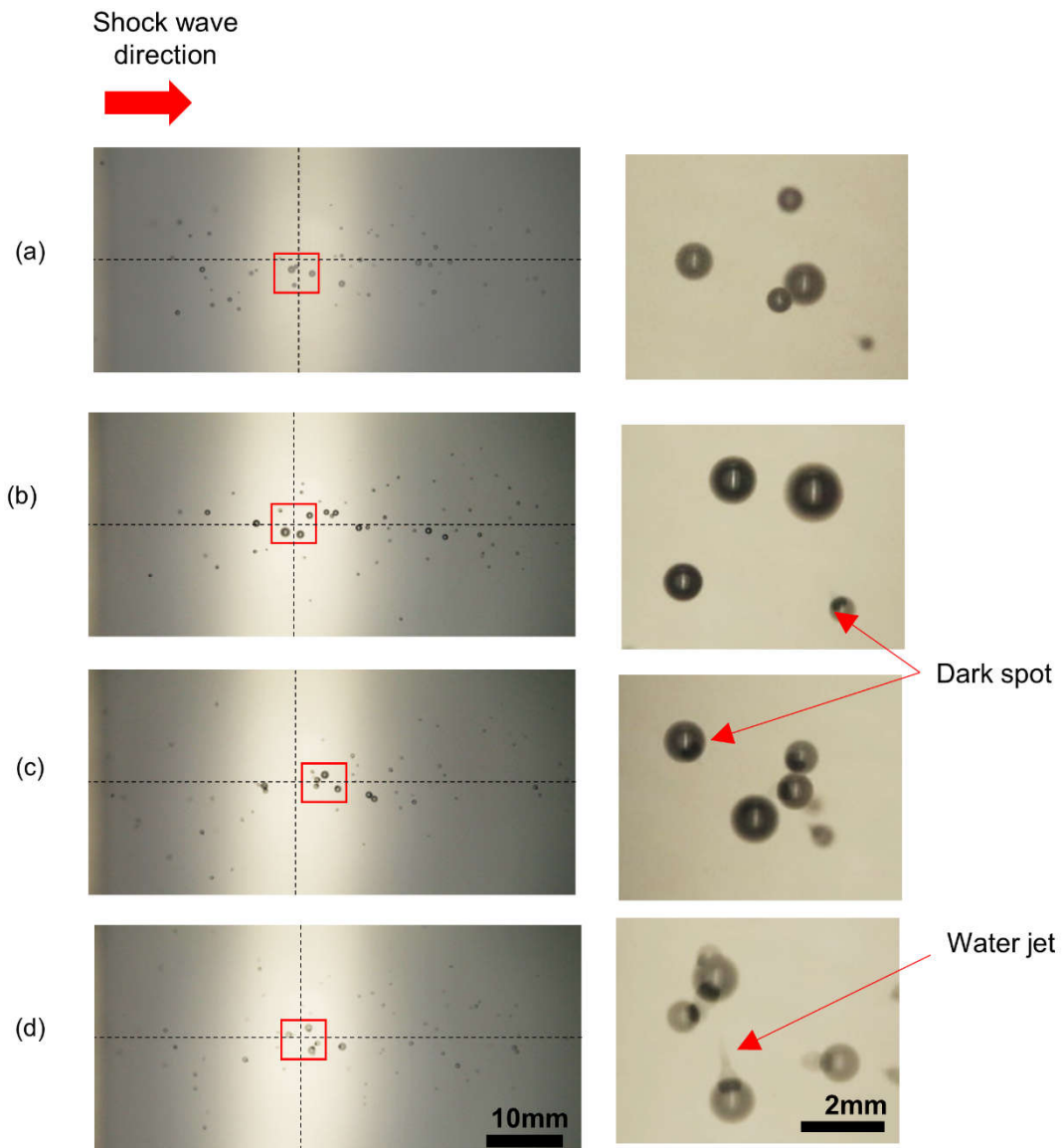
Figure 4.18 Typical instantaneous snapshot images of cavitation bubble cloud taken at a time delay of 60 μs after shock wave generator triggered. (a) 50 μs, (b) 100 μs, (c) 150 μs, (d) 200 μs.
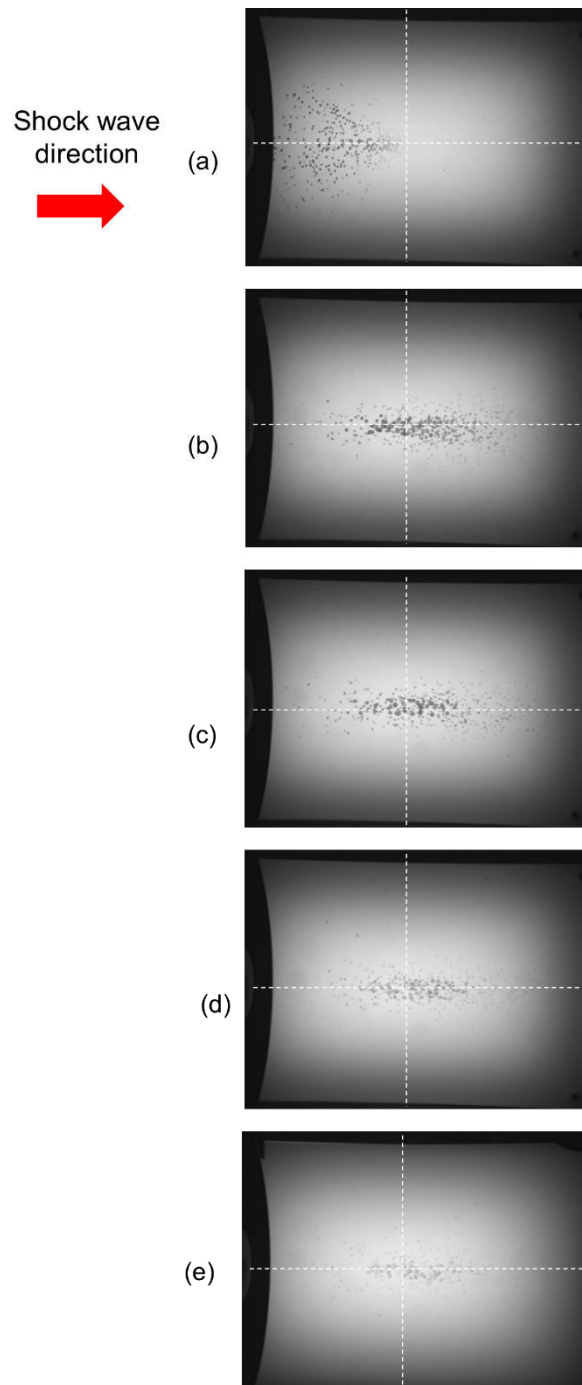
Figure 4.19 A sequential series of the 50 images of the cavitation bubbles captured under the micro pulsed light with various exposure time. (a) 10 μs, (b) 50 μs, (c) 100 μs, (d) 200 μs, and (e) 300 μs.

4.4 Discussion

4.4.1 Bubble Distribution

Figure 4.20 shows a spatial comparison of the 1D pressure profile and the accumulated image with 20 instantaneous images. White and red cross indicate the positions of the peak positive and negative pressure, respectively. Since the shape of the bubble in the image remains as a circular shape, the effect of the its spatial movement seems to be insignificant. The bubbles become relatively denser and larger as they approach the focus. More small bubbles were observed in the pre-focal region (left side of the image). Such features are well preserved on the images when capturing repeatedly.

As seen in Figure 4.3b, large bubbles are darkly imaged because they grow for a relatively long period of time, and small bubbles are blurred because they survive for a relatively short period of time. This may imply a correlation between the grayscale of the image and the lifetime of the bubble. And this also means that cavitation image can be used to evaluate the lifetime of bubbles spatially distributed in the shock wave field.
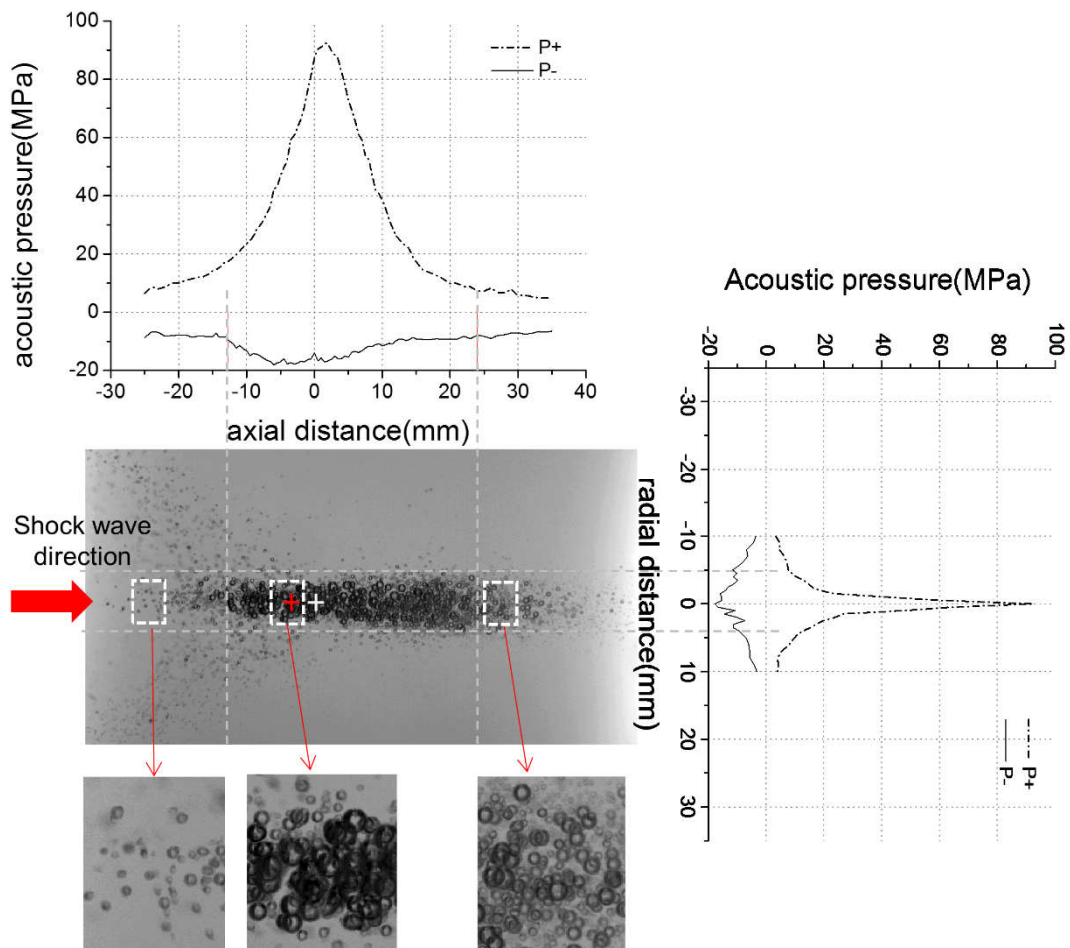
Figure 4.20 Cavitation bubble cloud image in contrast to the 1D pressure profiles of the positive and negative peak pressures of shock waves.

4.4.2 Clinical Meaning of Cavitation Cloud Image

Multiple previous studies demonstrated that shock wave-induced cavitation bubbles are closely related to clinical effect (Coleman *et al*., 1987; Crum, 1988; Delius *et al*., 1988; Loske *et al*., 2002; Pishchalnikov *et al*., 2003; Pishchalnikov *et al*., 2006; Rink *et al*., 1994). This study considered the static afterimages of the cavitation bubbles overlapped over the entire bubble lifetime. The therapeutic effect is more closely associated with bubble dynamics, particularly the violent inertial collapses (Coleman *et al*., 1987; Pishchalnikov *et al*., 2006). An investigation that includes the dynamic activities of cavitation bubbles is required to effectively deliver the therapeutic regions of the shock wave therapy (Pishchalnikov *et al*., 2005). Cavitation cloud image using long exposure photography effectively visualizes the area where bubbles collapse after growing fully. And this area can be regarded as the targeted therapeutic region of the shock wave therapy where the cavitation effect and the inertial collapses of the bubble dynamics are maximized (Figure 4.19e).

4.4.3 Advantages of Use of Long Exposure Shadowgraphy

To observe the dynamic variations of such bubbles, we may need to look into a number of sequential images of the bubbles captured at a very short time interval on the order of nanosecond for the entire bubble lifetime. To obtain such images, we need a high-resolution

high-speed camera, which may not be readily available. The present micro-pulse LED light

can reduce the illumination time to several ten microseconds. Because it acquires a single

image synchronized to a TTL signal, it has an advantage to use a relatively inexpensive

ordinary industrial CCD camera. Nevertheless, the captured afterimages that accumulate in all

the temporal histories of cavitation bubbles are still valuable, because they provide information

on the area and location of significant bubble activities. Such geometrical information is easily

obtainable by the present optical method and is therefore practically useful for predicting the

size and location of the therapeutic region.

4.4.4 Quality Assurance Toolkit for Shock Wave Device

The present practical optical method may have potential for the quality assurance of the

therapeutic devices. The present performance test of the therapeutic device requires the precise

information of the focal intensity and region which are technically difficult for clinical users

to obtain. In order to assure if the device works as it was released from manufacturers, the

relative deviation from the standard working condition needs to be examined. If we regularly

obtain the optical images of the cavitation bubbles which are easily captured by clinical users,

the comparison of them to the standard image obtained under the normal working condition

may enable clinical users to test the performance of the therapeutic device. A future work for

the construction of a simplified tool kit for the quality assurance purpose is suggested for

clinical users to assure the clinical efficacy as well as patient safety.

4.4.5 Limitations

The image of cavitation bubbles is captured rapidly and easily by a simple optical method, while a time-consuming expensive hydrophone damaging scanning process is required to obtain the acoustic focal field. Accordingly, the present optical method is practically useful for delivering the geometrical features of the acoustic focal region, even if a precise shock wave measurement is not possible. The conditions for obtaining the optical image of cavitation bubbles such as the illumination time and the number of images for overlay should be further optimized to estimate the acoustic focal region more accurately.

4.5 Conclusion

The optical images of the shock wave-induced cavitation bubble clouds were successfully captured under the illumination of a micro-second LED light, demonstrating that they hold the geometrical features of the acoustic focal region.

Admitting that cavitation plays an important role in therapeutic effects and the cavitation bubble geometry is closely associated with the true therapeutic region, the optical bubble image has clinical potential to estimate the acoustic field. The observed similarity between

cavitation bubble distribution and pressure field would be a basis that the performance test of the therapeutic device may be carried out with the optical image of cavitation bubbles. And this result suggests that the cavitation bubble image may in part be substituted for a time consuming expensive hydrophone damaging scanning process for accurate shock wave field measurements, particularly the focal distribution of the peak negative pressure.

Cavitation bubbles produced by a single shock wave pulse are highly correlated with the shock wave pressure at an exposed location since there is no significant positional movement during its lifetime. Therefore, the distribution of cavitation is similar to the spatial characteristics of the shock wave negative pressure field. It has a possibility to quantitatively analyze the shock wave pressure field by observing the cavitation bubble cloud which is difficult to measure.

The study is limited to the static images of cavitation bubbles and an investigation that includes bubble dynamics is suggested to examine the cavitation-related therapeutic effects. Further studies are suggested to relate the cavitation bubble images to clinical outcomes.

Chapter 5

CONCLUSIONS AND FUTURE STUDIES

5.1 Conclusions

This research has expanded the application range of optical hydrophone and cavitation cloud imaging. This study describes the feasibility of optical methods that can simultaneously measure acoustic pressure and cavitation in a shock wave field simultaneously.

An optical hydrophone is utilized for reliable measurements in high intensity shock wave field and cavitating liquid. The signal output from optical hydrophone contains artifacts attributable to cavitation bubbles. This cavitation related signal appears as peculiar tails after the main pulse of shock wave. The present study demonstrated that this cavitation related artifacts can be interpreted as a useful information and can be used to measure the 1st and 2nd collapse signals, which are characteristic of shock wave-induced cavitation. In particular, the 2nd collapse of bubbles is considered as a direct treatment mechanism in shock wave therapy. As expected, the life time measured by cavitation related signal was found to be highly correlated with the shock wave output. With these findings, an alternative method that can measure the acoustic pressure of shockwave and its subsequent cavitation related signal, directly and simultaneously, with a single measurement, can be proposed.

A simple optical method was devised to visualize shock wave-induced cavitation bubbles

under micro-pulse LED light illumination. The characteristics of the cavitation bubbles were observed to hold those of the shock wave field, particularly the focal distribution of the peak negative pressure. A high correlation from the result of the comparison between the pixel intensities of the optical image with negative pressure means that the gray scale level can roughly represent the negative pressure level in 2D space. The characteristics of the shock wave acoustic field and collapsing position of large bubbles were confirmed under various lighting operation time. It is known that the position of inertial bubble collapse is highly correlated with the effective area of shock wave treatment. The observed similarity would be a basis that the performance test of the therapeutic device may be carried out with the optical image of cavitation bubbles without a time-consuming expensive hydrophone damaging scanning process for the precise shock wave field measurement.

5.2 Future Works

Cavitation related signal was verified that its fluctuation signals are related to the 1st and 2nd collapse signals of cavitation, which correlate with cavitation energy. Since the optical hydrophone can simultaneously measure the shock wave pressure and cavitation related signals, the cavitation energy field can be mapped on the shock wave pressure field at the same time. Spatial measurement of shock wave field is challenged, which may reveal the characteristics of cavitation bubble cloud in shock wave field and effective area of shock wave

treatment.

This present study is limited to revealing the relationship between the geometry of the cavitation bubble group and the shock wave field. In fact, the bubbles are dynamically activated by shock waves and their temporal behaviors are chaotic throughout from generation to collapse, which is closely associated with the therapeutic effect.

The cavitation phenomenon varies depending on the state of the medium such as temperature, impurities, and type of medium, and so on. In this study, the influence of the medium conditions was not considered.

For shadowgraphy, the pixel intensity of the cavitation bubble image has more physical information than expected. Light ray is refracted by bubbles, and it affects pixel intensity depending on the time of bubble existence. The pixel intensity was found to be related to the negative pressure of shock wave field and the bubble size. Since the size of the bubble is highly correlated with the lifetime of the bubble, a new method can be proposed to measure the lifetime of individual bubbles distributed in space using cavitation bubble cloud images. They are also associated with cavitation dose when the bubble collapses.

The pixel intensity represents the amount of light irradiated on the image sensor and can vary depending on the camera and light settings such as light intensity, duration, sensor gain, iris, and gate, and so on. For a reproducible and reliable cavitation measurement technique, standardization research through optimization of cavitating medium is further needed.

REFERENCES

Albala, D. M., Assimos, D. G., Clayman, R. V., Denstedt, J. D., Grasso, M., Gutierrez-Aceves, J., Kahn R. I., Leveillee, R. J., Lingeman, J. E., Macaluso, Jr., J. N., Munch, L. C., Nakada, S. Y., Newman, R. C., Pearle, M. S., Preminger, G. M., Teichman, J., and Woods, J. R. (2001). Lower pole I: a prospective randomized trial of extracorporeal shock wave lithotripsy and percutaneous nephrostolithotomy for lower pole nephrolithiasis—initial results. *The Journal of Urology*, 166(6), pp2072-2080.

Ando, K., Sanada, T., Inaba, K., Damazo, J. S., Shepherd, J. E., Colonius, T., and Brennen, C. E. (2011). Shock propagation through a bubbly liquid in a deformable tube. *Journal of Fluid Mechanics*, 671, pp339-363.

Apfel, R. E. (1982). Acoustic cavitation: a possible consequence of biomedical uses of ultrasound. *The British journal of cancer. Supplement*, 45, pp140-146.

Arora, M., Junge, L., and Ohl, C. D. (2005). Cavitation cluster dynamics in shock-wave lithotripsy: Part 1. Free field. *Ultrasound in Medicine and Biology*, 31(6), pp827-839.

Arora, M., Ohl, C. D., and Lohse, D. (2007). Effect of nuclei concentration on cavitation cluster dynamics. *The Journal of the Acoustical Society of America*, 121(6), pp3432-3436.

Atchley, A. A., Frizzell, L. A., Apfel, R. E., Holland, C. K., Madanshetty, S., and Roy, R. A. (1988). Thresholds for cavitation produced in water by pulsed ultrasound. *Ultrasonics*, 26(5), pp280-285.

Bailey, M. R., Blackstock, D. T., Cleveland, R. O., and Crum, L. A. (1999). Comparison of electrohydraulic lithotripters with rigid and pressure-release ellipsoidal reflectors. II. Cavitation fields. *The Journal of the Acoustical Society of America*, 106(2), pp1149-1160.

Bailey, M. R., Crum, L. A., Sapozhnikov, O. A., Evan, A. P., Mcateer, J. A., Colonius, T., and Cleveland, R. O. (2003). Cavitation in shock wave lithotripsy. *Journal of the Acoustical Society of America*, 114(4), pp2417-2417.

Bailey, M. R., Pishchalnikov, Y. A., Sapozhnikov, O. A., Cleveland, R. O., McAteer, J. A., Miller, N. A., Pishchalnikova, I. V., Connors, B. A., Crum, L. A., and Evan, A. P.

(2005). Cavitation detection during shock-wave lithotripsy. *Ultrasound in Medicine and Biology*, 31(9), pp1245-1256.

Bekaev, A. A., Sokovikov, V. K., and Strokov, P. I. (2014). Electrohydraulic devices based on the Yutkin effect. *Russian Engineering Research*, 34(10), pp620-623.

Blackstock, D. T. (2000). *Fundamentals of physical acoustics*. John Wiley & Sons Inc. New York, USA.

Borkent, B. M., Gekle, S., Prosperetti, A., and Lohse, D. (2009). Nucleation threshold and deactivation mechanisms of nanoscopic cavitation nuclei. *Physics of Fluids*, 21(10), 102003.

Bourlion, M., Dancer, P., Lacoste, F., Mestas, J. L., and Cathignol, D. (1994). Design and characterization of a shock wave generator using canalized electrical discharge: Application to lithotripsy. *Review of Scientific Instruments*, 65(7), pp2356-2363.

Bull, V., Civale, J., Rivens, I., and ter Haar, G. (2013). A comparison of acoustic cavitation detection thresholds measured with piezo-electric and fiber-optic hydrophone sensors. *Ultrasound in Medicine and Biology*, 39(12), pp2406-2421.

Bull, V., Civale, J., Rivens, I., and ter Haar, G. R. (2011, September). Cavitation Detection Using a Fibre-Optic Hydrophone: A Pilot Study. In *AIP Conference Proceedings*, 1359(1), pp85-90, AIP.

Cai, H. Y., Li, L., Guo, T., Wang, Y. U., Ma, T. K., Xiao, J. M., Zhao, L., Fang, Y. Yang, P., and Zhao, H. U. (2015). Cardiac shockwave therapy improves myocardial function in patients with refractory coronary artery disease by promoting VEGF and IL-8 secretion to mediate the proliferation of endothelial progenitor cells. *Experimental and Therapeutic Medicine*, 10(6), pp2410-2416.

Carnell, M. T., Alcock, R. D., and Emmony, D. C. (1993). Optical imaging of shock waves produced by a high-energy electromagnetic transducer. *Physics in Medicine and Biology*, 38(11), pp1575-1588.

Caupin, F., and Herbert, E. (2006). Cavitation in water: a review. *Comptes Rendus Physique*, *7*(9-10), pp1000-1017.

Chaussy, C., Schmiedt, E., Jocham, B., Brendel, W., Forssmann, B., and Walther, V. (1982). First clinical experience with extracorporeally induced destruction of kidney stones by shock waves. *The Journal of Urology*, 127(3), pp417-420.

Chen, H., Li, X., Wan, M., and Wang, S. (2007). High-speed observation of cavitation bubble cloud structures in the focal region of a 1.2 MHz high-intensity focused ultrasound transducer. *Ultrasonics Sonochemistry*, 14(3), pp291-297.

Chitnis, P. V., and Cleveland, R. O. (2006). Quantitative measurements of acoustic emissions from cavitation at the surface of a stone in response to a lithotripter shock wave. *The Journal of the Acoustical Society of America*, 119(4), pp1929-1932.

Cho, S. C. (2008). Optimization of an electromagnetic cylindrical shock wave transducer used in extracorporeal shock wave therapy. M.Sc. Thesis, Jeju National University, Jeju, Republic of Korea, Chap. 1, pp.4-17.

Cho, S. C., Kang, G. S., Kim, S. H., Lee, K. I., Paeng, D. G., & Choi, M. J. (2007). Properties of the acoustic fields of a domestic electromagnetic extracorporeal shock wave therapy system. *Proceedings of the Acoustical Society of Korea, 26,* pp237-238.

Choi, M. J. (1992). Theoretical aspects of high amplitude pulsed ultrasound used in lithotripsy. PhD Thesis, University of Bath, Bath, United Kingdom, Chap. 6, pp127-175.

Choi, M. J. (2001, March). Precise determination of the cavitation activity caused by a lithotripsy field using a wavelet transformation. Final Program and Abstract. In *The Physics and Technology of Medical Ultrasound Biennial Meeting*, pp26-28.

Choi, M. J., Cho, S. C., Kang, G. S., Paeng, D. G., Lee, K. I., Hodnett, M., Zeqiri, B., and Coleman, A. J. (2008). Quantification of acoustic cavitation produced by a clinical extracorporeal shock wave therapy system using a passive cylindrical detector. *Modern Physics Letters B*, 22(11), pp809-814.

Choi, M. J., Cho, S. C., Kang, G., and Coleman, A. J. (2012). Activities of the cavitation bubbles in the wake of a shock pressure pulse recorded by an optical fiber hydrophone. *The Journal of the Acoustical Society of America*, 131(4), pp3365-3365.

Choi, M. J., Cho, S. C., Paeng, D. G., and Lee, K. I. (2010). Extracorporeal shock wave therapy: its acoustical aspects. *The Journal of the Acoustical Society of Korea*, 29(3E), pp119-130.

Choi, M. J., Cho, S. C., Paeng, D. G., Lee, K. I., and Coleman, A. (2011). Thickness effects of the metallic and the insulating membranes of a cylindrical electromagnetic shock wave transducer. *Journal of the Korean Physical Society*, 59(61), pp3583-3587.

Choi, M. J., Cho, S. C., Paeng, D. G., Lee, K. I., and Coleman, A. J. (2007). Acoustic characterization of a domestic commercial shock wave therapy system for the treatment of chronic tendonitis using a broadbnand optical hydrophone. The 7th International Symposium of Therapeutic Ultrasound (ISTU7), abstract book, Sheraton Grande Walkerhill, Seoul, 12-15 June, p77.

Choi, M. J., Coleman, A. J., and Saunders, J. E. (1993). The influence of fluid properties and pulse amplitude on bubble dynamics in the field of a shock wave lithotripter. *Physics in Medicine and Biology*, 38(11), pp1561-1573.

Choi, M. J., Doh, D. H., Hwang, T. G., Cho, C. H., Paeng, D. G., Rim, G. H., and Coleman, A. J. (2006). Acoustic streaming in lithotripsy fields: preliminary observation using a particle image velocimetry method. *Ultrasonics*, 44(2), pp133-145.

Church, C. C. (1989). A theoretical study of cavitation generated by an extracorporeal shock wave lithotripter. *The Journal of the Acoustical Society of America*, 86(1), pp215-227.

Cleveland, R. O., Sapozhnikov, O. A., Bailey, M. R., and Crum, L. A. (2000). A dual passive cavitation detector for localized detection of lithotripsy-induced cavitation in vitro. *The Journal of the Acoustical Society of America*, 107(3), pp1745-1758.

Cole, R. H., and Weller, R. (1948). Underwater explosions. Physics Today, 1, 35, Princeton University Press.

Coleman, A. J., and Saunders, J. E. (1989). A survey of the acoustic output of commercial extracorporeal shock wave lithotripters. *Ultrasound in Medicine and Biology*, 15(3), pp213-227.

Coleman, A. J., Choi, M. J., and Saunders, J. E. (1991). Theoretical predictions of the acoustic pressure generated by a shock wave lithotripter. *Ultrasound in Medicine and Biology*, 17(3), pp245-255.

Coleman, A. J., Choi, M. J., and Saunders, J. E. (1996). Detection of acoustic emission from cavitation in tissue during clinical extracorporeal lithotripsy. *Ultrasound in medicine and biology*, 22(8), pp1079-1087.

Coleman, A. J., Choi, M. J., Saunders, J. E., and Leighton, T. G. (1992). Acoustic emission and sonoluminescence due to cavitation at the beam focus of an electrohydraulic shock wave lithotripter. *Ultrasound in medicine and biology*, 18(3), pp267-281.

Coleman, A. J., Saunders, J. E., and Choi, M. J. (1989). An experimental shock wave generator for lithotripsy studies. *Physics in Medicine and Biology*, 34(11), pp1733-1742.

Coleman, A. J., Saunders, J. E., Crum, L. A., and Dyson, M. (1987). Acoustic cavitation generated by an extracorporeal shockwave lithotripter. *Ultrasound in Medicine and Biology*, 13(2), pp69-76.

Coleman, A. J., Whitlock, M., Leighton, T., and Saunders, J. E. (1993). The spatial distribution of cavitation induced acoustic emission, sonoluminescence and cell lysis in the field of a shock wave lithotripter. *Physics in Medicine and Biology*, 38(11), pp1545-1560.

Coralic, V., and Colonius, T. (2013). Shock-induced collapse of a bubble inside a deformable vessel. *European Journal of Mechanics-B/Fluids*, 40, pp64-74.

Cosentino, R., De Stefano, R., Selvi, E., Frati, E., Manca, S., Frediani, B., and Marcolongo, R. (2003). Extracorporeal shock wave therapy for chronic calcific tendinitis of the shoulder: single blind study. *Annals of the Rheumatic Diseases*, 62(3), pp248-250.

Crawford, F., and Snaith, M. (1996). How effective is therapeutic ultrasound in the treatment of heel pain? *Annals of the rheumatic diseases*, 55(4), pp265-267.

Crum, L. A. (1988). Cavitation microjets as a contributory mechanism for renal calculi disintegration in ESWL. *The Journal of Urology*, 140(6), pp1587-1590.

Cunningham, K. B., Coleman, A., Leighton, T. G., & White, P. R. (2001). Characterising in vivo acoustic cavitation during lithotripsy with time-frequency methods. *Acoustics Bulletin*, 26(5), pp10-16.

Cwik, A., Richter, T., and Ermert, H. (1993). An experimental study of cavitation effects due to shock waves. Institute of Electrical and Electronics Engineers Inc, In *Ultrasonics Symposium*, 2, pp785-785.

Davison, L., and Graham, R. A. (1979). Shock compression of solids. *Physics Reports*, 55(4), pp255-379.

Debus, J., Lorenz, W. J., and Huber, P. (1996). A new method of quantitative cavitation assessment in the field of a lithotripter. *Ultrasound in Medicine and Biology*, 22(3), pp329-338.

Debye, P., and Sears, F. W. (1932). On the scattering of light by supersonic waves. *Proceedings of the National Academy of Sciences*, 18(6), pp409-414.

Delacretaz, G., Rink, K., Pittomvils, G., Lafaut, J. P., Vandeursen, H., and Boving, R. (1995). Importance of the implosion of ESWL-induced cavitation bubbles. *Ultrasound in Medicine and Biology*, 21(1), pp97-103.

Delius, M., Jordan, M., Eizenhoefer, H., Marlinghaus, E., Heine, G., Liebich, H. G., and Brendel, W. (1988). Biological effects of shock waves: kidney haemorrhage by shock waves in dogs—administration rate dependence. *Ultrasound in Medicine and Biology*, 14(8), pp689-694.

Delius, M., Jordan, M., Liebich, H. G., and Brendel, W. (1990). Biological effects of shock waves: Effect of shock waves on the liver and gallbladder wall of dogs— Administration rate dependence. *Ultrasound in Medicine and Biology*, 16(5), pp459-466.

Eberle, G., and Eisenmenger, W. (1992). Thermal depolarization of PVDF: anomaly at 180 degrees C. *IEEE Transactions on Electrical Insulation*, 27(4), pp768-772.

Eisenmenger, W. (2001). The mechanisms of stone fragmentation in ESWL. *Ultrasound in Medicine and Biology*, 27(5), pp683-693.

Forssmann, B., Hepp, W., Chaussy, C., Eisenberger, F., and Wanner, K. (1977). Eine Methode zur berührungsfreien Zertrümmerung von Nierensteinen durch Stoßwellen-A method for no-contact destruction of kidney Stones by means of shock waves. *Biomedizinische Technik/Biomedical Engineering*, 22(7-8), pp164-168.

Ghorbani, M., Oral, O., Ekici, S., Gozuacik, D., and Koşar, A. (2016). Review on lithotripsy and cavitation in urinary stone therapy. *IEEE Reviews in Biomedical Engineering*, 9, pp264-283.

Granz, B. (1989). PVDF hydrophone for the measurement of shock waves (lithotripsy). *IEEE Transactions on Electrical Insulation*, 24(3), pp499-502.

Hamilton, M. F., and Blackstock, D. T. (Eds.). (1998). *Nonlinear Acoustics* (Vol. 1). San Diego: Academic press.

Hanafy, A., and Zanelli, C. I. (1991). Quantitative real-time pulsed Schlieren imaging of ultrasonic waves. In *Ultrasonics Symposium, 1991. Proceedings., IEEE 1991,* pp 1223-1227.

Harris, G. R. (1988). Hydrophone measurements in diagnostic ultrasound fields. *IEEE Transactions on Ultrasonics, Ferroelectrics, and Frequency Control*, 35(2), pp87-101.

Hatanaka, K., Ito, K., Shindo, T., Kagaya, Y., Ogata, T., Eguchi, K., Kurosawa, R., and Shimokawa, H. (2016). Molecular mechanisms of the angiogenic effects of low-energy shock wave therapy: roles of mechanotransduction. *American Journal of Physiology-Cell Physiology*, 311(3), ppC378-C385.

Haworth, K. J., Mast, T. D., Radhakrishnan, K., Burgess, M. T., Kopechek, J. A., Huang, S. L., McPherson, D. D., and Holland, C. K. (2012). Passive imaging with pulsed ultrasound insonations. *The Journal of the Acoustical Society of America*, 132(1), pp544-553.

Herbert, E., and Caupin, F. (2005). The limit of metastability of water under tension: theories and experiments. *Journal of Physics: Condensed Matter*, 17(45), ppS3597-S3602.

Herbert, E., Balibar, S., and Caupin, F. (2006). Cavitation pressure in water. *Physical Review E*, 74(4), 041603.

Huang, C., Holfeld, J., Schaden, W., Orgill, D., and Ogawa, R. (2013). Mechanotherapy: revisiting physical therapy and recruiting mechanobiology for a new era in medicine. *Trends in Molecular Medicine*, 19(9), pp555-564.

Huber, P., Debus, J., Peschke, P., Hahn, E. W., & Lorenz, W. J. (1994). In vivo detection of ultrasonically induced cavitation by a fiber-optic technique. *Ultrasound in Medicine and Biology*, 20(8), pp811-825.

IEC60601-2036, I. E. C. (2014). Medical electrical equipment – Part 2 -36: Particular requirements for the basic safety and essential performance of equipment for extracorporeally induced lithotripsy. *International Electrotechnical Commission, Geneva, Switzerland*.

IEC61846, I. E. C. (1998). 61846 Ultrasonics-Pressure pulse lithotriptors-Characteristics of fields. *International Electrotechnical Commission, Geneva, Switzerland*.

Iijima, Y., and Kudo, N. (2017). Evaluation of frequency-dependent ultrasound attenuation in transparent medium using focused shadowgraph technique. *Japanese Journal of Applied Physics*, 56(7S1), 07JF13.

Iloreta, J. I., Zhou, Y., Sankin, G. N., Zhong, P., and Szeri, A. J. (2007). Assessment of shock wave lithotripters via cavitation potential. *Physics of Fluids*, 19(8), 086103.

Ito, K., Fukumoto, Y., and Shimokawa, H. (2009). Extracorporeal shock wave therapy as a new and non-invasive angiogenic strategy. *The Tohoku Journal of Experimental Medicine*, 219(1), 1-9.

Jiang, X., Cheng, Q., Xu, Z., Qian, M., and Han, Q. (2016). Quantitative measurement of acoustic pressure in the focal zone of acoustic lens-line focusing using the Schlieren method. *Applied Optics*, 55(10), pp2478-2483.

Jochle, K., Debus, J., Lorenz, W. J., and Huber, P. (1996). A new method of quantitative cavitation assessment in the field of a lithotripter. *Ultrasound in Medicine and Biology*, 22(3), pp329-338.

Johnk, C. T. A. (1988). Engineering electromagnetic fields and waves. *New York, 2nd ed., John Wiley and Sons, Inc.,* pp277-280.

Jones, W. H. S. Hippocrates. With an English translation by WHS Jones (vol. 1, 2; vol. 3 by ET Withington; vol. 4 [including the text and translation of Heracleitus on the Universe] by WHS Jones). 4 vol.

Kang, G., Cho, C. S., Coleman, A. J., and Choi, M. J. (2014). Characterization of the shock pulse-induced cavitation bubble activities recorded by an optical fiber hydrophone. *The Journal of the Acoustical Society of America*, 135(3), pp1139-1148.

Kearney, C. J., Hsu, H. P., and Spector, M. (2012). The use of extracorporeal shock wave-stimulated periosteal cells for orthotopic bone generation. *Tissue Engineering Part A*, 18(13-14), pp1500-1508.

Kinsler, Lawrence E., Frey, Austin R., Coppens, A. B., and Sanders, James V. (2000). *Fundamentals of Acoustics*. J. Wiley and Sons.

Kodama, T., and Takayama, K. (1998). Dynamic behavior of bubbles during extracorporeal shock-wave lithotripsy. *Ultrasound in Medicine and Biology*, 24(5), pp723-738.

Kodama, T., Hamblin, M. R., and Doukas, A. G. (2000). Cytoplasmic molecular delivery with shock waves: importance of impulse. *Biophysical Journal*, 79(4), pp1821-1832.

Krimmel, J., Colonius, T., and Tanguay, M. (2010). Simulation of the effects of cavitation and anatomy in the shock path of model lithotripters. *Urological research*, 38(6), 505-518.

Uchida, T., Takeuchi, S., and Kikuchi, T. (2010). Study of measurement of the amount of generated acoustic cavitation: Relationships among broadband integrated voltage,

dissolved oxygen, and sonochemical luminescence. In *Ultrasonics Symposium (IUS), 2010 IEEE,* pp2223-2226, IEEE.

Kudo, N. (2015). A simple technique for visualizing ultrasound fields without Schlieren optics. *Ultrasound in Medicine and Biology*, 41(7), pp2071-2081.

Kudo, N. (2015). Optical methods for visualization of ultrasound fields. *Japanese Journal of Applied Physics*, 54(7S1), 07HA01.

Lance, R. M., Capehart, B., Kadro, O., and Bass, C. R. (2015). Human injury criteria for underwater blasts. *PloS one*, 10(11), e0143485.

Lauterborn, W., & Timm, R. (1980). Bubble collapse studies at a million frames per second. In *Cavitation and inhomogeneities in underwater acoustics*, pp42-46, Springer, Berlin, Heidelberg.

Lee, S. H., Lee, J. H., Lee, H. J., and Choi, M. J. (2001). Electromagnetic and dynamic properties of an electromagnetic type shock wave source: numerical simulation. *In Conference Proceedings, the Acoustical Society of Korea,* 20(1S), pp917-920.

Leighton, T. G., Fedele, F., Coleman, A. J., McCarthy, C., Ryves, S., Hurrell, A. M., De Stefano, A., and White, P. R. (2008). A passive acoustic device for real-time monitoring of the efficacy of shockwave lithotripsy treatment. *Ultrasound in Medicine and Biology*, 34(10), pp1651-1665.

Leitao, V. A., Simmons, W. N., Zhou, Y., Qin, J., Sankin, G., Cocks, F. H., Fehre, J., Granz, B., Nanke, R., Preminger, G. M., and Zhong, P. (2007). Comparison of light spot hydrophone (LSHD) and fiber optic probe hydrophone (FOPH) for lithotripter field characterization. *In AIP Conference Proceedings*, 900(1), pp377-380, AIP.

Lingeman, J. E. (1997). Extracorporeal shock wave lithotripsy: Development, instrumentation, and current status. *Urologic Clinics*, 24(1), pp185-211.

Loew, M., and Jurgowski, W. (1993). Extracorporeal shock-waves (ESWL) for treatment of calcareous tendinitis of the shoulder – a preliminary report: *Zeitschrift fur orthopadie und ihre grenzgebiete*, 131(5), pp470-473.

Lokhandwalla, M., and Sturtevant, B. (2000). Fracture mechanics model of stone comminution in ESWL and implications for tissue damage. *Physics in Medicine and Biology*, 45(7), pp1923-1940.

Loske, A. M. (2016). *Medical and biomedical applications of shock waves*. Chapter 2, Cham, Switzerland: Springer.

Loske, A. M., Prieto, F. E., Fernández, F., and van Cauwelaert, J. (2002). Tandem shock wave cavitation enhancement for extracorporeal lithotripsy. *Physics in Medicine and Biology*, 47(22), pp3945-3957.

Madanshetty, S. I., Roy, R. A., and Apfel, R. E. (1991). Acoustic microcavitation: Its active and passive acoustic detection. *The Journal of the Acoustical Society of America*, 90(3), pp1515-1526.

Maeda, K., Kreider, W., Maxwell, A., Cunitz, B., Colonius, T., and Bailey, M. (2015). Modeling and experimental analysis of acoustic cavitation bubbles for Burst Wave Lithotripsy. *In Journal of Physics: Conference Series*, 656(1), 012027. IOP Publishing.

Maxwell, A. D., Cunitz, B. W., Kreider, W., Sapozhnikov, O. A., Hsi, R. S., Harper, J. D., Bailey M. R., and Sorensen, M. D. (2015). Fragmentation of urinary calculi in vitro by burst wave lithotripsy. *The Journal of Urology*, 193(1), pp338-344.

Menzl, G., Gonzalez, M. A., Geiger, P., Caupin, F., Abascal, J. L., Valeriani, C., and Dellago, C. (2016). Molecular mechanism for cavitation in water under tension. *Proceedings of the National Academy of Sciences*, 113(48), pp13582-13587.

Neppiras, E. A. (1980). Acoustic cavitation, Physics Reports, *Review Section of Physics Letters*, 61(3), pp159-251.

Neppiras, E. A. (1980). Acoustic cavitation. *Physics Reports*, 61(3), pp159-251.

Neppiras, E. A. (1984). Acoustic cavitation series: part one: Acoustic cavitation: an introduction. *Ultrasonics*, 22(1), pp25-28.

Nishida, T., Shimokawa, H., Oi, K., Tatewaki, H., Uwatoku, T., Abe, K., Matsumoto Y., Kajihara, N., Eto, M., Matsuda, T., Yasui, H., Takeshita, A., and Sunagawa, K. (2004). Extracorporeal cardiac shock wave therapy markedly ameliorates ischemia-induced myocardial dysfunction in pigs in vivo. *Circulation*, 110(19), pp3055-3061.

Ohl, C. D. (2002). Cavitation inception following shock wave passage. *Physics of Fluids*, 14(10), pp3512-3521.

Ohl, S. W., Klaseboer, E., and Khoo, B. C. (2015). Bubbles with shock waves and ultrasound: a review. *Interface Focus*, 5(5), 20150019.

Pan, P. J., Chou, C. L., Chiou, H. J., Ma, H. L., Lee, H. C., and Chan, R. C. (2003). Extracorporeal shock wave therapy for chronic calcific tendinitis of the shoulders: a functional and sonographic study. *Archives of Physical Medicine and Rehabilitation*, 84(7), pp988-993.

Parsons, J. E., Cain, C. A., and Fowlkes, J. B. (2006). Cost-effective assembly of a basic fiber-optic hydrophone for measurement of high-amplitude therapeutic ultrasound fields. *The Journal of the Acoustical Society of America*, 119(3), pp1432-1440.

Pearle, M. S. (2012). Shock-wave lithotripsy for renal calculi. *New England Journal of Medicine*, 367(1), pp50-57.

Pearle, M. S., Lingeman, J. E., Leveillee, R., Kuo, R., Preminger, G. M., Nadler, R. B., Macaluso, J., Monga, M., Kumar, U., Dushinski, J., Albala, D. M., Wolf, Jr., J. S., Assimos, D., Fabrizio, M., Mynch, L. C., Nakada, S. Y., Auge, B., Honey, J., Oganm, JK., Pattaras, J., McDougall, E. M., Averch, T. D., Turk, T., Pietrow, P., and Watkins, S. (2005). Prospective, randomized trial comparing shock wave lithotripsy and ureteroscopy for lower pole caliceal calculi 1 cm or less. *The Journal of Urology*, 173(6), pp2005-2009.

Pishchalnikov, Y. A., Gutierrez, J., Dunbar, W. W., and Philpott, R. W. (2016). Intense cavitation at extreme static pressure. *Ultrasonics*, 65, pp380-389.

Pishchalnikov, Y. A., McAteer, J. A., Williams Jr, J. C., Pishchalnikova, I. V., and Vonderhaar, R. J. (2006). Why stones break better at slow shockwave rates than at fast rates: in vitro study with a research electrohydraulic lithotripter. *Journal of Endourology*, 20(8), pp537-541.

Pishchalnikov, Y. A., Sapozhnikov, O. A., Bailey, M. R., Pishchalnikova, I. V., Williams Jr, J. C., and McAteer, J. A. (2005). Cavitation selectively reduces the negative-pressure phase of lithotripter shock pulses. *Acoustics Research Letters Online*, 6(4), pp280-286.

Pishchalnikov, Y. A., Sapozhnikov, O. A., Bailey, M. R., Williams Jr, J. C., Cleveland, R. O., Colonius, T., Crum, L. A., Evan, A. P., and McAteer, J. A. (2003). Cavitation bubble cluster activity in the breakage of kidney stones by lithotripter shockwaves. *Journal of Endourology*, 17(7), pp435-446.

Pishchalnikov, Y. A., Williams Jr, J. C., and McAteer, J. A. (2011). Bubble proliferation in the cavitation field of a shock wave lithotripter. *The Journal of the Acoustical Society of America*, 130(2), ppEL87-EL93.

Platte, M. (1985). A polyvinylidene fluoride needle hydrophone for ultrasonic applications. *Ultrasonics*, 23(3), pp113-118.

Raabe, O., Shell, K., Goessl, A., Crispens, C., Delhasse, Y., Eva, A., Scheiner-Bobis, G., Wenisch, S and Arnhold, S. (2013). Effect of extracorporeal shock wave on proliferation and differentiation of equine adipose tissue-derived mesenchymal stem cells in vitro. *American Journal of Stem Cells*, 2(1), pp62-73.

Rabkin, B. A., Zderic, V., and Vaezy, S. (2005). Hyperecho in ultrasound images of HIFU therapy: involvement of cavitation. *Ultrasound in Medicine and Biology*, 31(7), pp947-956.

Rassweiler, J. J., Knoll, T., Köhrmann, K. U., McAteer, J. A., Lingeman, J. E., Cleveland, R. O., Bailey, M. R., and Chaussy, C. (2011). Shock wave technology and application: an update. *European Urology*, 59(5), pp784-796.

Rassweiler, J. J., Tailly, G. G., and Chaussy, C. (2005). Progress in lithotriptor technology. *EAU Update Series*, *3*(1), pp17-36.

Rink, K., Delacretaz, G., Pittomvils, G., Boving, R., and Lafaut, J. P. (1994). Incidence of cavitation in the fragmentation process of extracorporeal shock wave lithotriptors. *Applied Physics Letters*, 64(19), pp2596-2598.

Robinson, P. B., Blake, J. R., Kodama, T., Shima, A., and Tomita, Y. (2001). Interaction of cavitation bubbles with a free surface. *Journal of Applied Physics*, 89(12), pp8225-8237.

Roessler, W., Wieland, W. F., Steinbach, P., Hofstaedter, F., Thuroff, S., and Chaussy, C. (1996). Side effects of high-energy shockwaves in the human kidney: first experience with model comparing two shockwave sources. *Journal of Endourology*, 10(6), pp507-511.

Rompe, J. D., and Maffulli, N. (2007). Repetitive shock wave therapy for lateral elbow tendinopathy (tennis elbow): a systematic and qualitative analysis. *British Medical Bulletin*, 83(1), pp355-378.

Roy, R. A., Madanshetty, S. I., and Apfel, R. E. (1990). An acoustic backscattering technique for the detection of transient cavitation produced by microsecond pulses of ultrasound. *The Journal of the Acoustical Society of America*, 87(6), pp2451-2458.

Sankin, G. N., Lautz, J. M., Simmons, W. N., Zhong, P., Frank, S. T., and Szeri, A. J. (2017, March). Elimination of cavitation-related attenuation in shock wave lithotripsy. *In AIP Conference Proceedings*, 1821(1), 100001, AIP Publishing.

Sansone, V., Bonora, C., Sizzano, F., De, L. G., and Romeo, P. (2012). Early angiogenic response to shock waves in a three-dimensional model of human microvascular endothelial cell culture (HMEC-1). *Journal of Biological Regulators and Homeostatic Agents*, 26(1), pp29-37.

Sapozhnikov, O. A., Khokhlova, V. A., Bailey, M. R., Williams Jr, J. C., McAteer, J. A., Cleveland, R. O., and Crum, L. A. (2002). Effect of overpressure and pulse repetition frequency on cavitation in shock wave lithotripsy. *The Journal of the Acoustical Society of America*, 112(3), pp1183-1195.

Sapozhnikov, O. A., Maxwell, A. D., MacConaghy, B., and Bailey, M. R. (2007). A mechanistic analysis of stone fracture in lithotripsy. *The Journal of the Acoustical Society of America*, 121(2), pp1190-1202.

Schneider, B., and Shung, K. K. (1996). Quantitative analysis of pulsed ultrasonic beam patterns using a Schlieren system. *IEEE Transactions on Ultrasonics, Ferroelectrics, and Frequency Control*, 43(6), pp1181-1186.

Shimokawa, H., Ito, K., Fukumoto, Y., and Yasuda, S. (2008). Extracorporeal cardiac shock wave therapy for ischemic heart disease. *Shock Waves*, 17(6), pp449-455.

Smith, A. D., Badlani, G. H., Preminger, G. M., Kavoussi, L. R., and Richstone, Lee. (2012a). *Smith's Textbook of Endourology*. Volume III, PMPH-USA.

Smith, N., and Zhong, P. (2012). Stone comminution correlates with the average peak pressure incident on a stone during shock wave lithotripsy. *Journal of Biomechanics*, 45(15), pp2520-2525.

Smith, N., Sankin, G. N., Simmons, W. N., Nanke, R., Fehre, J., and Zhong, P. (2012b). A comparison of light spot hydrophone and fiber optic probe hydrophone for lithotripter field characterization. *Review of Scientific Instruments*, 83(1), 014301.

Staudenraus, J., and Eisenmenger, W. (1993). Fibre-optic probe hydrophone for ultrasonic and shock-wave measurements in water. *Ultrasonics*, 31(4), pp267-273.

Storey, B. D., and Szeri, A. J. (1999). Mixture segregation within sonoluminescence bubbles. *Journal of Fluid Mechanics*, 396, pp203-221.

Strasberg, M. (1959). Onset of ultrasonic cavitation in tap water. *The Journal of the Acoustical Society of America*, 31(2), pp163-176.

Suhr, F., Delhasse, Y., Bungartz, G., Schmidt, A., Pfannkuche, K., and Bloch, W. (2013). Cell biological effects of mechanical stimulations generated by focused extracorporeal shock wave applications on cultured human bone marrow stromal cells. *Stem cell Research*, 11(2), pp951-964.

Sukubo, N. G., Tibalt, E., Respizzi, S., Locati, M., and d'Agostino, M. C. (2015). Effect of shock waves on macrophages: a possible role in tissue regeneration and remodeling. *International Journal of Surgery*, 24, pp124-130.

Sun, J., Gao, F., Wang, Y., Sun, W., Jiang, B., and Li, Z. (2017). Extracorporeal shock wave therapy is effective in treating chronic plantar fasciitis: a meta-analysis of RCTs. *Medicine*, 96(15), E6621.

Tachikawa, R., Tsukamoto, A., Nakagawa, K., Arafune, T., Liao, H., Kobayashi, E., Ushida, T., and Sakuma, I. (2012). Development of an expansion wave generator for shock wave therapy. *Advanced Biomedical Engineering*, 1, pp68-73.

Tailly, G. G. (2013). Extracorporeal shock wave lithotripsy today. *Indian journal of urology: IJU: journal of the Urological Society of India*, 29(3), pp200-207.

Takeuchi, H., Motosuke, M., and Honami, S. (2012). Noncontact bubble manipulation in microchannel by using photothermal Marangoni effect. *Heat Transfer Engineering*, 33(3), pp234-244.

Tanguay, M., and Colonius, T. (2003, November). Progress in modeling and simulation of shock wave lithotripsy (SWL). *In Fifth International Symposium on cavitation (CAV2003)*, Osaka, Japan, November 1-4, OS-2-1-010.

Thoroddsen, S. T., Etoh, T. G., and Takehara, K. (2008). High-speed imaging of drops and bubbles. *Annu. Rev. Fluid Mech.*, 40, pp257-285.

Toepler, A. (1867). Optische studien nach der methode der schlierenbeobachtung. *Annalen der Physik*, 207(6), pp180-215.

Tomita, Y., and Shima, A. (1990). High-speed photographic observations of laser-induced cavitation bubbles in water. *Acta Acustica united with Acustica*, 71(3), pp161-171.

Tomita, Y., Shima, A., and Ohno, T. (1984). Collapse of multiple gas bubbles by a shock wave and induced impulsive pressure. *Journal of Applied Physics*, 56(1), pp125-131.

Tomita, Y., Uchikoshi, R., Inaba, T., and Kodama, T. (2009). Microbubble disruption by ultrasound and induced cavitation phenomena. Proceedings of the 7th International Symposium on Cavitaiton (CAV2009), 109, Ann Arbor, Michigan, USA, August 16-20.

Tu, J., Matula, T. J., Bailey, M. R., and Crum, L. A. (2007). Evaluation of a shock wave induced cavitation activity both in vitro and in vivo. *Physics in Medicine and Biology*, 52(19), pp5933-5944.

Vaezy, S., Shi, X., Martin, R. W., Chi, E., Nelson, P. I., Bailey, M. R., and Crum, L. A. (2001). Real-time visualization of high-intensity focused ultrasound treatment using ultrasound imaging. *Ultrasound in Medicine and Biology*, 27(1), pp33-42.

Wang, C. J., and Chen, H. S. (2002). Shock wave therapy for patients with lateral epicondylitis of the elbow: a one-to two-year follow-up study. *The American Journal of Sports Medicine*, 30(3), pp422-425.

Webster, E. (1963). Cavitation. *Ultrasonics*, 1(1), pp39-48.

Wolf, N. M. (1970). Underwater blast injury-a review of the literature. *Bureau of Medicine and Surgery, Navy Department Research Work Unit*,

Wolfrum, B. (2004). Cavitation and shock wave effects on biological systems [Dissertation]. University of Göttingen, Germany.

Worcester, E. M., and Coe, F. L. (2010). Calcium kidney stones. *New England Journal of Medicine*, 363(10), pp954-963.

Wu, F., Wang, Z. B., Cao, Y. D., Chen, W. Z., Bai, J., Zou, J. Z., & Zhu, H. (2003). A randomised clinical trial of high-intensity focused ultrasound ablation for the treatment of patients with localised breast cancer. *British Journal of Cancer*, 89(12), pp2227-2233.

Wurster, C., Staudenraus, J., and Eisenmenger, W. (1994). The fiber optic probe hydrophone. *In Ultrasonics Symposium, 1994. Proceedings.*, 2, pp. 941-944, IEEE.

Xi, X., and Zhong, P. (2000). Improvement of stone fragmentation during shock-wave lithotripsy using a combined EH/PEAA shock-wave generator—in vitro experiments. *Ultrasound in Medicine and Biology*, 26(3), pp457-467.

Xi, X., and Zhong, P. (2001). Dynamic photoelastic study of the transient stress field in solids during shock wave lithotripsy. *The Journal of the Acoustical Society of America*, 109(3), pp1226-1239.

Xu, Z., and Xu, Y. (2015). The Development And Status Of Extracorporeal Shock Wave Lithotripsy. 5th international Conference on Education, Management, Information and Medicine (EMIM 2015), Shenyangm, China, April 24-26.

Xu, Z., Raghavan, M., Hall, T. L., Mycek, M. A., and Fowlkes, J. B. (2008). Evolution of bubble clouds induced by pulsed cavitational ultrasound therapy-histotripsy. *IEEE Transactions on Ultrasonics, Ferroelectrics, and Frequency Control*, 55(5), pp1122-1132.

Yadav, H. S., Murty, D. S., Verma, S. N., Sinha, K. H. C., Gupta, B. M., and Chand, D. (1973). Measurement of refractive index of water under high dynamic pressures. *Journal of Applied Physics*, 44(5), pp2197-2200.

Yanagida, H., Masubuchi, Y., Minagawa, K., Takimoto, J. I., and Koyama, K. (1999). Effect of ultrasound frequency on sonochemical luminescence under well-determined sound pressure. *Japanese journal of applied physics*, 38(5S), pp3103-3104.

Zel'dovich, Y. B., and Raizer, Y. P. (1965). *Physics of shock waves and high-temperature hydrodynamic phenomena* (No. FTD-MT-64-514). FOREIGN TECHNOLOGY DIV WRIGHT-PATTERSON AFB OH.

Zhong, P., Xi, X., Zhu, S., Cocks, F. H., and Preminger, G. M. (1999). Recent developments in SWL physics research. *Journal of Endourology*, 13(9), 611-617.

Zhong, P., Zhou, Y., and Zhu, S. (2001). Dynamics of bubble oscillation in constrained media and mechanisms of vessel rupture in SWL. *Ultrasound in Medicine and Biology*, 27(1), pp119-134.

Zhou, Y., and Zhong, P. (2003). Suppression of large intraluminal bubble expansion in shock wave lithotripsy without compromising stone comminution: Refinement of reflector geometry. *The Journal of the Acoustical Society of America*, 113(1), pp586-597.

Zhou, Y., Qin, J., and Zhong, P. (2005). The Characteristics of Cavitation Bubbles Induced by the Secondary Shock Wave in an HM-3 Lithotripter and Its Effect on Stone Comminution. In *AIP Conference Proceedings*, The 5th International Symposium of Therapeutic Ultrasound (ISTU5), abstract book, 829(1), pp298-302. AIP.

Zhou, Y., Qin, J., and Zhong, P. (2012). Characteristics of the secondary bubble cluster produced by an electrohydraulic shock wave lithotripter. *Ultrasound in Medicine and Biology*, 38(4), pp601-610.

Zijlstra, A., and Ohl, C. D. (2008). On fiber optic probe hydrophone measurements in a cavitating liquid. *The Journal of the Acoustical Society of America*, 123(1), pp29-32.